SYNTHESIS OF CARBON SUPPORTED ORDERED INTERMETALLIC NANOPARTICLES AS OXYGEN REDUCTION CATALYSTS IN POLYMER ELECTROLYTE MEMBRANE FUEL CELLS

A Dissertation

Presented to the Faculty of the Graduate School

of Cornell University

In Partial Fulfillment of the Requirements for the Degree of

Doctor of Philosophy|

by

Minh Thai Nguyen

January 2014

SYNTHESIS OF CARBON SUPPORTED ORDERED INTERMETALLIC NANOPARTICLES AS OXYGEN REDUCTION CATALYSTS IN POLYMER ELECTROLYTE MEMBRANE FUEL CELLS

Minh Nguyen, Ph. D.

Cornell University 2014

Polymer Electrolyte Membrane Fuel cells are electrochemical devices that convert energy stored in chemical bonds of fuel (hydrogen gas, methanol, etc.) directly into electrical energy with high theoretical efficiency. The major challenges are the slow oxygen reduction reaction kinetics, requiring a significant amount of Pt catalyst to achieve significant current densities. Finding catalysts, which are more active and cheaper than Pt, as well as being stable under cathodic conditions will be key to making this technology more economically attractive. First, a method was developed to synthesize ordered intermetallic nanoparticles in the 4-6 nm size range. The synthetic method used was a modified solution phase coreduction method, which is able to synthesize ordered intermetallic nanoparticles in the 4-6 nm size range. This method was used to form carbon supported, ordered tetragonal Pt_2MM' (M and M' are = Fe, Co, or Ni) nanoparticles. After extensive characterization and electrochemical measurements, it was found that ordered tetragonal Pt_2FeNi/C catalyst showed the highest activity roughly four times as efficient as pure platinum, with a half-wave potential roughly 30 mV more positive than the Pt/C standard. The ordered tetragonal material also showed high stability under cathodic conditions, losing roughly 10% of the 3d element after 2000 cycles (from 0.05 – 1.10 V at 50 mV/s).

BIOGRAPHICAL SKETCH

Minh Nguyen was born Spetember 23rd, 1986 in San Jose California. He eventually made his way to sunny southern California where he graduated from Lake Elsinore High School. Afterwards, he attended college at the University of La Verne, CA, where he excelled in the sciences, giving him the opportunity to become an Undergraduate Teaching Assistant for General and Organic chemistry. In the summer of 2007, he did a REU internship at Harvey Mudd College with Professor Adam Johnson, focusing on developing new catalysts to improve the enantioselectivity in the hydroamination reaction of alkenes. After graduating from La Verne in 2008, he decided to continue his education at Cornell University where he worked on the research and development of new active and stable oxygen reduction catalysts for fuel cells with Professor Frank DiSalvo.

To my parents Lisa Mai Nguyen and Hung Thai Nguyen,

and my sister Thai Hang Nguyen

ACKNOWLEDGMENTS

I am thankful for all the inspiration, guidance, encouragements, and understanding of my professors, mentors, colleagues, family, and friends.

I would like to thank Professor Frank DiSalvo for giving me the opportunity to work in his lab as well as the guidance and encouragement during my graduate studies. Thanks for letting me explore my interests in nanoparticle synthesis and catalysts. I would like to thank Professors Héctor D. Abruña and Bruce van Dover for serving on my thesis committee and their valuable suggestions.

I thank Jake Smarr, Joanna Tan, Laurie Lange, and Josh Judkins for their friendship. I could not have survived Ithaca mentally without you guys. I would also like to thank those that helped me with my research: Brian Leonard, Minghui Yang, Ryo Wakabayashi, Hao Chen, Chinmayee Subban, and Spencer Robins. I also thank the current DiSalvo group members for your advice and attention during group meeting presentations.

TABLE OF CONTENTS

LIST OF FIGURES

LIST OF TABLES

CHAPTER 1

INTRODUCTION TO PROTON ELECTROLYTE MEMBRANE FUEL CELLS

1.1 Introduction to Proton Electrolyte Membrane Fuel Cells

The motivation for alternative energy systems, centered on renewable energy, is stimulated by the increased global demand for energy, finite abundance of fossil fuel resources, and fears of climate change fueled by excessive carbon dioxide emissions. In the last decade, major efforts have been put into the development of "the hydrogen economy." The use of hydrogen as an energy carrier has the potential to reduce green house gas emissions, improve air quality, and improve energy efficiency and security by addressing the problems of intermittence in wind, solar, and other forms of clean and renewable energy generation. Hydrogen has many uses; the largest application of hydrogen is for the processing or "upgrading" of fossil fuels and production of ammonia. Hydrogen can be prepared in several different ways, the most economical way of commercial bulk hydrogen production is through steam reforming of natural gas.[1] Ideally, industrial scale hydrogen would be produced from water via electrolysis from electricity generated by renewable energy sources such as wind, solar, geothermal, etc. Direct water splitting by photocatalysis has the potential to offer a direct and efficient route to obtaining clean hydrogen from water, though advances in the field are needed to make this process economically feasible.

Fuel cells are electrochemical devices that convert energy stored in chemical bonds of fuel (hydrogen gas, methanol, formic acid, etc.) directly into electrical energy with high theoretical efficiency, without being limited by the Carnot efficiency,

inherent in any heat engine. The allure of fuel cells is little to no carbon emission; using hydrogen gas as a fuel, the only byproduct would be water, heat, and electricity. Of course, if the hydrogen is produced from a fossil fuel source, source CO_2 is produced in that step.

A typical fuel cell using hydrogen as a fuel consists of an anode, where hydrogen is oxidized, and a cathode, where oxygen is reduced. The two compartments are separated by an ionically conducting polymer electrolyte, which facilitates the transfer of ions generated during the oxidation and reduction processes. The electrolyte also serves as a physical barrier, ideally preventing the mixing of the fuel and oxidant. The operating temperature of the fuel cell is dependant on the choice of electrolyte material and the fuel. Table 1.1 lists the common types of fuel cells, the temperature at which they operate at, the electrode and electrolyte materials, and the electrode reactions. Depending on the type, size, efficiency, and operating temperature, fuel cells can be used in stationary or mobile and portable applications.

Table 1.1 *Types of fuel cells*

Fuel Cell Type	Electrolyte Used	Catalyst	Operating Temp., °C	Electrode Reaction
Polymer Electrolyte	Polymer Membrane	Pt for anode & cathode	50-120	Anode: $H_2 = 2H^+ + 2e^-$ Cathode: $½O_2 + 2H^+ + 2e^- = H_2O$
Direct Methanol	Polymer Membrane	Pt-Ru for anode, Pt on cathode	90-120	Anode: $CH_3OH + H_2O = 6H^+ + CO_2 + 6e^-$ Cathode: $1½O_2 + 6H^+ + 6e^- = 3H_2O$
Direct Formic Acid	Polymer Membrane	Pd anode Pt cathode	< 40	Anode: $HCOOH = CO_2 + 2H^+ + 2e^-$ Cathode: $½O_2 + 2H^+ + 2e^- = H_2O$
Alkaline	Potassium Hydroxide	non-precious metals	< 80	Anode: $H_2 + 2OH^- = H_2O + 2e^-$ Cathode: $½O_2 + H_2O + 2e^- = 2OH^-$
Phosphoric Acid	Phosphoric Acid	Pt for anode & cathode	150-200	Anode: $H_2 = 2H^+ + 2e^-$ Cathode: $½O_2 + 2H^+ + 2e^- = H_2O$
Molten Carbonate	Lithium/ Potassium Carbonate	non-precious metals	600-650	Anode: $H_2 + CO_3^{-2} = H_2O + CO_2 + 2e^-$ Cathode: $½O_2 + CO_2 + 2e^- = CO_3^{-2}$
Solid Oxide	Yittria Stabilized Zirconia	Ni for anode, perovskite oxide cathode	850-1100	Anode: $H_2 + O^{-2} = H_2O + 2e^-$ Cathode: $½O_2 + 2e^- = O^{-2}$

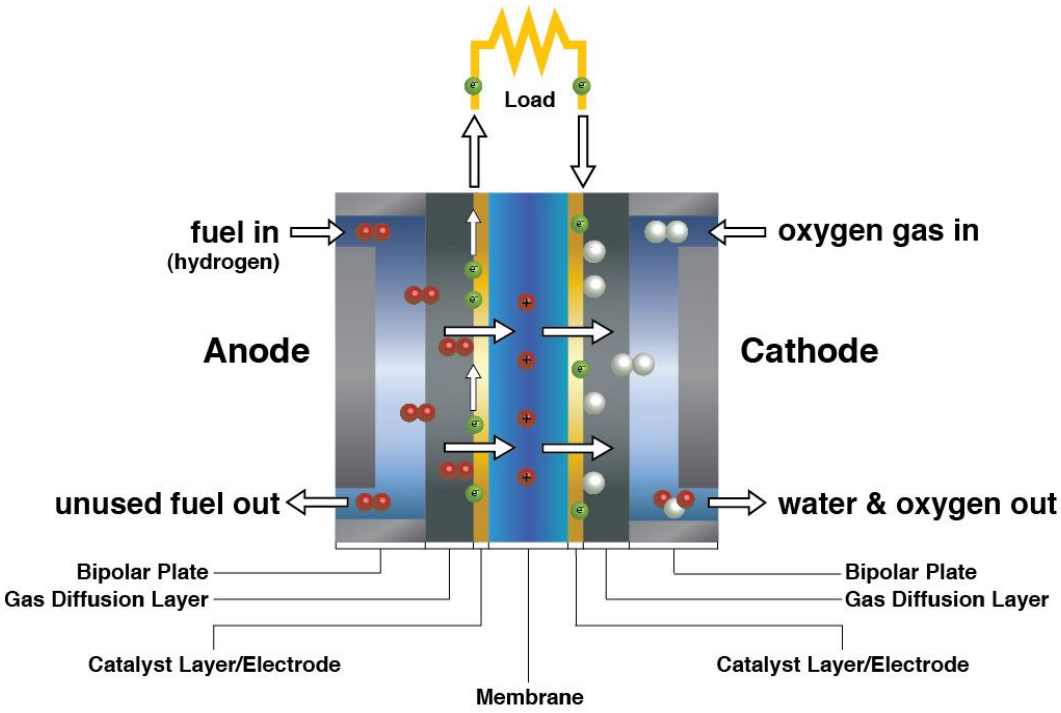

Figure 1.1. Schematic of PEM fuel cell

Of the different classes of fuel cells, Polymer Electrolyte Membrane Fuel Cells (PEMFCs) are considered the most economically viable candidate for automotive applications due to their low operating temperatures, short warm-up time, and high power density. A schematic of a typical PEMFC is shown in Fig. 1.1. The core of the fuel cell is the membrane electrode assembly (MEA) and consists of the membrane electrode sandwiched between the catalyst electrode layers. The gas diffusion layer (GDL) serves as a bridge between the MEA and bipolar plates and serves the following functions: allows gas or fuel to flow from the channels to the catalyst layer, removes byproduct water outside of the catalyst layer and prevents flooding by excessive liquid water accumulation while keeping some water on the surface for conductivity through the membrane, transfers heat during cell operation, and provides mechanical strength to hold MEA from expansion caused by water absorption. The bipolar plates are generally made of mechanically rigid, electrically conductive and corrosion resistant materials such as graphite, carbon, or stainless steel. Along with providing an electrically conductive path for electron flow when several MEAs are stacked in series, the bipolar plates may contain coolant flow fields to remove waste heat generated by the fuel cell reaction.[2]

The commonly used proton exchange membrane, Nafion®, consists of a perfluorosulfonic acid (PFSA) ionomer, which needs to be hydrated in order to optimize proton conduction. The need to keep the membrane hydrated limits the operating temperatures of the PEMFC to below 100^{o}C, through it has been shown that the incorporation of silica and zirconium phosphate into Nafion water channels can increase the working temperature to above 100^{o}C.[3]

Platinum facilitates the hydrogen oxidation reaction (HOR) at the anode according to equation 1.1. The protons produced in this reaction migrate through the membrane towards the cathode while the electrons produced flow through the external circuit creating an electric current. Platinum also facilitates the oxygen reduction reaction (ORR) at the cathode according to equation 1.2. The migrated protons combine with reduced oxygen and the electrons to form water. The overall electrochemical reaction of the PEMFC is given by equation 1.3.

HOR: $\mathbf{H_2 \rightarrow 2H^+ + 2e^-}$ $\mathbf{E^0 = 0.00\ V\ vs.\ SHE}$ **(Eq. 1.1)**

ORR: $\mathbf{1/2O_2 + 2H^+ + 2e^- \rightarrow H_2O}$ $\mathbf{E^0 = 1.23\ V\ vs.\ SHE}$ **(Eq. 1.2)**

Overall rxn: $\mathbf{H_{2(g)} + 1/2O_{2(g)} \rightarrow H_2O_{(l)}}$ $\mathbf{E^0 = 1.23\ V\ vs.\ SHE}$ **(Eq. 1.3)**

The HOR is relatively facile on Pt surfaces, with exchange current densities of about 10^{-3} A·cm^{-2}).[4] Due to the low operating temperatures of PEMFCs and the method through which commercial hydrogen is synthesized (steam reforming of methane produces CO as a byproduct), catalyst stability and tolerance to poisoning is an issue. In relation to catalysis, a poison, such as CO, is defined as an impurity that lowers the activity an efficiency of the material. In this case, PtRu has shown to be more CO tolerant, an alternative approach would be to remove CO catalytically from the hydrogen stream. For the cathode, the standard electrocatalysts are Pt nanoparticles (ideally in the 3-5 nm size range) that are highly dispersed on a conducting carbon support (roughly 30-40 nm particles) to achieve a high Pt surface area (around 100 m^2/g). Pt is the most active element for ORR, yet the rate of ORR at the cathode, being

the most critical, has exchange current densities of about 10^{-8} A·cm^{-2}, roughly 5 magnitudes slower than HOR [4]. Due to the sluggish reduction kinetics at the cathode, high Pt loadings are necessary to partially compensate for the faster rates of HOR (0.4 mg_{Pt}/cm^2 at the cathode compared to 0.05 mg_{Pt}/cm^2 at the anode).[4,10]

1.2 Challenges for Oxygen Reduction Reaction

In order for commercial implementation of PEMFCs for mobile and transportation applications, the technology needs to be more economically sound. There are several factors that influence the cost: one, the initial cost of the fuel cell; two, durability; three, fuel distribution station issues; and four, efficiency of the fuel cell. The major contributor to the high cost is the sluggish kinetics of ORR, which requires high Pt loadings. Even with high Pt loading, the activation overpotential for ORR is about 0.4 V at low current densities (less than 100 mA/cm^2). The DOE targets for automotive applications is 0.2 g_{Pt}/kW, implying that the required amount of Pt in the cathode compartment needs to be reduced to less than 0.1 mg_{Pt}/cm^2.[5] To achieve this benchmark, more active and stable catalysts with lower Pt content will need to be developed.

Much research has been devoted to increasing the activity and decreasing the Pt loading by alloying various 3d transition metals.[4,6-9] However, these alloyed electrocatalysts suffer from stability issues under PEMFC cathodic operating conditions. The high working potentials and acidic environment will leach non-Pt metals exposed on the surface of the nanoparticle into the electrolyte. An alternative approach has been to structure Pt catalysts to achieve high mass based activities.

These include, for example, core-shell catalysts or controlled crystal face orientation of catalysts.[4,10,11]

1.3 Introduction to Nanomaterials

Nanomaterials are materials with morphological features on the nanoscale, usually defined as smaller than a tenth of a micrometer in at least one dimension.[12] Inorganic nanoparticles, or nanocrystals, are of particular interest due to their diverse range of physical and chemical properties with numerous applications in fields such as catalysis, energy storage, electronics, data storage, and many others. An important aspect of going into the nanoscale is the vastly increased ratio of surface area to volume, which leads to new quantum mechanical effects. One example is the "quantum size effect,"[13] where the physical and electronic properties of bulk materials change with reductions in particle size, with the greatest change observed in particles sizes below 20 nm. Aside from particle size,[13] the composition,[6-9] morphology,[14-16] and crystal structure[17] have been shown to alter the material's properties. Thus the controlled synthesis of these materials is crucial to their performance and integration into various technologies.

Controlling these parameters synthetically is quite challenging, even for single metal systems, and typically the procedures of synthesizing such nanocrystals are quite specific to the targeted material, lacking adaptability when applied to different systems. For example, the synthesis of Pd nanocubes can be accomplished by reducing Na_2PdCl_4 with ethylene glycol (EG) in the presence of poly(vinyl pyrrolidone (PVP) and KBr in an appropriate ratio, with the nanocube formation occurring only under

specific injection rates, concentrations, and temperatures.[18] The preparation of similar noble metal nanocubes (Au and Pt) have drastically different preparation methods, with Au nanocubes using ascorbic acid (AA) as a reducing agent in the presence of cetyltrimethylammonium chloride (CTAC)[19] or alternatively Pt nanocube formation occurring using a solution of oleic acid and oleyamine with trace amounts of $Fe(CO)_5$.[20] This chemistry is typically unsuccessful when applied to other metals, often not forming particles at all or resulting in spherical or randomly shaped particles. This is a common story when discussing inorganic nanocrystal synthetic techniques; most are not generally applicable to other phases or types of materials, so the conditions for each system need to be studied and established on a case-by-case basis. If there were a more general synthetic method to create nanoparticles with control over size, composition, and crystal structure, it would be possible to streamline the development and integration of advanced materials for future applications.

The synthesis of microscale and nanoscale materials has been studied for decades, but only recently have chemists begun to control key aspects of the particles such as size, shape, composition, and structure. Several approaches have been developed for the synthesis of inorganic nanomaterials and they are generally divided into two categories: top-down and bottom-up. The top-down approach generally consists of fracturing bulk pieces of the desired material and mechanically breaking them down to micron and nano-sized particles using techniques such as high-energy wet ball milling.[21] While these techniques are great for large industrial scale operations, this technique is quite limited in controlling the morphology and size of the material, as the smallest particles achieved are roughly 70-90 nm in diameter.[21]

Bottom-up approaches, however, are readily adapted to controlling the size and morphology of the resulting materials and examples of these techniques include, but are not limited to, precipitation processes,[22] the sol-gel method,[23] and aerosol methods.[24] While several synthetic techniques have been developed for the synthesis of metals[18-20,24] and simple binary phases,[4,19,22,25] very few techniques allow for solution-based synthesis of diverse intermetallic nanomaterials below 10 nm in dimension.

Intermetallics are an important class of materials with many useful properties and as such, have been incorporated into numerous applications.[4,25] For example, intermetallics can display desirable magnetic, superconducting, and chemical properties due to their strong internal order and mixed (metallic and covalent/ionic) bonding, making them ideal for applications in high capacity data storage,[21] gate contact/barrier layers for microelectronics,[17] and catalysts.[4,9,25]

Materials scientists use the term intermetallic in a number of different ways; most commonly, *intermetallic* refers to solid-state phases involving two or more metals. Many intermetallic compounds are often called "alloys," but we need to be more precise in defining what kinds of structures are implied by these descriptors. In alloys the various elements substitute randomly for one another on the same crystallographic sites (Wyckoff positions) in the unit cell, forming a "solid solution" with a range of possible compositions.[32] In ordered intermetallic compounds, different elements occupy different crystallographic sites in the structure, with distinct local environments and often a well-defined, fixed stoichiometry. Often the descriptor "ordered" is left out when talking about intermetallic compounds, and we do so here,

but always imply that order exists. The atomic ordering of intermetallics compounds will often give rise to different crystal structures than the elements that comprise them and can also change the properties of the material. For example, atomically disordered CoPt alloy particles are superpapamagnetic, but upon ordering the Co and Pt atoms in alternating layers in a tetragonal crystal structure, CoPt exhibits room temperature ferromagnetism with high coercivity.[27] With regards to PEMFC catalysis, intermetallic bulk materials have shown enhanced ORR activity.[4,28] However, advances in synthesizing intermetallic nanoparticles in the sub 10 nm range need to be developed.

Intermetallics are traditionally synthesized using high temperature reactions and lengthy annealing times. Some common synthetic techniques include arc melting and powder metallurgy, where the reactants are heated to high temperatures (typically above 1000^{o}C) followed by days or weeks of annealing. Formation of intermetallic phases requires homogenous mixing of reactants as small particles (typically 1-100 μm) and high temperatures to overcome the slow solid-solid diffusion rates in the solid state. The lengthy annealing times are necessary for reactants to become homogeneous, nucleating and growing long range ordered intermetallic structure throughout the material. The high temperature reactions that are required for traditional solid-state synthesis, while important for generating many useful materials, offer little control of morphology or particle size, especially in the nanometer regime. In some cases, the desired phase can be directly crystallized from a melt of the same composition (congruent melting), but this method is more appropriate for growing bulk crystals or polycrystals with large grain sizes.

Some alternative techniques have been developed to synthesize bulk scale

solid-state materials at low temperatures and with reduced annealing times. Most of these methods try to overcome the diffusion problems that are inherent in solid-state reactions by intimately mixing the starting materials. Examples of these techniques include co-precipitation of metal precursors,[4,9,22,30] sol-gel processing,[25] vacuum deposition,[30] and annealing elementally modulated thin films.[29] These techniques are quite practical and have been able to reduce both heating temperatures and annealing times since the reaction products are homogeneously mixed on the atomic level.

Several solution-based approaches have been developed to synthesize metal nanoparticles.[4,9,22] These reactions typically use metal salts[9] or organometallic precursors[22] as reagents and thermally decompose or reduce them to form free zero-valent metal atoms in solution. The metal atoms then aggregate into small alloy particles whose growth, and therefore particle size and morphology, can be influenced by the presence of surface stabilizing agents. Altering the reagent concentrations can control the composition of the nanoparticles.

For applications in PEM catalysis, oxygen reduction and oxidation of fuel occur on the surface of the nanomaterials, therefore, it is crucial to have clean and electrochemically active surfaces. Heating above room temperature is often necessary to nucleate the ordered phase from the disordered or alloy products, thus, the use of surface stabilizing agents should be avoided as decomposition of the organics may deposit a carbon layer that covers the catalyst surface, rendering it inactive. On the other hand, exposing unprotected nanoparticles to high temperatures can cause the particles to agglomerate, sinter, and grow, leading to a rapid decrease in the active surface area of the catalyst.

Some methods have been developed to form intermetallic nanocrystals in the 5-10 nm size range.[13,17,30,31] For example, Aslam *et al.* have shown that ordered face-centered-cubic (fct) PtFe nanocrystals in the 4-6 nm size range can be synthesized by encapsulating alloy PtFe nanoparticles in a SiO_2 shell, which prevents the particles from agglomerating during the annealing phase, up to 1000^{o}C. However, the ordered particles are often kept inside the silica shells, and removal of the silica shells cause the particles to agglomerate. If surface stabilizing surfactants are used during the synthesis, there is a thin carbon layer that is not easily removed.[30] Sun *et al.* have also shown size controlled PtFe nanoparticles using a similar method, employing MgO to encapsulate the particles and prevent rapid particle growth. The MgO is removed with a dilute HCl wash, with only minor Fe metal leaching. However, significant particle agglomeration was observed. The use of surface stabilizing surfactants such as hexadecanethiol and oleic acid are able to stabilize the particles for several hours; however, complete removal of the carbon groups was unable to be achieved.[31,32] In order to explore the properties of intermetallic nanomaterials as PEMFC catalysis, it is imperative to develop a broad method of synthesizing well-dispersed, intermetallic nanocrystals with tunable size and composition without the use of strongly coordinating surfactants.

1.4 Scope of Dissertation

The second chapter of this dissertation will focus on the synthesis of size-controlled alloy and ordered bimetallic nanoparticles using a one-pot solution co-reduction technique. The method of nanoparticle synthesis is dependant on

tetrahydrofuran (THF) soluble metal chloride and/or lithium metal chloride precursors followed by rapid reduction. The choice of reducing agent is dependent on the reduction potential of the precursors and has shown to have an affect on controlling particle size. Emphasis will be given to the generality of the synthetic method and will touch briefly on the method used to transfer particles to a conducting carbon support. Characterization of the various nanomaterials using XRD, EDX, SEM, TEM, as well as XPS will be presented and discussed.

The third chapter of this dissertation will explore the electrochemical activity and stability of pseudo-ternary Pt based nanomaterials using the method presented in chapter 2. The activity and stability of these catalysts towards ORR was determined from techniques such as cyclic voltammetry (CV) and rotating disk electrode (RDE) analysis, which are discussed in greater detail.

The fourth chapter will focus on applying this synthetic method to making true ternary nanomaterials, where each of the three elements are ordered on different crystallographic sites to form a structure not observed in any binary compound. This method was unable to form pure, single-phase true ternary materials, however several hypotheses as to why are discussed.

REFERENCES

1 Oxtoby, D. W.; Gillis, P. H.; Nachtrieb, N. H. *Principles of Modern Chemistry*; 5th ed.; Brooks/Cole Publishing Co., 2002.

2 Salwan, D. S.; Zaharim, A.; Sopian, K. In *International Conference on Energy & environment* 2009, p 371.

3 A. K. Sahu, S. Pitchumani, P. Sridhar and A. K. Shukla, *Indian Academy of Sciences* **2009**, *32*, 285-294.

4 *PEM Fuel Cell Electrocatalysts and Catalyst Layer: Fundamentals and Applications*; illustrated ed.; Springer, 2008.

5 N. N. Laboratory in *Pathways to Commercial Success: Technologies and Product Supported by the Fuel Cell Technologies Program, Vol.* U.S. Department of Energy, **2012**.

6 S. J. Hwang, S. J. Yoo, S. Jang, T.-H. Lim, S. A. Hong and S.-K. Kim, *The Journal of Physical Chemistry C* **2011**, *115*, 2483-2488.

7 J. Luo, L. Wang, D. Mott, P. N. Njoki, N. Kariuki, C.-J. Zhong and T. He, *Journal of Materials Chemistry* **2006**, *16*, 1665.

8 S. Thungprasert, T. Sarakonsri, W. Klysubun and T. Vilaithong, *Journal of Alloys and Compounds* **2011**, *509*, 6812-6815.

9 S. Koh, M. F. Toney and P. Strasser, *Electrochimica Acta* **2007**, *52*, 2765-2774.

10 S. Zhang, M. Qing, H. Zhang and Y. Tian, *Electrochemistry Communications* **2009**, *11*, 2249-2252.

11 D. Zhao, Y.-H. Wang and B.-Q. Xu, *The Journal of Physical Chemistry C* **2009**, *113*, 20903-20911.

12 Buzea, C.; Pacheco, I.; Robbie, K. *Biointerphases* **2007**, *2*.

13 E. V. Shevchenko, D. V. Talapin, H. Schnablegger, A. Kornowski, O. Festin, P. Svedlindh, M. Hasse and H. Weller, *Journal of American Chemical Society* **2003**, 9090-9101.

14 C. Burda, X. Chen, R. Narayanan and M. El-Sayed, *Chemical Review* **2005**, *105*, 1025-1102.

15 S. Eustis and M. El-Sayed, *Chemical Society Reviews* **2006**, *35*, 209-217.

16 C. J. Orendorff, T. K. Sau and C. J. Murphy, *Small* **2006**, *2*, 636-639.

17 S. Sun, S. Anders, T. Thomson, J. E. Baglin, M. F. Toney, H. F. Hamann, C. B. Murray and B. D. Terris, *Journal of Physical Chemistry C* **2003**, *107*, 5419-5425.

18 M. Jin, H. Zhang, Z. Xie and Y. Xia, *Angewandte Chemie* **2001**, *50*, 7850-7854.

19 C.-L. Lu, K. S. Prasad, H.-L. Wu, K.-a. A. Ho and M. Huang, *Journal of American Chemical Society* **2010**, *132*, 14546-14553.

20 C. Wang, H. Daimon, Y. Lee, J. Kim and S. Sun, *Journal of American Chemical Society* **2007**, *129*, 6974-6975.

21 C. Raab, M. Simko, U. Fiedeler, M. Nentwich and A. Gazso, *Nano Trust Dossiers* **2011**, *6*, 1-4.

22 E. V. Shevchenko, D. V. Talapin, H. Schnablegger, A. Kornowski, O. Festin, P. Svedlindh, M. Hasse and H. Weller, *Journal of American Chemical Society* **2003**, 9090-9101.

23 L. Hench and J. West, *Chemical Review* **1990**, *90*, 33-72.

24 Y. He, X. Li and M. Swihart, *Chemistry Materials* **2004**, *17*, 1017-1026.

25 D. Wang, Q. Peng and Y. Li, *Nano Research* **2010**, *3*, 574-580.

26 Sun, S.; Murray, C. B.; Weller, D.; Folks, L.; Moser, A. *Science* **2000**, *287*, 1989-1992.

27 L. Castaldi, K. Giannakopoulos, A. Travlos, D. Niarchos, S. Boukari and E. Beaurepaire, *Journal of Physics: Conference Series* **2005**, *10*, 155-158.

28 Yu, D. Wang, H. Xin, H. Abruna and D. Muller, *Microscopy and Microanalysis* **2012**, *18*, 1306-1307.

29 M. Baldauf and D. M. Kolb, *The Journal of Physical Chemistry C* **1996**, *100*, 11375-11381.

30 J. Z. Chen, H. Herman and S. Safai, *Journal of Thermal Spray Technology* **1993**, *2*, 357-361.

31 J. Kim, Y. Lee and S. Sun, *Journal of American Chemical Society* **2010**, *132*, 4996-4997.

32 L. Kantorovich, *Quantum Theory of the Solid State: An Introduction*, Springer **2004**, p. 28.

CHAPTER 2

SYNTHESIS OF SIZE CONTROLLED, ORDERED INTERMETALLIC NANOPARTICLES USING A MODIFIED SOLUTION PHASE CO-REDUCTION METHOD

2.1 Introduction

Multimetallic materials, both alloys (a homogeneous mixture or solid solution of two or more metals) and intermetallics (multimetallic materials where different elements have distinct local environments) are among the most important solid-state materials in modern science and technology.[1-3] Solid-state materials posses a diverse range of physical and chemical properties such as energy storage,[4] super hard materials,[5] ferromagnetism,[6-8] superconductivity,[9-11] corrosion resistance,[12] catalysis,[13-18] and many more. The physical and chemical properties of these solid-state materials are highly dependent on composition and often processing conditions, so controlling these variables is crucial to their performance in advanced applications. From the 91 metal elements in the periodic table (under standard conditions), there are 4095 different binary metal systems, and within each binary system, there may exist several intermetallic phases and many more possible alloy compositions. The possible intermetallic and alloy phases increase exponentially when ternary and quaternary multimetallic systems are considered; finding the right material composition with the exact properties for a particular application could take several decades, especially if processed and tested one at a time.

To accelerate the discovery of advanced PEMFC catalytic materials, much

attention has been focused on high-throughput screening methods such as combinatorial sputtering[19,20] and theoretical computational modeling,[21] which can potentially screen entire multimetallic systems for the most catalytically active compositions in the fraction of the time. However, the bulk chemical and physical properties of a given material also depend on how the material is synthesized as well as the surface vs. bulk structure and composition of the material (such as surface segregation). In combinatorial sputtering for example, the different compositions are synthesized and tested in the form of a thin film, often exhibiting different activities when the active composition is synthesized and tested as carbon supported nanoparticles.[19,22] Similar arguments can be made with high-throughput computational modeling methods,[21,23] reasons for which have been satirized in a popular joke about theoretical physicists:

> Milk production at a dairy farm was low, so the farmer wrote to the local university, asking for help from academia. A multidisciplinary team of professors was assembled, headed by a theoretical physicist, and two weeks of intensive on-site investigation took place. The scholars then returned to the university, notebooks crammed with data, where the task of writing the report was left to the team leader. Shortly thereafter the physicist returned to the farm saying to the farmer, "I have the solution, but it only works in the case of spherical cows in a vacuum." [24]

The point of the joke is that theoretical modeling will often reduce a problem to its simplest form to make the calculations more feasible (often due to technological limitations), even though such simplifications may miss the essential phenomena that result in the observed behavior. Though not completely perfect, both high-throughput methods do provide helpful clues as to which multimetallic systems should be given greater attention by synthetic material scientists. When the observed properties of such

high-throughput methods are used to design the next set of combinatorial or theoretical "experiments," a positive feedback loop can be generated to improve both the materials property and the existing models and techniques. As mentioned in the previous chapter, the synthesis of nanomaterials is often complicated and generally limited to a handful of metallic systems. To quicken the discovery and eventual integration of advanced multimetallic nanomaterials into real world applications, it would be highly beneficial to develop a relatively simple method of synthesizing size controlled alloy and intermetallic nanoparticles, which can be applied to a wide range of multimetallic systems.

For applications in solid-state (heterogeneous) catalysis, the efficiency and economic affordability of a given material depends on particle size, or more precisely the surface area. High surface area materials have a lower fraction of atoms at the surface (rather than being inaccessible in the interior of the particle). Nanoparticles have a very high specific surface area, for example, Pt nanoparticles with a diameter of 2 nm will have a surface area of roughly 140 m^2/g[25] and roughly 58% of the Pt atoms are in the surface layer.

2.1.1 Catalysis: Nanoparticles with Clean Surfaces

When dealing with applications in catalysis, it will be useful to specify the term "clean surface." Atomically clean metal surfaces are usually highly reactive and thus only really exist in extreme conditions (under ultra high vacuum and/or high temperatures), but definitely not in a chemical flask. The high reactivity comes from the under coordinated surface atoms, which, upon contact with other matter (gasses,

liquids, and even solids reacts via physisorption, chemisorption, or solid state diffusion), resulting in a decrease in the total energy of the surface or interface.[26] A particle surface is considered "clean" when no molecules are strongly adsorbed on it, though it may be covered with weakly interacting molecules. Generally speaking, adsorption is strong (chemisorption) when the adsorption energy, ΔG_{ads}, is greater than 30-40 kJ/mol,[26] which implies that the probability of desorption from the surface at room temperature is very small. The adsorption of a molecule on is temperature dependent according to equation 2.1.

$$\tau_a \approx \tau_0 e^{\Delta G_{ads}/RT} \qquad \textbf{(Eq. 2.1)}$$

τ_a = residence time (time passed between adsorption and desorption)
τ_0 = characteristic time of surface atom vibration (~ 10^{-12} s^-)[27]
ΔG_{ads} = adsorption energy
R = gas constant (8.314 J K^- mol^-)
T = temperature (K)

Increasing the temperature of the system under vacuum may be a viable option to removing adsorbed species from metallic surfaces when ΔG_{ads} is small enough and when possible decomposition or side reactions do not occur.

2.1.2 Methods to Prevent Nanoparticle Agglomeration

Nanoparticles are thermodynamically unstable, due to the characteristic high ratio of under coordinated surface atoms to fully coordinated bulk atoms, and have a tendency to lower their high surface energies. To stabilize themselves, bare nanoparticles will either adsorb surrounding molecules or lower their surface area through agglomeration. In order to avoid particle agglomeration (important for

applications in catalysis), nanoparticles need to be kinetically stabilized either by adsorption of neutral or charged molecular species or by strong particle support interactions at the surface of a solid support material.[27] The kinetic stabilization of nanoparticles through molecular steric and electrostatic repulsive forces has been thoroughly discussed in the literature.[28-32] For the scope of this thesis, they will be briefly summarized below.

Nanoparticle stabilization, via steric repulsive forces, is done by adsorbing certain molecules (surfactants) onto the particle's surface to sterically separate them from one another, preventing particle-particle collision and fusion. The size, chemical nature, and concentration of these adsorbed molecules determine the degree of stabilization. When one dimension of the surfactant molecule is significantly longer than the typical size of the nanoparticle, a "corona" of surfactant forms around the particle. Thus, large molecular weight (generally containing long alkyl chains) molecules are typically used as surfactants to prevent nanoparticle agglomeration.[28,29,31] Another important requirement for an effective stabilizer is large adsorption energy; large adsorption energy ensures the surfactant will not (or has a low probability to) spontaneously desorb from the particles surface, thus ensuring particles will not cluster. Molecules that can readily donate electron density, such as molecules with π-electrons (aromatic systems) or other lone pairs with valence electrons (amines, water, alcohols, organic acids, etc.), often adsorb very strongly to metal surfaces that are electron-deficient (surfaces with more valence orbitals than valence electrons).[29] This method of nanoparticle stabilization is an effective route to controlling particle size, uniformity, and dispersibility;[31] however, for applications in

catalysis where clean surfaces are required, steric stabilization methods (as described above) need to be employed with care. If the surfactant cannot be completely removed, the surface is partly or fully blocked and the effectiveness of the catalyst is reduced, perhaps even to zero. In those cases, the catalyst is "poisoned" and inactive.

Electrostatic stabilization occurs via repulsive electrostatic forces, which nanoparticles experience when the particles are charged.[30,32] The approach and adsorption of a negatively charged anion to a metal particle induces a partial charge (δ^+) on the surface as depicted in Figure 2.1. The Coulomb interaction between equally "charged" particles is repulsive, which is the basis of general electrostatic stabilization.[30,32] When nanoparticles are in solution containing both anions and cations, the metal surface (depending on how electropositive the metal is) is surrounded primarily by one kind of ion (most likely the anion) followed by a shell of the counter ions.[33] The concentration of anions and cations near the particle surface is strongly perturbed from that at large distance from the particle; the length scale over which the concentration is significantly perturbed is called the Debye length as illustrated in Fig. 2.2. Debye length (κ^{-1}) depends on the concentration of the ionic solute (C_o) and the dielectric constant of the solvent (ε_r) by equation 2.2.

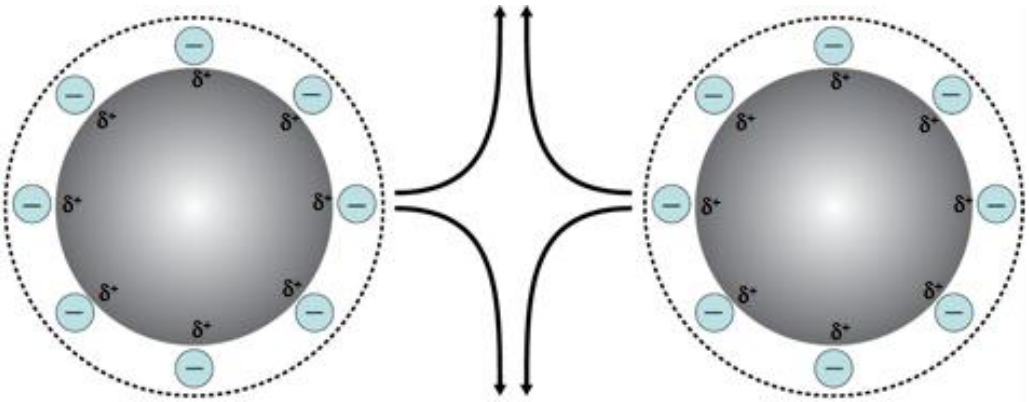

Figure 2.1. Anions approaching and adsorbing onto the nanoparticle surface induces a positive charge on the metal surface. The Coulomb repulsion between charged particles prevents agglomeration.

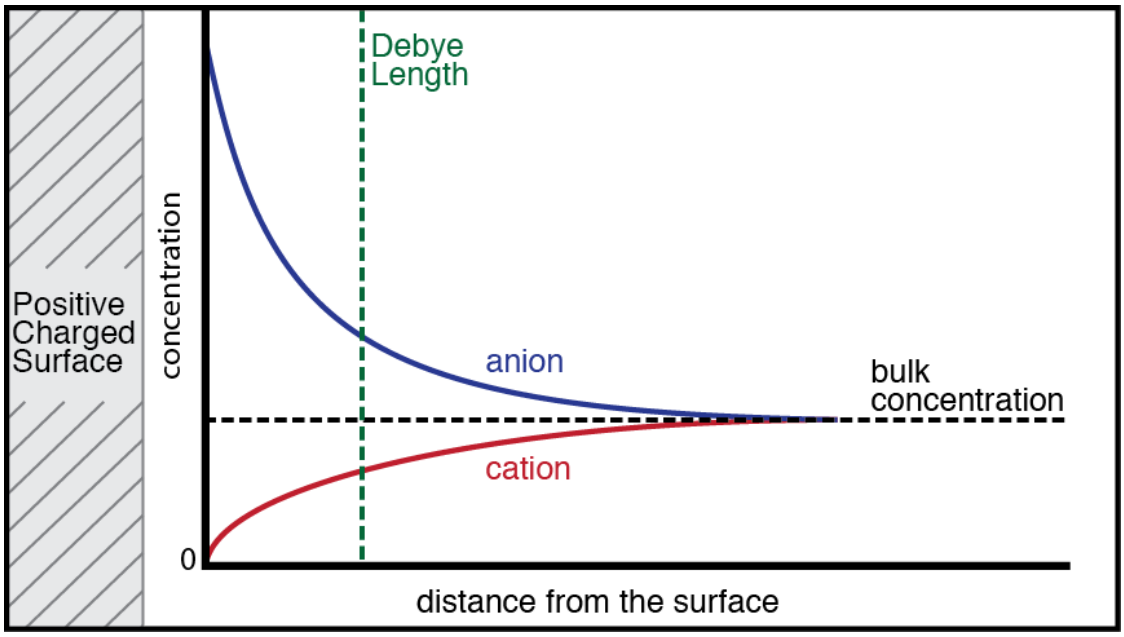

Figure 2.2. General plot of the change in concentration of anions (blue curve) and cations (red curve) vs. distance from a positive charged surface. The black dashed line represents the bulk concentration of the solution and the green dashed line represents the Debye length.

$$\kappa^{-1} = \sqrt{\frac{\varepsilon_r \varepsilon_0 RT}{2F^2 C_0}} \longrightarrow \kappa^{-1} \approx \sqrt{\frac{\varepsilon_r}{C_0}} \qquad \textbf{(Eq. 2.2)}$$

ε_o = permittivity of free space (C^2/J·m)
R = gas constant (J/mol·K)
T = temperature (K)
F = Faraday constant (9.6485 x 10^4 C/mol)

In water (ε = 80) with 1M monovalent anions, the Debye length is about 0.3 nm – the approximate length of a water molecule. The greater the Debye length, the more the particles are kinetically stabilized from agglomeration. However, the nanoparticle synthetic method employed, described in greater detail later in this chapter, takes into account the solubility (or insolubility) of the ions in THF to kinetically stabilize the nanoparticles.

2.2 Solution Phase Co-reduction Method

In the literature, many slight variations of nanoparticle synthesis via reduction of metal ions in solution exist.[22,23,31,34-36] Generally, the method involves the dissolution of the metal precursor (or precursors for multimetallic nanoparticle compositions) in a suitable solvent, followed by a reduction of the metal cations to a zero-valent state as depicted in Fig. 2.3. Reduction in solvents that do not react with the zero valent metal atoms or that do not bind too strongly to the metals, allows the formation of small particles by creating metal-metal bonds. Careful consideration must be given to choosing the right metal precursors, reducing agent, and solvent to avoid unwanted byproducts that may coordinate strongly to the particle surfaces. For example, dissolving Pt(II) acetylacetonate in THF followed by reduction with n-

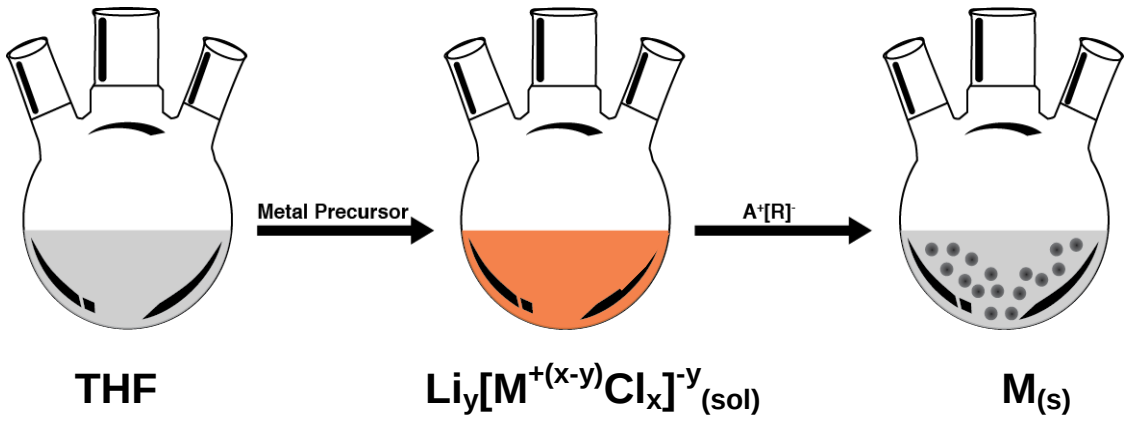

Figure 2.3. Basic schematic of a solution-phase reduction method of synthesizing nanoparticles. A metal precursor, in this case a ternary Li-M-chloride, is dissolved in a solvent followed by a reduction step to yield metal nanoparticles in solution.

Butyllithium (in hexanes) leaves particles coated with an organic residue, observable as a large weight loss when the product is heated in air to 500^{o}C (roughly 35%).[37] The observed weight loss arises from a side reaction between the reducing agent and the solvent (n-Butyllithium added to THF solution will yield an orange colored gel), and/or from the adsorption of acetylacetonate, which is present in solution after reduction. The major advantage of this direct method of nanoparticle synthesis is its simplicity. However, due to the stringent conditions that must be met to ensure dispersed nanoparticles with clean surfaces, finding the appropriate specified conditions can be challenging.

2.2.1 Complete Dissolution of the Metal Precursor

The physical and chemical properties of a material are highly dependent on its atomic composition. Several factors in the synthetic process are critical to minimizing compositional variance among as synthesized nanoparticles, one of which is ensuring complete dissolution of the precursors in solution. Other factors, such as the rate of reduction (both physical and chemical reduction rates), and the size of the as synthesized nanoparticles, will be discussed in further detail later in this chapter. Though some compositional spread (as well as a range in particle size) is unavoidable when no surfactant is present, maximizing nanoparticle homogeneity is key to forming single-phase ordered intermetallic nanomaterials, many of which (those that are "line-phases") only form over a narrow compositional range. Samples with a wide compositional spread may show mixed phases or require high annealing temperatures (so particles can grow and achieve the required atomic stoichiometry) to form the

ordered intermetallic phase.

To address this issue, careful selection of the metal precursors is done to ensure complete dissolution and thus homogeneous precursor solution. The homogeneous solution, while vigorously stirring, is rapidly reduced with a strong reducing agent (one where the reduction potential is much more negative than that of the metal cations). The reduction of each metal should happen almost instantaneously on collision with the reducing agent, minimizing the reduction and condensation of most of one metal before the reduction of the less electronegative metals.

Since THF is quite stable under a wide variety of potentials (-3.0 to +1.4V)[38a] and it is generally weakly coordinating to most metals, it is the solvent of choice. THF also has a dielectric constant of 7.6 and able to dissolve a wide range of nonpolar and polar chemical compounds.[38b] Though some metal chlorides ($FeCl_3$ for example) readily dissolve in THF, some are insoluble ($NiCl_2$) or have low solubility ($PtCl_4$). In certain situations, the addition of LiCl to the solution will allow the metal chloride to dissolve completely in THF. Taking $PtCl_4$ as an example, because of its polymeric structure, dissolution occurs by breaking the chloride bridging ligands. The addition of 2LiCl to $PtCl_4$ will yield Li_2PtCl_6 (or $2Li(THF)_4^+ + PtCl_6^{-2}$, this dissolution is determined by the high enthalpy of solution of Li^+ in THF),[38c] which is highly soluble in THF. There are some cases, $NiCl_2$ for example, where the addition of LiCl salt to the metal chloride/THF solution does not cause the metal chloride to dissolve at room temperature. This appears to be a kinetic problem. In these extreme cases, a ternary lithium metal chloride precursor is synthesized (when not commercially available) by mixing stoichiometric amounts of LiCl and the metal chloride (based on information

from the corresponding phase diagram) and annealed in a furnace for up to four weeks. A complete summary of THF-soluble metal precursors used in this method, as well as the source of the precursor is listed in Table 2.1.

Table 2.1 List of THF soluble metal precursors (left column) along with the chemical source. **(sol)** subscript denotes THF soluble species.

THF Soluble Metal Precursor	Chemical Source
$AuCl_{3(s)} \rightarrow AuCl_{3(sol)}$	$AuCl_{3(s)}$ from Sigma-Aldrich
$PdCl_{2(s)} + 2LiCl_{(sol)} \rightarrow Li_2[PdCl_4]^{-2}{}_{(sol)}$	$PdCl_{2(s)}$ from Strem Chemicals Inc.
$AgCl_{(s)} + LiCl_{(sol)} \rightarrow Li[AgCl_2]^{-}{}_{(sol)}$	$AgCl_{(s)}$ from Strem Chemicals Inc.
$PtCl_{4(s)} + 2LiCl_{(sol)} \rightarrow Li_2[PtCl_6]^{-2}{}_{(sol)}$	$PtCl_{4(s)}$ Sigma-Aldrich, 99.9%
Li_2CuCl_4/THF 0.1M soln.	Li_2CuCl_4/THF soln. from Alfa Aesar
$BiCl_3 + 3LiCl_{(sol)} \rightarrow Li_3[BiCl_6]^{-3}{}_{(sol)}$	$BiCl_3$ from Strem Chemicals Inc.
$FeCl_{3(s)} \rightarrow FeCl_{3(sol)}$	$FeCl_{3(s)}$ from Sigma-Aldrich
$MoCl_{5(s)} \rightarrow MoCl_{5(sol)}$	$MoCl_{5(s)}$ from Sigma-Aldrich
$SnCl_{2(s)} + LiCl_{(sol)} \rightarrow Li[SnCl_3]^{-}{}_{(sol)}$	$SnCl_{2(s)}$ from Sigma-Aldrich
$Li_6NiCl_{8(s)} \rightarrow Li_6[NiCl_8]^{-2}{}_{(sol)}$	($6LiCl + NiCl_2$) annealed @ 540^{o}C for 672hrs --rapid quench to room temp. $NiCl_{2(s)}$ Sigma-Aldrich 99.99%
$Li_2CoCl_{4(s)} \rightarrow Li_2[CoCl_4]^{-2}{}_{(sol)}$	($2LiCl + CoCl_2$) annealed @ 400^{o}C for 162hrs. $CoCl_{2(s)}$ Sigma-Aldrich 99.9%
$NbCl_{5(s)} \rightarrow NbCl_{5(sol)}$	$NbCl_{5(s)}$ from Strem Chemicals Inc.
$CrCl_3(THF)_{3(s)} \rightarrow CrCl_{3(sol)}$	$CrCl_3(THF)_3$ from Strem Chemicals Inc.
$ZnCl_2$/THF 0.5M soln.	$ZnCl_2$/THF soln. from Sigma-Aldrich
$TaCl_5 \rightarrow TaCl_{5(sol)}$	$TaCl_5$ from Sigma-Aldrich
$VCl_4(THF)_{2(s)} \rightarrow VCl_{4(sol)}$	$VCl_4(THF)_2$ from Sigma-Aldrich
$TiCl_4(THF)_{2(s)} + 2LiCl_{(sol)} \rightarrow Li_2[TiCl_6]^{-2}{}_{(sol)}$	$TiCl_4(THF)_2$ from Sigma-Aldrich
$WCl_{6(s)} \rightarrow WCl_{6(sol)}$	WCl_6 from Strem Chemicals Inc.
$MnCl_{2(s)} + 2LiCl_{(sol)} \rightarrow Li_2[MnCl_4]^{-2}{}_{(sol)}$	$MnCl_{2(s)}$ from Sigma-Aldrich

Another important quality of THF is its stability under very reducing conditions; not only does lithium triethylborohydride (super hydride) come in a solution of THF, but sodium naphthalide, with a reduction potential of roughly -2.5 V, is made in THF.[39] By using reducing agents that are stable with the solvent, the concern of possible contaminants from unwanted side reactions between the solvent and reducing agent can be eliminated. This solution-phase coreduction method is typically followed by a heat treatment step to obtain ordered intermetallic nanomaterials, at significantly high temperatures (200 to 800^{o}C). At this temperature, many organics adsorbed onto the particle surface will decompose, leaving behind a metal surface coated with carbon that is difficult to remove. THF is generally weakly coordinated to the metal particles and can be removed by gentle heating under vacuum.

Organic anions, if present in the precursors, generally have a higher binding energy to the nanoparticle surface. Upon heating they generally decompose before desorbing, leaving surface residues. For this reason, no organic ligands are used in the synthesis discussed here, rather only chloride precursors.

2.2.2 Choice of Reducing Agent

Due to their widespread applications as catalysts, metals precipitated from aqueous solutions continue to be a thoroughly investigated subject.[13-18,22,23] The precipitation of metals from aqueous or nonaqueous solutions typically requires the chemical reduction of a metal cation. Reducing agents take many forms, the most common of which are gaseous H_2, hydrides (alkali metal borohydrides and super

hydrides, lithium aluminum hydride), and alkali metal naphthalides.

Typical reduction reaction of a transition metal cation "M" and corresponding oxidation reaction of some species "X":

$$\mathbf{M^{n+}_{(sol)} + ne^- \rightarrow M^0_{(s)}} \qquad \textbf{Reduced}$$

$$\mathbf{X^{(m-n)} \rightarrow X^m + ne^-} \qquad \textbf{Oxidized}$$

In order for the electron transfer to occur, the Gibbs free energy, ΔG^o, must be favorable (negative). As a matter of convention, the favorability of oxidation or reduction processes is reflected in the standard electrode potential, E^o, calculated from the two corresponding electrochemical half-reactions. E^o is related to the free energy by equation 2.3.

$$\mathbf{\Delta G^o = -nFE^o} \qquad \textbf{(Eq. 2.3)}$$

n = moles of electrons per mole of product
F = Faraday constant (96,485 C/mol)

If $\mathbf{E^o_{cell} > 0}$**, then the process is spontaneous**
If $\mathbf{E^o_{cell} < 0}$**, then the process is nonspontaneous**

$$\mathbf{E^o_{cell} = E^o_{cathode} - E^o_{anode}} \qquad \textbf{(Eq. 2.4)}$$

From equation 2.4, the reduction of any metal with E^o more positive than the reducing agent should be possible at room temperature. A list of various reducing agents and their corresponding electrode potentials in water are given in table 2.2.[39,40] A list of metal ions and their corresponding reduction potentials in acidic and basic aqueous solution is given in table 2.3.[41] These are a rough guide to selecting such reagents for

use in non-aqueous solvents, since the half cell potentials are solvent dependent. This dependency is expected since the solvent is typically coordinated to the reactant, especially for cations. THF behaves as a Lewis base[38] and coordinates strongly to Li^+ and to metal chlorides with unsaturated coordination spheres (which are Lewis acids to some degree).

The use of borohydrides, such as $NaBH_4$, as a reducing agent has been shown to incorporate boron impurities into the nanoparticle in certain metal systems, sometimes forming metal borides.[42] To minimize boron contamination, hydride anions can be used as a "clean" alternative. The hydride anion, H^-, is the simplest possible anion, consisting of two electrons and a proton. Hydrogen has a relatively low electron affinity, 72.77 kJ/mol, and reacts exothermically with protons (ΔH = -1676 kJ/mol). The strength of the H—H bond (ΔH_{BE} = 436 kJ/mol) coupled with its low electron affinity makes the hydride ion a strong reducing agent. Free hydride anions only exist in extreme conditions; typically compounds have hydrogen centers with hydridic character. The structure of lithium (and potassium) triethylborohydride ($Li^+[B(Et)_3H]^-$), in which H is formally H^-, allows the compound to be a very strong hydride source while the ethyl ligands improve solubility in THF. Hydrogen is more electronegative than boron (2.20 for hydrogen vs. 2.04 of boron using the Pauling scale of electronegativity), which causes the B-H bond to be polarized with hydrogen having a partial negative charge. This polarization, along with the polarization of the B-Et bonds leads to its high reactivity with electron accepting atoms.[43]

Table 2.2 List of various reducing agents with their corresponding half-reaction and electrode potentials in aqueous solutions.

Reducing Agent	Half-reaction	Electrode Potential E^o (V)
Hydrogen	$2H^+ + 2e^- \rightarrow H_2$	**0.00**
Borohydride	$B(OH)_3 + 7H^+ + 8e^- \rightarrow BH_4^- + 3H_2O$	**-0.48**
Hydride	$H_2 + 2e^- \rightarrow 2H^-$	**-2.25**
Naphthalide	$C_{10}H_8 + e^- \rightarrow C_{10}H_8^-$	**-2.50**

By comparing the electrode potentials of various reducing agents in table 2.2

with the standard electrode potentials of various metal cations in table 2.3, one could assume hydrides, such as super hydride, alkyl metal triethylborohydride ($A^+[BEt_3H]^-$ A = Li, Na, or K), would be enough to reduce all these metals to their zero-valent state. However, the formation of stable hydrides or meta-stable hydride intermediates with certain metals can lead to non-homogeneous multimetallic nanoparticle compositions. Nucleophilic main group hydrides convert many transition metal halides and cations into the corresponding hydrides. Fig. 2.4 highlights a portion of the periodic table and the known metal hydride compounds. Those in green fonts are stable at standard temperature and pressure while those in red typically exist at high pressure and decompose under ambient conditions. Upon heating under vacuum, all metal hydrides decompose to give the free metal and $H_{2(g)}$. The term hydride is used to indicate compounds of the type M_xH_y and does not indicate the ionic or covalent nature of the bonding.

Table 2.3 Standard reduction potential (vs. NHE) of various metal ions in acidic and

basic aqueous solution (when the data is available). Source: WebElements [http://www.webelements.com/]

Metal ion	E^o (V)	
	Acid	Base
$Au^{+3} \rightarrow Au_{(s)}$	1.52	
$Pt^{+4} \rightarrow Pt_{(s)}$	1.01	
$Pd^{+2} \rightarrow Pd_{(s)}$	0.95	
$Ag^{+1} \rightarrow Ag_{(s)}$	0.80	0.34
$Ru^{+3} \rightarrow Ru_{(s)}$	0.62	
$Cu^{+2} \rightarrow Cu_{(s)}$	0.34	
$Bi^{+3} \rightarrow Bi_{(s)}$	0.32	
$Fe^{+3} \rightarrow Fe_{(s)}$	-0.04	-0.88
$W^{+6} \rightarrow W_{(s)}$	-0.09	-1.07
$Sn^{+2} \rightarrow Sn_{(s)}$	-0.14	-0.91
$Mo^{+4} \rightarrow Mo_{(s)}$	-0.15	-0.98
$Ni^{+2} \rightarrow Ni_{(s)}$	-0.26	-0.72
$Co^{+2} \rightarrow Co_{(s)}$	-0.28	-0.73
$V^{+4} \rightarrow V_{(s)}$	-0.55	-0.40
$Nb^{+5} \rightarrow Nb_{(s)}$	-0.65	
$Cr^{+3} \rightarrow Cr_{(s)}$	-0.74	-1.33
$Zn^{+2} \rightarrow Zn_{(s)}$	-0.79	-1.26
$Ta^{+5} \rightarrow Ta_{(s)}$	-0.81	
$Ti^{+4} \rightarrow Ti_{(s)}$	-0.86	-1.90
$Mn^{+2} \rightarrow Mn_{(s)}$	-1.18	-1.56

Figure 2.4 Periodic table showing the currently known metal hydride compositions. The compositions in red denote non-stable hydrides at ambient temperature and the compositions in green are stable hydrides at ambient temperature

To reduce metals that do form stable metal hydrides, we can use alkali metal naphthalide as a reducing agent. The alkali metal naphthalides are prepared by stirring the metal with naphthalene in THF, which makes a dark green solution. The radical naphthalide anion is strongly basic with a reducing potential near -2.5 V vs. RHE, thus able to reduce even the most electropositive metals (except those from group I & II) without forming stable hydrides or hydride intermediates. Since naphthalene is aromatic, the only concern is that it can coordinate strongly onto metal surfaces. On a Pt (1,1,1) surface, naphthalene has been shown to have ΔG_{ads} between 28-132 kJ/mol (from DFT calculations, naphthalene has been shown to adsorb onto Pt (111) surface in five different configurations with adsorption energies of 28, 51, 73, 92, and 132 kJ/mol).[44] The calculations assume a flat Pt (111) surface, on the curved surface of Pt nanoparticles (< 2 nm particle size), the adsorption energy may be significantly less. By heating at 150^{o}C (using a 600 watt, 60 Hz heat gun) under vacuum for 15-20 minutes, white crystals of naphthalene condense on the upper portion of the tube, indicating the removal of some naphthalene species. However, when Pt nanoparticles are synthesized with lithium naphthalide reducing agent and annealed at temperatures above 400^{o}C in an evacuated silica tube, the inside of the tube develops a black film, suggesting naphthalene is still present on the particles surface and decomposes upon annealing. However, when potassium naphthalide is used, after annealing, there does not seem to be any observable evidence of organics decomposing on the tube surface. Fig. 2.5a is a picture of the silica tubes of Pt nanoparticles annealed at 600^{o}C for 24hrs, reduced with lithium and potassium naphthalide; from the picture, it is clear that the inside of the tube containing Pt reduced with lithium naphthalide is darkened,

indicating that residual organics have decomposed. TGA under a flow of air of both platinum samples is shown in Fig. 2.5b and c. The TGA of Pt reduced with potassium naphthalide shows a total percent weight loss of roughly 4% while Pt reduced with lithium naphthalide showed a weight loss of roughly 26%. TGA of PtNi product made from $KB(Et)_3H$ and $LiB(Et)_3H$ reducing agents (using lithium metal chloride precursors) showed a 6% and 9% weight loss in air respectively.[37] This observation is consistent with the formation of insoluble KCl on the nanoparticle surface, which prevents naphthalene from binding to the Pt.

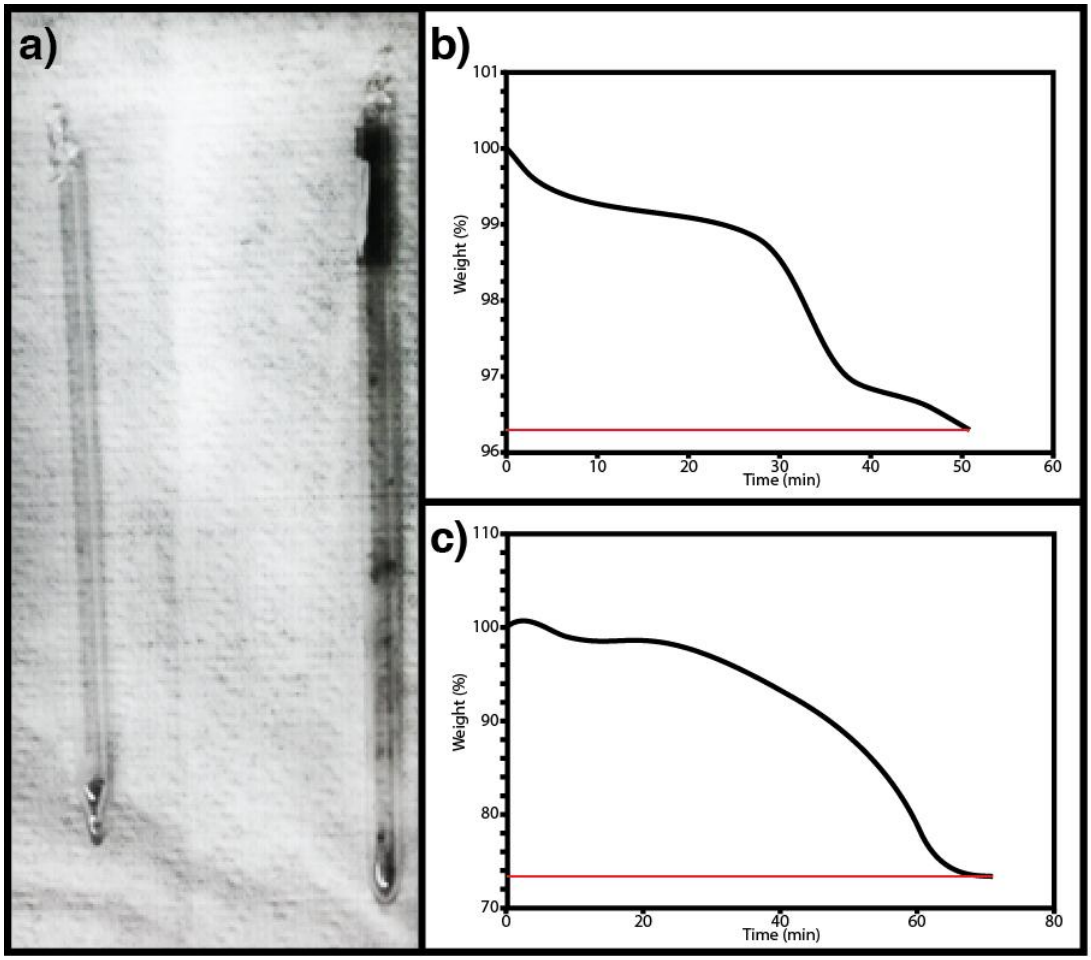

Figure 2.5 a) Pt nanoparticles sealed in an evacuated silica tube, annealed at 600^{o}C for 24hr using Potassium Naphthalide (left) and Lithium Naphthalide (right) as reducing agents. TGA in air (from room temperature to 550^{o}C at a rate of 10^{o}C/min) of annealed Pt nanoparticles using Potassium Naphthalide b) and Lithium Naphthalide c) as a reducing agents.

2.2.3 Reduction Conditions

Reaction conditions, such as temperature and concentration, are known to affect the particle size of as-synthesized nanoparticles.[45] The size of as-synthesized nanoparticles may, inadvertently, have an affect on obtaining single phase ordered nanomaterials as well as the temperature required to transform from alloy-to-ordered phase. In multimetallic systems, particle size does have an effect on atomic uniformity among individual particles. Statistically speaking, samples with smaller average particle sizes will have a higher range of atomic composition from particle-to-particle than samples with larger average particle sizes. This is analogous to the statistical outcome of a coin flip being either heads or tails: large sample sizes (more than 30 flips) will show statistical outcomes near 50:50, whereas small sample sizes (< 5 flips) way show outcomes as extreme as 100:0 head-to-tales. In a bimetallic system with a uniform particle size of 1 nm, the majority of the particles will lie within +/- 10% of the target stoichiometry compared to +/- 2% in 5 nm particles (this calculation assumes particles are uniform in size, 1 nm is 5 metal atoms, and nanoparticles are treated as perfect spheres).[50] Thus, when targeting phases that have a narrow compositional range of stability, having an average particle size that is too small (large compositional variation among particles) could lead to multiphase samples or require higher annealing temperatures to order, allowing particles to agglomerate and obtain the stable atomic composition (Fig. 2.6).

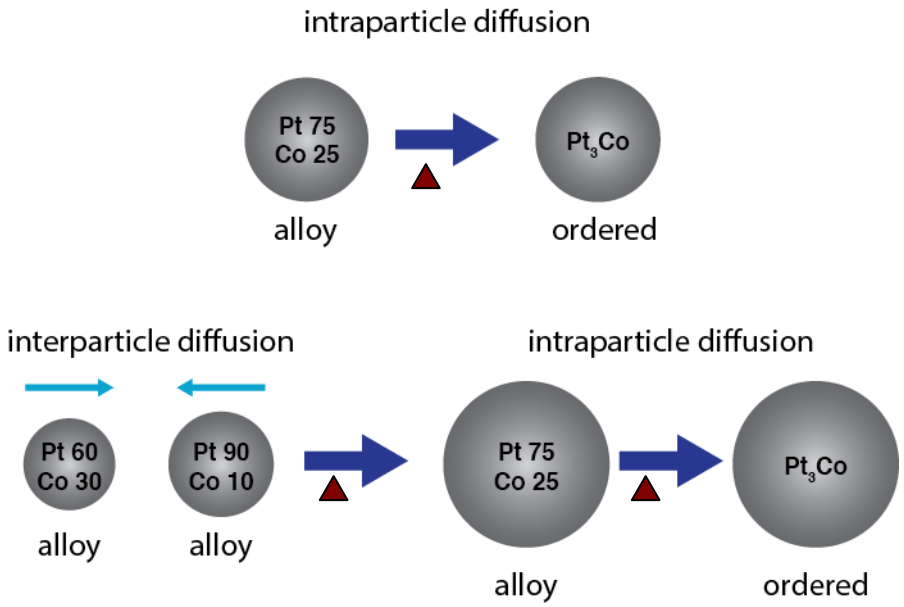

Figure 2.6 Atoms in alloy nanoparticles with compositions within the ordered phase range diffuse within the particle (given enough thermal energy) to obtain the ordered intermetallic phase Pt_3Co. Alloy particles with compositions outside the ordering range must diffuse together, when the composition is within the ordering range, intraparticle diffusion occurs and the ordered phase is obtained, often requiring higher annealing temperatures and/or annealing time.

2.2.4 Diffusion: Transitioning from Alloy to Ordered Phase

In multimetallic systems, the use of reducing agents with highly negative reduction potentials will likely reduce metal ions in solution non-preferentially, producing nanoparticles with atomic compositions near the target stoichiometry. However, the nanoparticle is usually an alloy, the atoms within the particles randomly occupy the atomic sites within the crystal structure. Given enough thermal energy and time, the atoms will rearrange into their most thermodynamically stable configuration. If the particles are in the appropriate stoichiometric window, according to the bulk phase diagram, the particles might be expected to form an ordered intermetallic crystal. As the particle becomes smaller and smaller, one might also expect that the surface energies could lead to surface segregation (preference of one type of atom to be at the surface) and/or to suppression of the ordered structure.

The process of ordering is centered on atomic diffusion, which is a process whereby the random thermally activated movement of atoms in a solid results in the net transport of atoms. The diffusion coefficient, D, is directly influenced by the temperature as depicted in equation 2.5. The natural log of equation 2.5 is given in equation 2.6. Plotting ln D vs. 1/T will give a straight line, the slope of which is a measure of the activation energy and the y-intercept is D_o; a larger activation energy (or slope) results in a smaller diffusion coefficient. A plot of diffusivity vs. reduced reciprocal temperature (normalized by the melting temperature, T_m) for various diffusion paths in fcc metals is given in Fig. 2.7.[46] From this figure, it is apparent that bulk diffusion is much lower than surface or grain boundary diffusion.

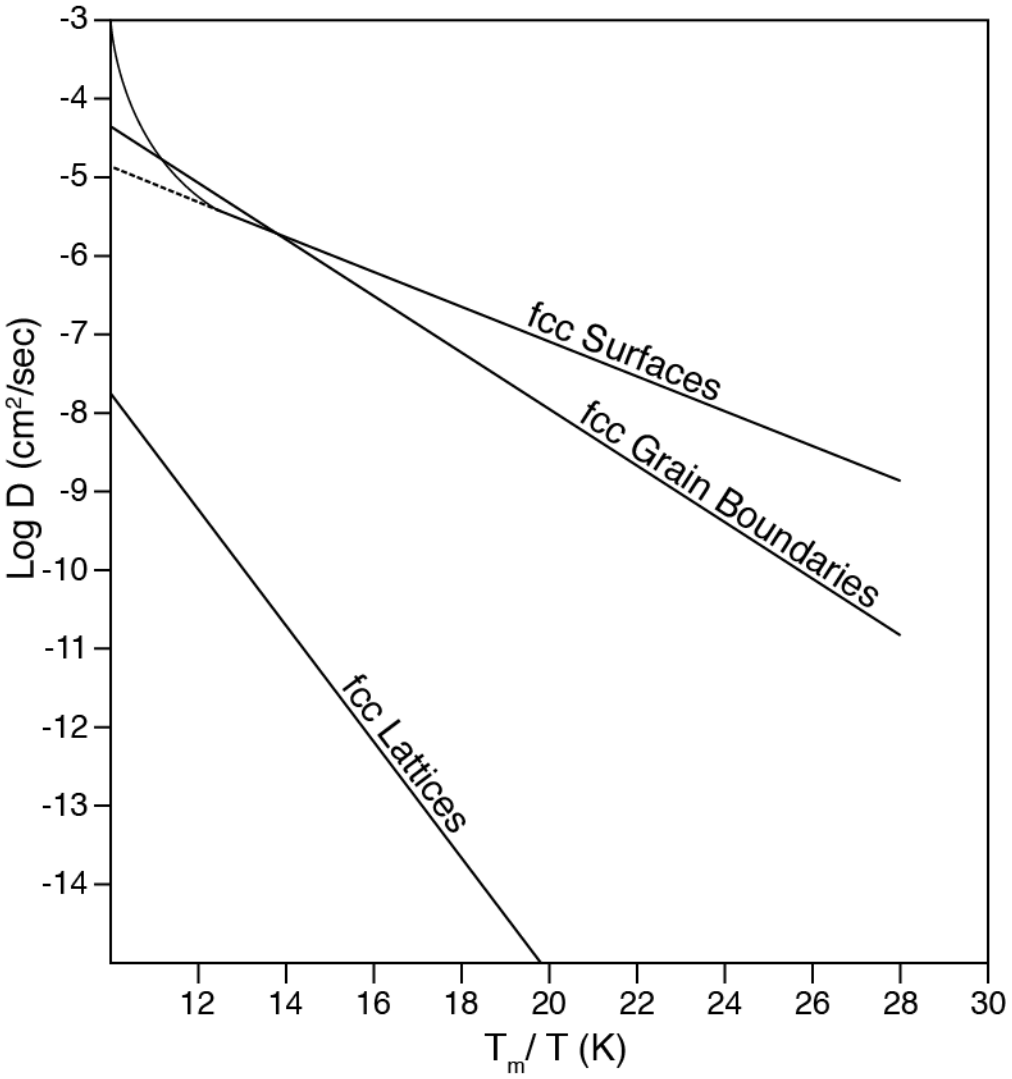

Figure 2.7 Diffusivity vs. reduced reciprocal temperature for various diffusion paths in fcc metals

Diffusion coefficient:

$$D = D_o e^{-Ea/RT} \quad \textbf{(Eq. 2.5)}$$

D_o = prefactor (cm^2/s)

E_a = activation energy for diffusion

R = gas constant (8.31 J/mol·K or 8.662 x 10^{-5} eV/atom·K)

T = temperature (K)

Natural log of Eq. 2.3: Plot of log (D) vs. (1/T) gives a linear representation of diffusion kinetics

$$\ln D = \ln D_o - (E_a/R)(1/T) \quad \textbf{(Eq. 2.6)}$$

Nanoparticles (typically below 20 nm) have been known to experience lower melting temperatures than their bulk counterparts.[51] The lowering of the melting temperature of small particles can be estimated using equation 2.7.[51,52] From the equation, the melting temperature of a small particle is inversely related to it's radius, with smaller particles showing a greater change in melting temperature compared to the melting temperature of the bulk material.

Estimation of the melting temperature of small particles:

$$\Delta\theta = \frac{2T_m\sigma}{\rho L r} \qquad \textbf{(Eq. 2.7)}$$

θ = melting temperature of a small particle

T_m = melting temperature of the bulk material

σ = surface tension coefficient

ρ = density of the material

L = latent heat of fusion

r = radius of the particle

This equation matches experimental results when plotting the melting temperature of Au and CdS as a function of particle size; for gold particles in the 1 nm range, the melting temperature can be as much as 900^{o}C lower than the corresponding bulk value (a shift of 1000^{o}C for 1 nm CdS particles).[52]

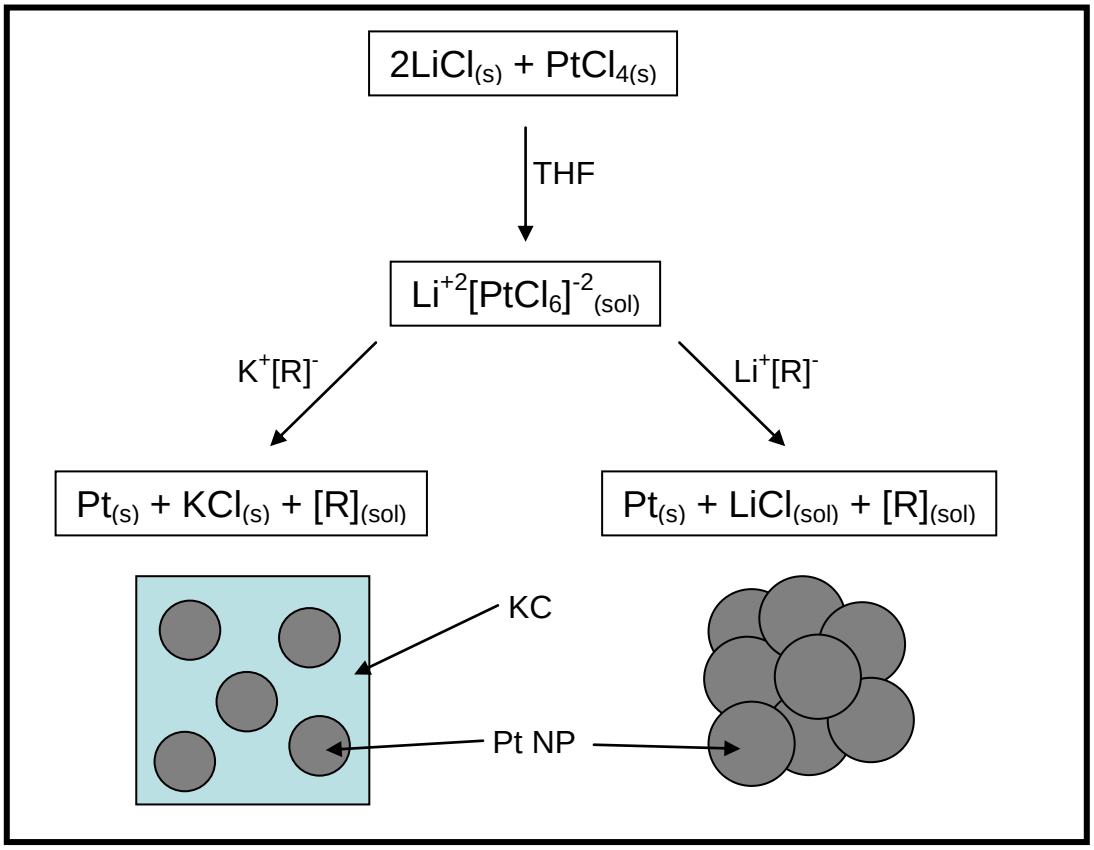

Figure 2.8. Schematic representation of Pt nanoparticle synthesis using either a potassium or lithium reducing agent. When using a potassium reducing agent ($K^+[R]^-$), the nanoparticles are trapped within KCl crystals since KCl is insoluble in THF. When using a lithium reducing agent ($Li^+[R]^-$), the nanoparticles agglomerate together.

As stated previously, one reason of using chloride precursors is to minimize possible surface contamination by neutral or anionic organic molecules. Also, when using alkali metal reducing agents (such as Li or K triethylborohydride or naphthalide) to make nanoparticles, the salt byproduct of the reaction (either LiCl or KCl depending on the reducing agent employed), can be used to kinetically stabilize the as synthesized nanoparticles. Stabilization of the nanoparticles is determined by the solubility of the salt byproduct in THF. LiCl is highly soluble in THF and offers no protection from particle agglomeration. In contrast, KCl is not soluble in THF and crystallizes around the nanoparticles precipitating both out of solution. A schematic representation of the synthesis of Pt nanoparticles using either lithium or potassium reducing agents is depicted in Fig. 2.8. An SEM and TEM image of Pt nanoparticles prepared with potassium triethylborohydride are depicted in Fig. 2.9a and b. The SEM image shows a cubic salt crystal with dimensions of roughly 10 microns; the surface of the crystal is smooth with little evidence of nanoparticles on the surface. The TEM image of the same sample shows the nanoparticles somewhat dispersed within the salt crystal (under high beam intensities, 120 keV, the salt readily vaporizes and the particles migrate closer together). Two SEM images of Pt nanoparticles reduced with lithium triethylborohydride are depicted in Fig. 2.9c and d. From the image, it is apparent that the nanoparticles have agglomerated together into micron-sized spheres; on higher magnification, the particles have sintered, thus dispersion after this point is impossible. It has also been shown that by adding additional LiCl to the reaction solution and reducing with an equimolar excess of the potassium reducing agent to increase the ratio of KCl to nanoparticles, thereby increasing the particle-to-particle

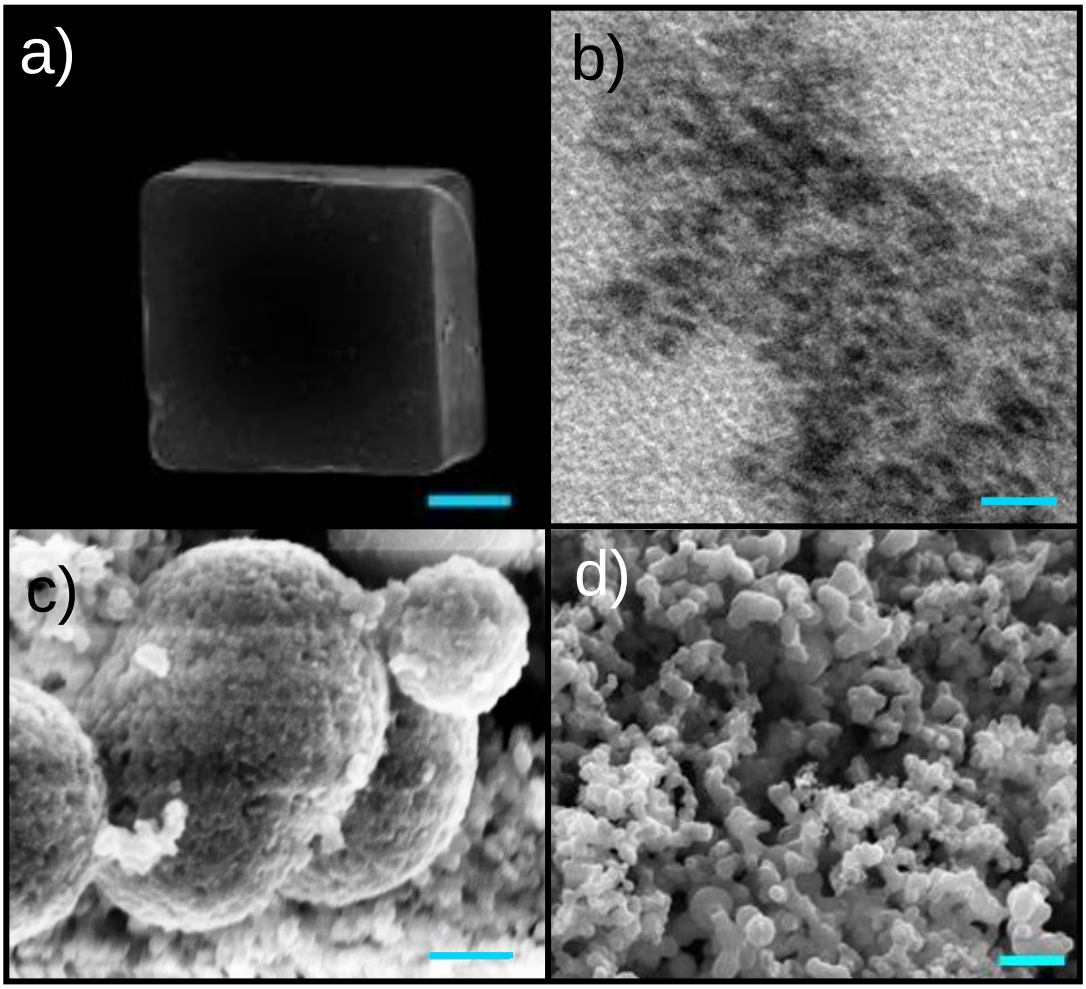

Figure 2.9. a) SEM image of $Li^{+2}[PtCl_6]^{-2}$ reduced with potassium triethylborohydride and annealed at 400^{o}C for 24 hours. The large block like KCl crystal contains entrapped Pt nanoparticles. The scale bar denotes 2 μm. b) TEM image of the same sample with the scale bar representing 20 nm. The dark spots are Pt, blurred by charging of the KCl with the beam (operating at 120 keV). KCl is unstable and vaporizes causing the nanoparticles to agglomerate slightly. c) SEM image of $Li^{+2}[PtCl_6]^{-2}$ reduced with lithium triethylborohydride at room temperature. The scale bar is 500 nm. f) SEM image of the same image with the scale bar representing 25 nm. Particle agglomeration is clearly evident.

distance within the KCl matrix.[47] The melting point of KCl is 770^{o}C, offering protection from agglomeration over a moderately broad temperature range. The ability to increase the particle-particle distance within the KCl matrix, adjusting annealing temperature and time are the three parameters that are adjusted to fine-tune particle size while forming ordered intermetallic nanoparticles.

2.3 Experimental

2.3.1 Synthesis of Binary Alloys and Ordered Intermetallics

Pt_3Co nanoparticles were synthesized in a manner similar to that described in the previous section. Briefly, $PtCl_4$ (100 mg, 0.30 mmol; Sigma-Aldrich, 99.9%), LiCl (25.2 mg, 0.60 mmol; Alfa Aesar, 99.9%), and Li_2CoCl_4 (22mg, 0.10 mmol; made from annealing LiCl and $CoCl_2$ (Sigma-Aldrich, 99.9%) in a 2:1 ratio at 400^oC for 1 week) were dissolved in 25 mL dry THF in a 100 mL three-neck round-bottom flask. After the mixture was stirred for at least 20 min in an Ar atmosphere glove-box, 2.75 mL of reducing agent (either lithium triethylborohydride ($LiB(Et)_3H$) or potassium triethylborohydride ($KB(Et)_3H$)--1.0 M in THF, Sigma-Aldrich) was added rapidly via syringe injection. The clear green solution turns black instantly along with the formation of H_2 gas bubbles, indicating successful reduction of the metal ions to metal nanoparticles. The solution is then transferred to a 50 mL Teflon centrifuge tube, capped and fastened with a septum and copper wire to minimize exposure to air. The solution is spun at 5000 rpm for 10 minutes in a centrifuge, precipitating out the black nanoparticles. The clear supernatant is removed under Ar via cannula needle and the black powder is washed three times with 25 mL of dry THF by repeating the centrifuge and cannula process, followed by a final rinse and removal with 25 mL dry hexanes. The black powder is then dried under vacuum via schlenk-line for at least an hour. The centrifuge tube is then backfilled with Ar and the nanoparticles are exposed to air slowly by inserting a needle through the top of the septum and letting it sit overnight (at least 12 hours as air slowly diffuses into the tube through the needle).

To transition from alloy to ordered intermetallic, the black powder is

transferred to a silica tube and sealed under vacuum. While under vacuum, the powder is gently heated using a heat gun (Master Appliance HG-201A corded master heat gun, 93-150^{o}C) to ensure all residual solvent is removed. The sample is then annealed at various temperatures and times (see Results section) in a tube furnace. Other binary phases were synthesized in a similar fashion and summarized in table 2.5.

2.3.2 Transfer of nanoparticles to carbon support

There are two variations we use to deposit nanoparticles onto a conducting carbon support and depend on the type of reducing agent used during nanoparticle synthesis. The direct method (using lithium based reducing agents) involves synthesizing the nanoparticles directly onto a support material while the indirect method (using potassium based reducing agents) synthesizes nanoparticles trapped within a KCl matrix and requires additional steps to "release" the particles onto a support material.

Direct Method: Metal precursors and an equivalent amount of Carbon Black (C-Blk, Vulcan X-72), to produce the desired catalyst-to-support mass ratio, is added to 25 mL of THF and stirred vigorously for 2 hours. The precursor/C-Blk solution is then reduced with a 20% excess amount of lithium reducing agent and allowed to stir for an additional 15 minutes. The catalyst/C product is then washed and cleaned in a similar manner as described in the previous section.

Indirect Method: The method used to transfer heat-treated nanoparticles to a carbon support material is similar to the method described in the literature.[47] Briefly, 4 mg of

Carbon Black (Vulcan X-72) is weighed out in a 2 mL vial with 1.5 mL of Ethylene glycol. The solution was sonicated for at least 1 hour. An appropriate amount of nanoparticle in KCl sample (to produce 1 mg of nanoparticles when targeting 20 weight% catalyst loading) is weighed out in a 25 mL scintillation vial and place in an ice bath; 2 mL of ethylene glycol is added to the sample and immediately ultrasonicated (Misonix Inc., Microson ultrasonic cell disruptor XL Model DU-2000; 0.5-1.5 mL probe) for 1 minute at power level 3. After 1 minute, the sonicated C-Blk/ethylene glycol soln. is added, via syringe, to the nanoparticle/ethylene glycol solution and sonicated for an additional 15 minutes. After sonication, the sample is centrifuged at 3000 rpm for 1 hour. The clear supernatant is removed leaving behind a black powder. The black powder is washed five times with 15 mL Millipore water, repeating the centrifuge and removal sequence. After the final wash and supernatant removal, the black powder is dried in air at 150^{o}C for 1 hour to yield nanoparticles dispersed on carbon support (NP/C).

2.3.3 Material characterization

The nanoparticle phase and domain size were determined using XRD (Rigaku Ultima VI diffractometer, Cu K_{α} (λ = 0.15418 nm) radiation source). Nanoparticle size and degree of dispersion was determined from TEM images (Tecnai T12, 120 kV). Atomic composition of the material was characterized by EDX coupled to the SEM (LEO-1550 field emission SEM). TGA (Q50 TA Instruments) analysis under a flow of air was used to determine carbon to metal ratio by oxidizing carbon to CO_2.

2.4 Results and Discussion

2.4.1 Comparison of Potassium vs. Lithium reducing agents

As stated previously, depending on the reducing agent used (either lithium or potassium based), the salt that forms from the reduction reaction will affect the particle growth kinetics. XRD of Pt_3Co nanoparticles reduced with LBH and KBH and annealed at various temperatures for 24 hours is shown in Fig. 2.8. The sample reduced with KBH shows intense KCl peaks that drown out the diffraction peaks from the nanoparticles. To better compare the two samples, XRD was taken after KCl is removed by washing the sample three times with Millipore water and dried at 125^{o}C for one hour. The domain size is estimated using the Scherrer equation[48]:

$$\tau = (K\lambda)/(\beta \cos\theta)$$

τ = domain size

K **= shape factor (typically 0.9, varies some with crystallite shape)**

λ = X-ray wavelength

β = FWHM (radians)

θ = Bragg angle

The domain size may be smaller or equal to the grain size and not applicable to grains larger than about 100-200 nm. In the Scherrer equation, β is inversely proportional to the domain size, thus smaller particles will have wider diffraction peaks measured as the full width at half max (FWHM).

Aside from estimating particle size, the phase information (the transition from alloy to ordered) can be monitored via XRD. Using Pt_3Co as an example, alloy Pt_3Co adopts a disordered face-centered-cubic (fcc) structure type with Pt and Co atoms randomly occupying (in a 3:1 ratio) the 4(a) Wyckoff positions of the cubic unit cell as depicted in Fig 2.10. Due to the smaller atomic size of Co atoms compared to Pt, the XRD peaks will shift to higher angles, thus the XRD pattern of Pt_3Co alloy shows the same characteristic peaks as that of pure Pt, only slightly shifted to higher angles. At higher angles, expected peak shifts from Pt to intermetallic Pt_3Co are several degrees, which is easy to observe.

Upon ordering, the Pt and Co atoms occupy fixed points in the unit cell, resulting in a lowering of the overall symmetry and the appearance of additional diffraction peaks, also referred to by us as ordering peaks (due to the appearance of the peaks upon ordering). By comparing the ratio of the intensity of one of the ordering peaks with one of the main peaks (for instance the (1,1,0) peak at 32.84 2-theta with the (1,1,1) peak at 40.51 2-theta), with the ratio of the same peaks in the bulk ordered system, the degree of ordering can be estimated. The degree of ordering, or percent ordering, of Pt_3Co nanoparticles synthesized with different reducing agents and annealed at various temperatures is given in Table 2.4.

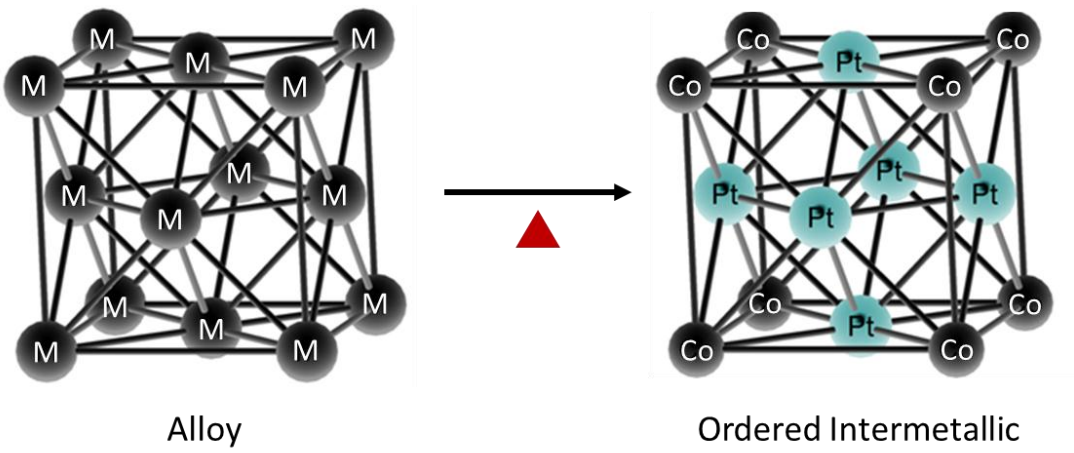

Figure 2.10 Unit cell of Alloy and ordered fcc Pt_3Co

Table 2.4 Domain size and degree of ordering of Pt_3Co nanoparticles annealed at various temperatures for 24 hours. Degree of ordering was calculated from the XRD patterns by dividing the intensity of the (1,1,0) peak at 32.84 2-theta with the (1,1,1) peak at 40.51 2-theta and dividing that number by 0.122 (the ratio of peak intensities in fully ordered Pt_3Co from the database card # 04-006-7902).

Annealing Temperature (^oC) for 24hr	Domain Size (nm)		Degree of Ordering (%)	
	LBH	KBH	LBH	KBH
25	1.7	1.7	--	--
300	8.6	3.3	--	--
400	21.9	4.5	--	--
500	23.7	4.8	25	--
600	30.1	5.0	52	20

From Fig. 2.11 and 2.12, the nanoparticles reduced with LBH increase to a domain size of roughly 30 nm after annealing at 600^{o}C while the nanoparticles reduced with KBH increase to a domain size of roughly 6 nm after the same heat treatment. The appearance of ordering peaks are detected at a lower temperature in Pt_3Co reduced with LBH compared to KBH (500^{o}C vs. 600^{o}C), and is most likely due to faster interparticle diffusion in the sample without KCl since in that case, the particle-particle contact is extensive. The usefulness of KCl as a particle-size stabilizing agent reduces as the annealing temperature approaches the melting point of KCl, 770^{o}C. In cases where high surface area is not an important property, using lithium reducing agents would be ideal to synthesize intermetallic nanomaterials that order at low temperature. It is particularly notable that the sample prepared from LBH and annealed at 400^{o}C shows considerable growth in domain size (by diffraction), yet the ordered phase has not formed. This suggests either a kinetic barrier to nucleation or thermodynamic inhibition by surface energies. Since ordering is observed with KBH product at smaller domain sizes (5.0 vs. 24 nm) than for the LBH product, it is unlikely that surface energies, which should be larger per mole of the KBH product, play an important role in this case.

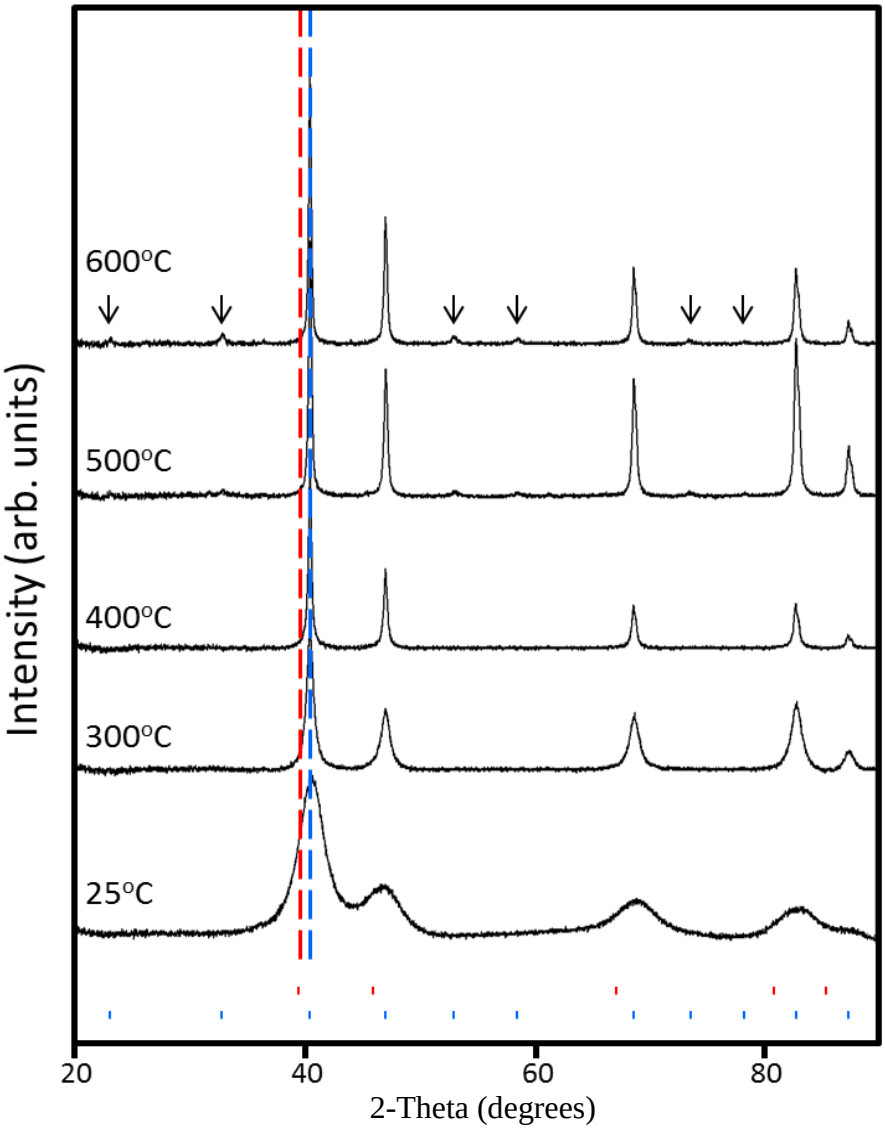

Figure 2.11 XRD pattern of Pt_3Co nanoparticles at room temperature and after annealing at 300°C, 400°C, 500°C, and 600°C for 24 hours. The red tick marks at the bottom denote the peak position of Pt (database card # 04-004-6364), and the blue lines denote the peak position of ordered Pt_3Co (database card # 04-006-7902). Reference lines for the (111) peak of Pt (red dotted line) and (111) peak of ordered Pt_3Co (blue dotted line) is shown for comparison. The ordering peaks are marked by (↓). Pt_3Co nanoparticles made with $LiB(Et)_3H$.

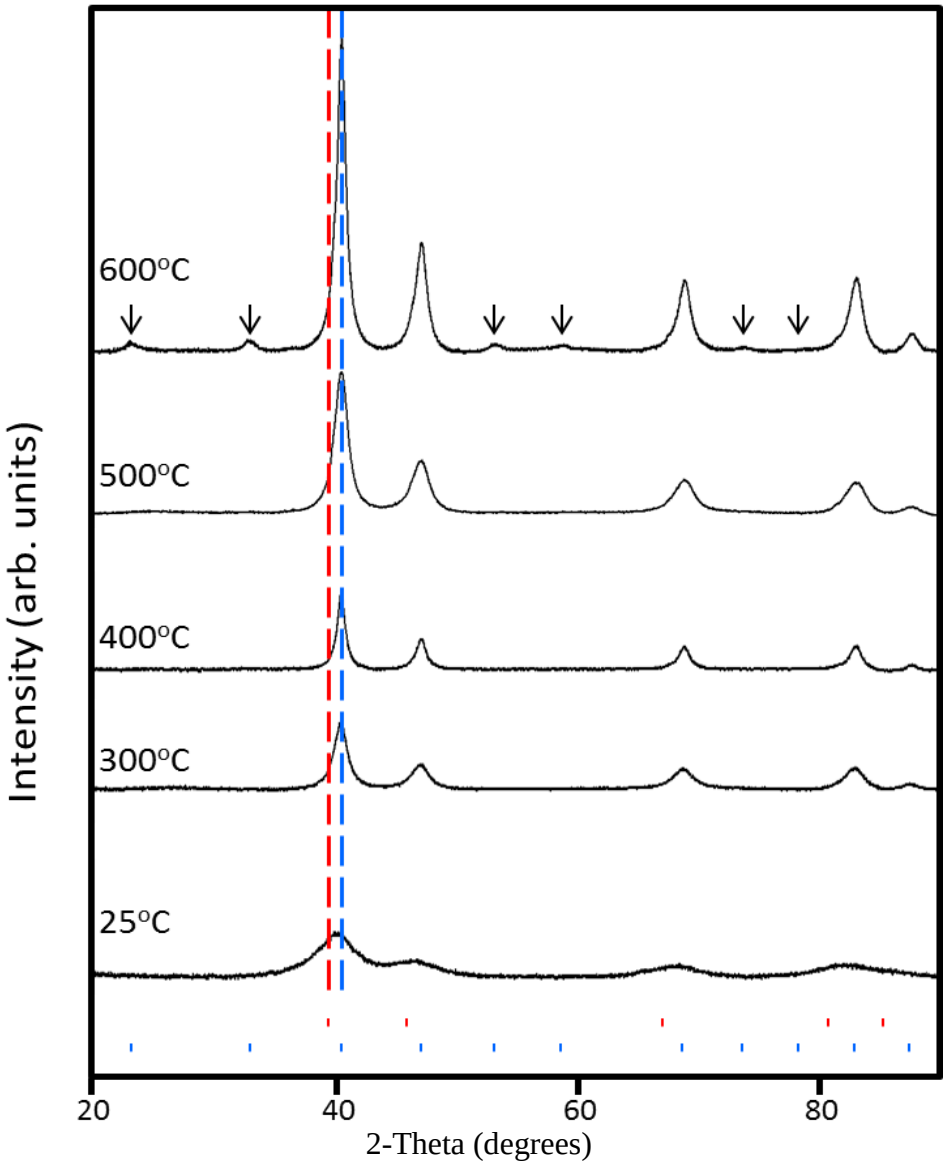

Figure 2.12 XRD pattern of Pt_3Co nanoparticles at room temperature and after annealing at 300°C, 400°C, 500°C, and 600°C for 24 hours. The red tick marks at the bottom denote the peak position of Pt (database card # 04-004-6364), and the blue tick marks denote the peak position of ordered Pt_3Co (database card # 04-006-7902). Reference lines for the (111) peak of Pt (red dotted line) and (111) peak of ordered Pt_3Co (blue dotted line) is shown for comparison. The ordering peaks are marked by (↓). Pt_3Co nanoparticles made with $KB(Et)_3H$. All samples were washed with Millipore water and dried to remove KCl prior to obtaining XRD pattern.

2.4.2 Lower Ordering Temperature by Changing Reduction Temperatures

Changing the reaction temperature (the temperature of solution during the reducing step) can significantly change the size of as synthesized nanoparticles. The domain size of Pt nanoparticles, made by dissolving Li_2PtCl_6, in 25 mL of THF at various temperatures (-35, 25, and 55^oC) and reduced with a corresponding amount of $LiB(Et)_3H$ (10% excess), were characterized by XRD and are depicted in Figure 2.13. The domain size of the sample increases when reduction occurs at elevated reaction temperatures (2.1, 3.3, 4.5 nm for reduction at -35, 25, and 55^oC respectively). It should be noted that in all samples, the precursor solution changes from clear orange to opaque black upon injection of the reducing agent, however, in the sample reduced at -35^oC, the color change happened relatively slowly, over the course of 3-5 seconds (color change was instant, less than a second, when reduction occurred at or above room temperature). The slow color change suggests a slower reduction rate; slower reduction kinetics has been shown to lead to more Pt nanoparticle "seeds" in solution,[49] which would lead to more particles with smaller average particle size.

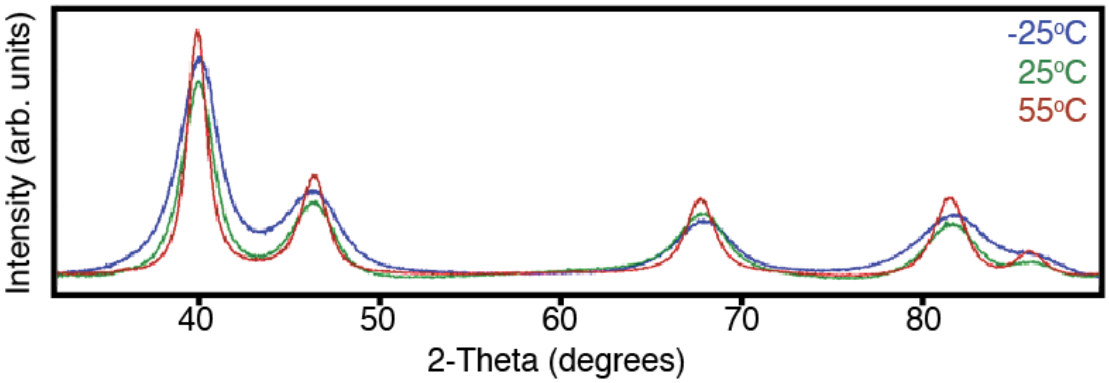

Figure 2.13 XRD pattern of Pt nanoparticles reduced at -25°C (blue curve), 25°C (green curve), and 55°C (red curve). From the FWHM, the domain size increases with increased reduction temperature.

Figure 2.14 Co-Pt phase diagram

Fig. 2.14 shows the experimental phase diagram of bulk Co-Pt. Pt_3Co (written

as $CoPt_3$ in the phase diagram) is single phase between 72 and 80 atomic percent Pt at 600^{o}C and is used as a test system to see if larger as-synthesized particles will order at lower annealing temperatures. Two samples of Pt_3Co nanoparticles were synthesized, one reduced at room temperature and the other reduced at 55^{o}C. Each sample was annealed at various temperatures for 24 hrs and XRD was used to monitor domain size and phase (either alloy or ordered intermetallic). The XRD patterns of Pt_3Co nanoparticles, reduced at 55^{o}C with 10% excess $KB(Et)_3H$, and annealed at 25, 300, 400, 500^{o}C for 24 hrs (all samples were washed with Millipore water and dried at 125^{o}C for 1 hour to remove KCl prior to XRD characterization) is shown in Fig. 2.15.

Reduction at 55^{o}C did lead to significantly lower ordering temperatures, however, the domain size of the sample increased faster than when reduced at room temperature (going from a domain size of 5.6 nm to 15.8 nm between annealing temperatures of 300^{o}C and 500^{o}C respectively vs. domain sizes of 3.3 nm to 5.2 nm for the sample reduced at room temperature and annealed under the same conditions) as seen in table 2.5. A possible explanation for this observation could be the slight increase in solubility of KCl in THF at 55^{o}C vs. 25^{o}C. The increased solubility could lead to slower KCl crystallization around the NPs and thus particles are closer together within the KCl lattice. We did not further pursue these observations, but it is clear that increasing the reduction temperature by 30^{o}C has an effect on nucleating behavior. For the purpose of consistency, all other reactions to produce nanoparticles in this thesis were carried out at room temperature.

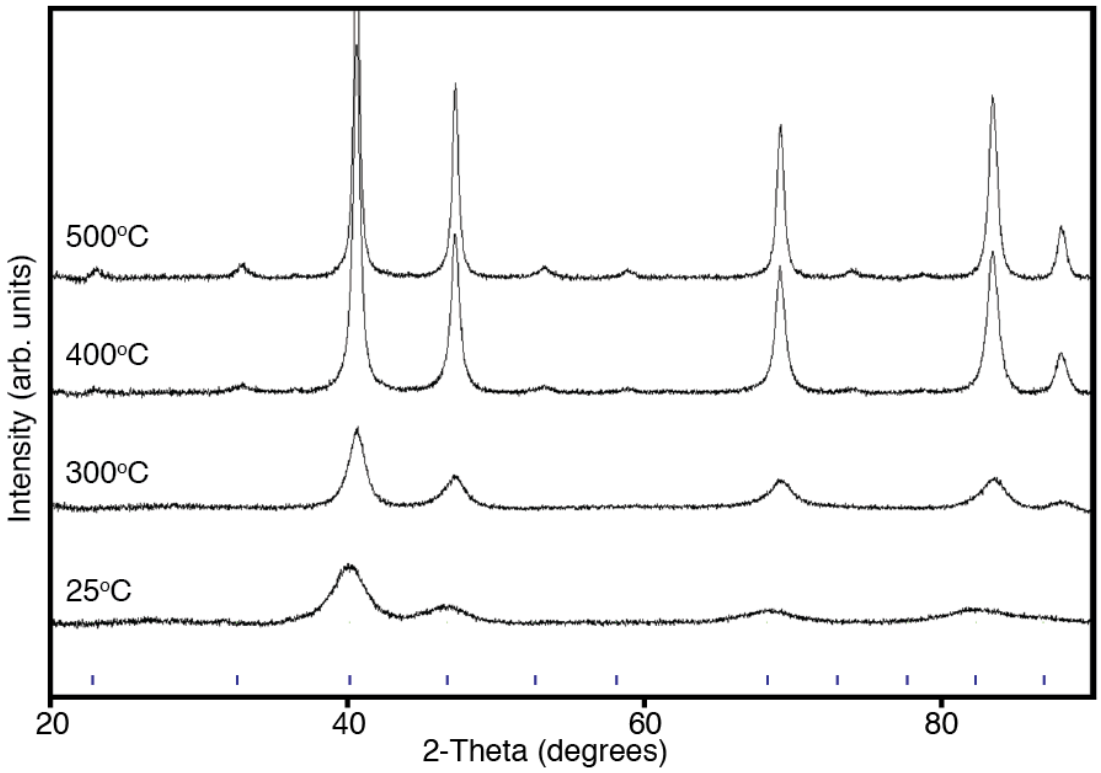

Figure 2.15 XRD pattern of **Pt_3Co reduced at 55°C with $KB(Et)_3H$** and annealed at 300, 400, and 500°C for 24 hours. The pattern at 25°C is the as-synthesized sample. The blue lines indicate the powder pattern of Pt_3Co (database card # 04-006-7902). For better resolution, each sample was washed with Millipore water and dried prior to data collection to remove KCl.

Table 2.5 Comparison of domain sizes and degree of ordering of Pt_3Co nanoparticles reduced at 25 and 55^{o}C and annealed at various temperatures for 24 hours. Degree of ordering was calculated from the XRD patters by dividing the intensity of the (1,1,0) peak at 32.84 2-theta with the (1,1,1) peak at 40.51 2-theta and dividing that number by 0.122 (the ratio of the peak intensities in fully ordered bulk Pt_3Co from the database card # 04-006-7902)

Annealing Temperature (^{o}C) for 24hr	Domain Size (nm)		Degree of Ordering (%)	
	25^{o}C reduction	55^{o}C reduction	25^{o}C reduction	55^{o}C reduction
25	1.7	2.0	--	--
300	3.3	5.6	--	--
400	4.5	10.9	--	32
500	4.8	15.8	--	55
600	5.0	--	20	--

2.4.3 Transfer of Nanomaterials to Carbon Support

For applications in catalysis, maintaining the high surface area of the nanomaterials is paramount. Using the method of ordered intermetallic nanoparticle synthesis and transfer described previously, the particles can be well dispersed onto a support material. An alternative method of obtaining ordered nanoparticles on a support material is to synthesize the particles directly onto the support (by reducing the metal precursors in a solution of C-Blk/THF), and then performing the proper heat treatment to obtain the ordered intermetallic phase. TEM of $Pt_{0.75}Co_{0.25}$/C synthesized by reducing the metal precursors in a solution containing C-Blk support is shown in Fig. 2.16a. The particles appear well dispersed on the support material. The sample is then annealed to 600^{o}C for 24 hrs to obtain the ordered phase and the TEM image is shown in Figure 2.16b; after annealing, some of the nanoparticles have agglomerated, lowering the active surface area. Fig. 2.16c is a TEM image of Pt_3Co annealed at 600^{o}C for 24 hrs, then transferred to C-Blk support using the method previously described in section 2.3.2. Transferring the particles after the heat treatment step minimizes agglomeration on the carbon support.

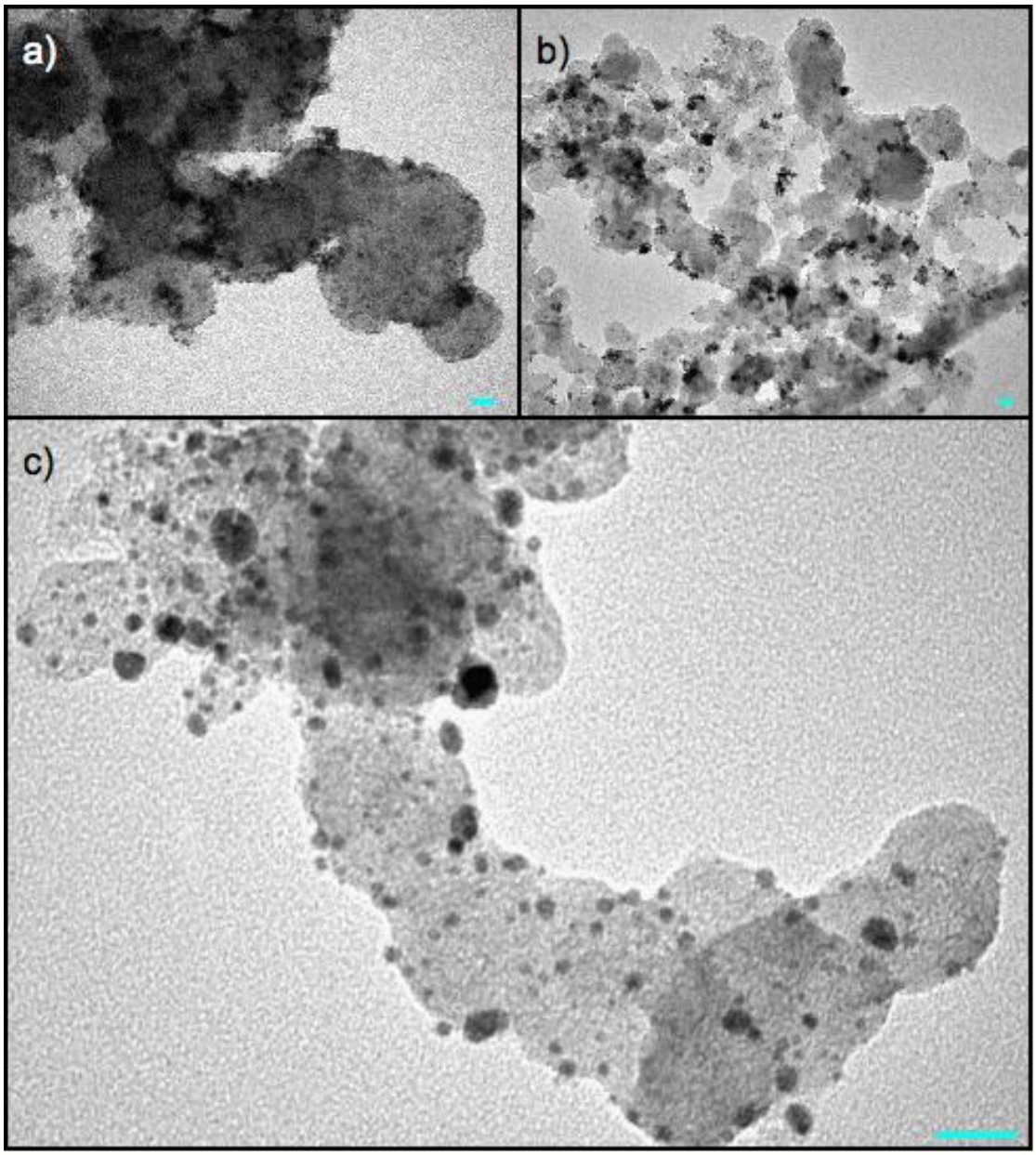

Figure 2.16. TEM image of Pt_3Co nanoparticles on C-Blk support. a) Unannealed Pt_3Co/C made by reducing metal precursors in a solution of dispersed C-Blk/THF, domain sizes of 1.6 nm. b) Pt_3Co/C after heat treatment at 600^{o}C for 24 hours, domain sizes of 4.2 nm c) Pt_3Co nanoparticles annealed at 600^{o}C for 24 hours, then transfer onto C-Blk support vie indirect method described in section 2.3.2, domain sizes of 5.0 nm. All scale bars denote 20 nm.

2.4.4 Synthesis of Other Binary and Pseudo-Ternary Systems

Using the solution phase coreduction method, other binary metal systems have been explored and synthesized. A list of the binary systems, the precursors used, the dissolution time, as well as the reducing agent employed is given in table 2.6. Table 2.7 lists the annealing conditions (temperature and annealing time) needed to transition from alloy to ordered intermetallic as well as the atomic composition (obtained by EDX) and domain size (calculated from XRD). The XRD patterns of the ordered intermetallic binary phases are given in Fig. 2.17 to 2.29.

Most of the XRD patterns are straight forward in that the peaks match up with the corresponding database peaks of the bulk ordered phase. Pt_3Cr (Fig. 2.18) was annealed at 750^{o}C for 24 hours, which would typically yield domain sizes greater than 25 nm (as observed in Fig. 2.21 with the Pt_2W sample), instead of the observed 13 nm. The minimal particle growth at relatively high temperatures (temperatures approaching the melting point of KCl) is do to an additional step mid heat treatment; Pt_3Cr/KCl sample was annealed at 400^{o}C for 12 hours, then transferred to carbon support and then annealed at 750^{o}C for 24 hours. Nanoparticle transfer was done after the initial heat treatment step so that the particles can grow to sizes greater than 3 nm, this is due to the high reactivity of as-synthesized nanoparticle (as-synthesized particles are typically < 2 nm and Cr will completely oxidize if exposed to air). PtZn sample, Fig. 2.26, was washed with 10 mL of 0.1M HCl to remove ZnO; EDX data in table 2.7 is the atomic ratio after the dilute acid wash. $PdBi_2$, Fig. 2.29, shows two ordered phases: ordered intermetallic $PdBi_2$ tetragonal and monoclinic. The bulk phase diagram of Bi-Pd, Fig. 2.30, shows that at low temperatures (< 380^{o}C) the monoclinic

is the stable phase while at higher temperatures (between 380-485^{o}C), the tetragonal phase is the stable phase. Annealing the $PdBi_2$ samples at higher or lower temperatures does show to favor one phase over the other (observable by an increase or decrease of the relative peak intensities of one phase over the other), however a pure phase sample was not obtainable without compromising particle size.

Table 2.6 Synthesis of binary nanoparticles with details on the precursors used, time it takes to dissolve completely in 25 mL THF

Target Binary Phase	Precursors	Time to Dissolve in 25 mL THF
Pt_3V	$PtCl_4$ (0.3 mmol), $VCl_4(THF)_2$ (0.1 mmol), LiCl (0.6 mmol)	< 30 min
Pt_3Cr	$PtCl_4$ (0.3 mmol), $CrCl_3(THF)_3$ (0.1 mmol), LiCl (0.6 mmol)	< 15 min
Pt_3Mn	$PtCl_4$ (0.3 mmol), $MnCl_2$ (0.1 mmol), LiCl (0.7 mmol)	8 hrs
Pt_3Co	$PtCl_4$ (0.3 mmol), Li_2CoCl_4 (0.1 mmol), LiCl (0.6 mmol)	< 15 min
Pt_2Mo	$PtCl_4$ (0.3 mmol), $MoCl_5$ (0.15 mmol), LiCl (0.6 mmol)	< 15 min
Pt_2W	$PtCl_4$ (0.3 mmol), WCl_6 (0.15 mmol), LiCl (0.6 mmol)	< 15 min
PtMn	$PtCl_4$ (0.3 mmol), $MnCl_2$ (0.3 mmol), LiCl (1.2 mmol)	8 hrs
PtFe	$PtCl_4$ (0.3 mmol), $FeCl_3$ (0.3 mmol), LiCl (0.6 mmol)	< 15 min
PtCo	$PtCl_4$ (0.3 mmol), Li_2CoCl_4 (0.3 mmol), LiCl (0.6 mmol)	< 15 min
PtNi	$PtCl_4$ (0.3 mmol), Li_6NiCl_8 (0.3 mmol), LiCl (0.6 mmol)	2 hrs
PtZn	$PtCl_4$ (0.3 mmol), $ZnCl_2$ (0.3 mmol), LiCl (0.6 mmol)	< 15 min
Pd_3Fe	$PdCl_2$ (0.3 mmol), $FeCl_3$ (0.1 mmol), LiCl (0.6 mmol)	< 30 min
Pd_3Sn	$PdCl_2$ (0.3 mmol), $SnCl_2$ (0.1 mmol), LiCl (0.7 mmol)	< 30 min
$PdBi_2$	$PdCl_2$ (0.3 mmol), $BiCl_3$ (0.6 mmol), LiCl (2.4 mmol)	< 30 min

Table 2.7 Summary of annealing conditions to form the ordered intermetallic phase of various binary systems. The ordered structure, atomic ratios (from EDX) and domain size (from XRD) are also provided.

Target Binary Phase	Reducing Agent Used	Anneal Temp. (^{o}C)	Anneal Time (hr)	Ordered Structure	EDX ratio	Domain Size (nm)
Pt_3V	KNaph	625	24	Cubic	78:22	15
Pt_3Cr	KNaph	750	24	Cubic	65:35	13
Pt_3Mn	KNaph	385	6	Cubic	77:23	10
Pt_3Co	$KB(Et)_3H$	600	24	Cubic	76:24	5
Pt_2Mo	$KB(Et)_3H$	650	24	Orthorhombic	68:32	13
Pt_2W	KNaph	750	24	Orthorhombic	67:33	30
PtMn	$KB(Et)_3H$	600	24	Tetragonal	52:48	8
PtFe	$KB(Et)_3H$	600	12	Tetragonal	51:49	6
PtCo	$KB(Et)_3H$	575	18	Tetragonal	53:47	5
PtNi	$KB(Et)_3H$	575	24	Tetragonal	52:48	7
PtZn	KNaph	500	12	Tetragonal	60:40	11
Pd_3Fe	$KB(Et)_3H$	600	24	Cubic	76:24	9
Pd_3Sn	$KB(Et)_3H$	600	24	Cubic	74:26	9
$PdBi_2$	$KB(Et)_3H$	385	24	Tetragonal/ Monoclinic	32:68	25 27

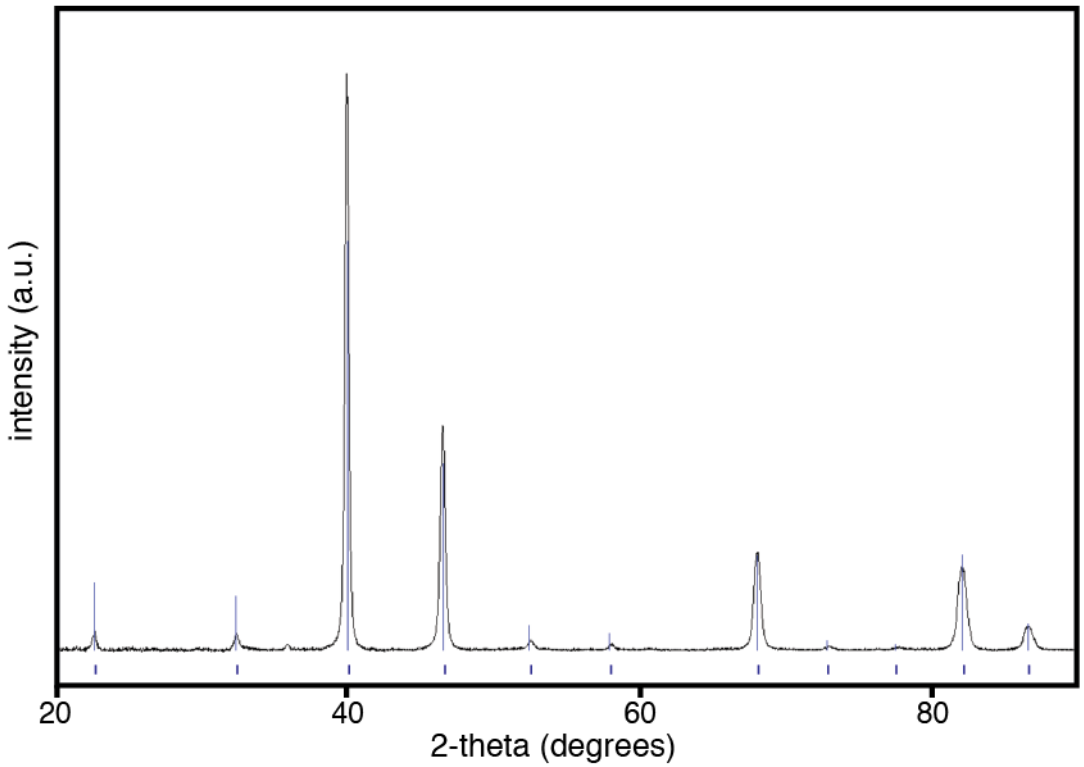

Figure 2.17 XRD pattern of Pt_3V from the synthesis and annealing conditions described in table 2.6 and 2.7. The blue tick marks at the bottom denote the peak position of ordered Pt_3V (database card # 04-004-6343), with the blue lines showing the relative peak intensities. This sample was washed with Millipore water and dried at 125^{o}C for 1 hour prior to obtaining the XRD pattern to remove any residual KCl.

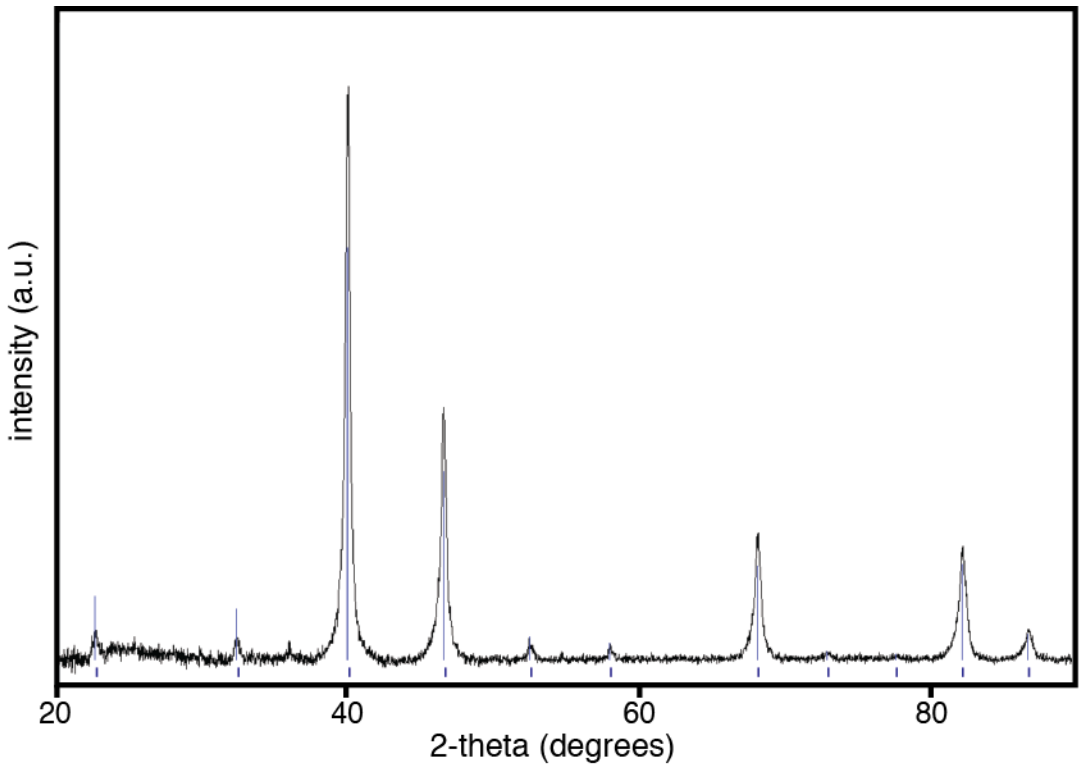

Figure 2.18 XRD pattern of Pt_3Cr from the synthesis and annealing conditions described in table 2.6 and 2.7. The blue tick marks at the bottom denote the peak position of ordered Pt_3Cr (database card # 04-003-3551), with the blue lines showing the relative peak intensities. This sample was washed with Millipore water and dried at 125^{o}C for 1 hour prior to obtaining the XRD pattern to remove any residual KCl.

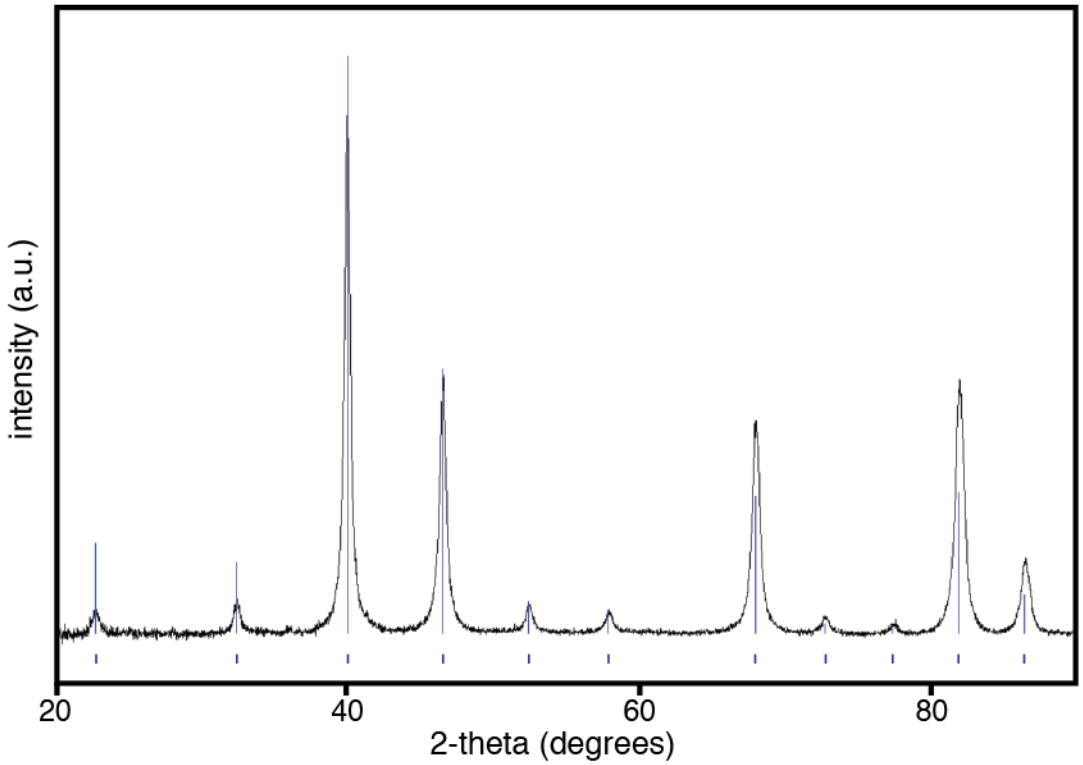

Figure 2.19 XRD pattern of Pt_3Mn from the synthesis and annealing conditions described in table 2.6 and 2.7. The blue tick marks at the bottom denote the peak position of ordered Pt_3Mn (database card # 03-065-3260), with the blue lines showing the relative peak intensities. This sample was washed with Millipore water and dried at 125^{o}C for 1 hour prior to obtaining the XRD pattern to remove any residual KCl.

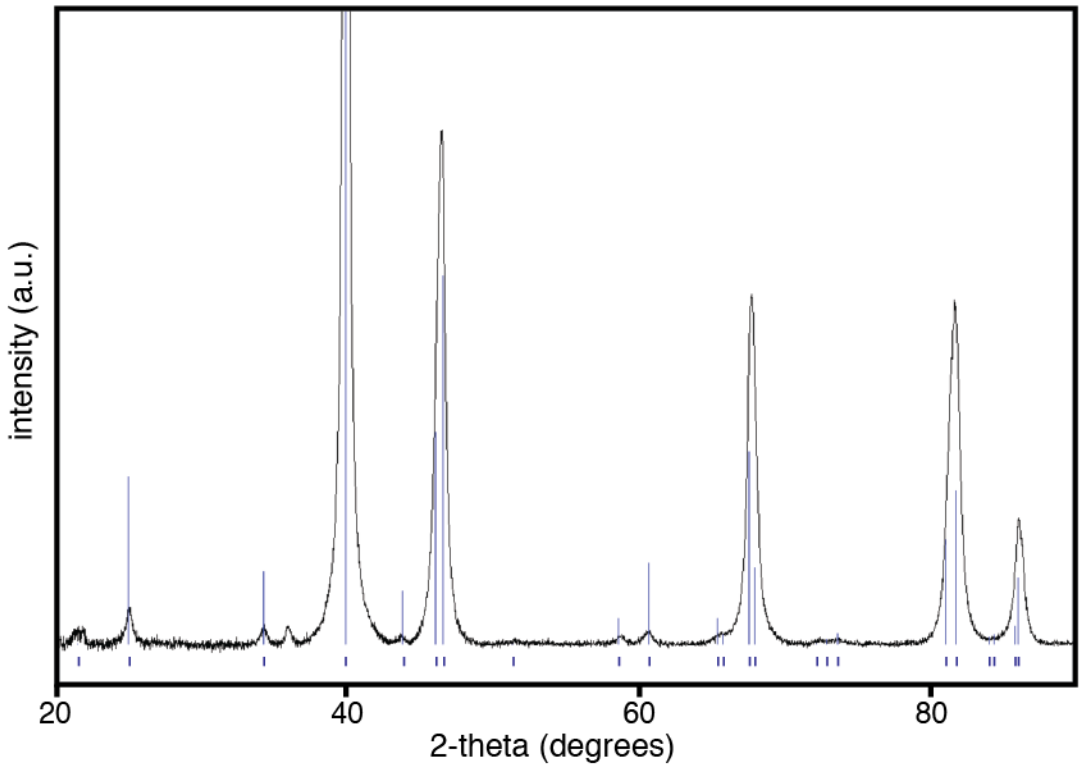

Figure 2.20 XRD pattern of Pt_2Mo from the synthesis and annealing conditions described in table 2.6 and 2.7. The blue tick marks at the bottom denote the peak position of ordered Pt_2Mo (database card # 04-001-0706), with the blue lines showing the relative peak intensities. This sample was washed with Millipore water and dried at 125^{o}C for 1 hour prior to obtaining the XRD pattern to remove any residual KCl.

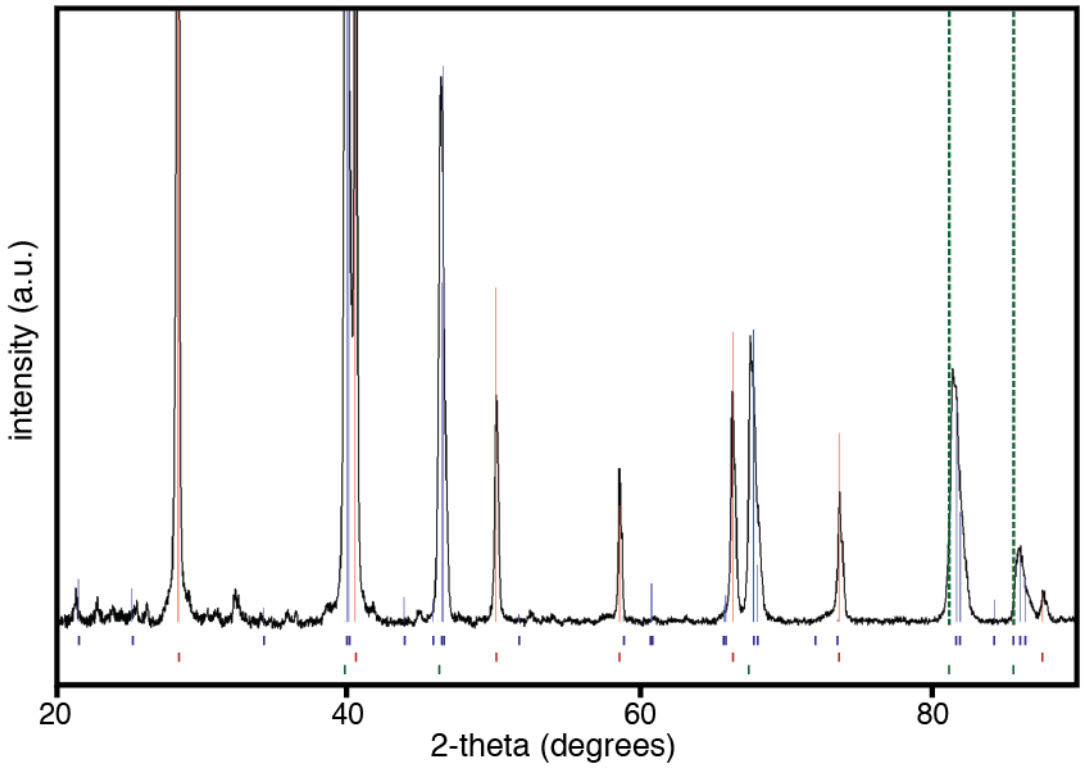

Figure 2.21 XRD pattern of Pt_2W from the synthesis and annealing conditions described in table 2.6 and 2.7. The blue, red, and green tick marks at the bottom denote the peak positions of ordered Pt_2W (database card # 04-004-2345), KCl (database card # 00-004-0587), and Pt (database card # 04-004-6364) respectively. The blue and red lines show the relative peak intensities of Pt_2W and KCl respectively. The green dotted lines highlight the peak positions of Pt at higher angles.

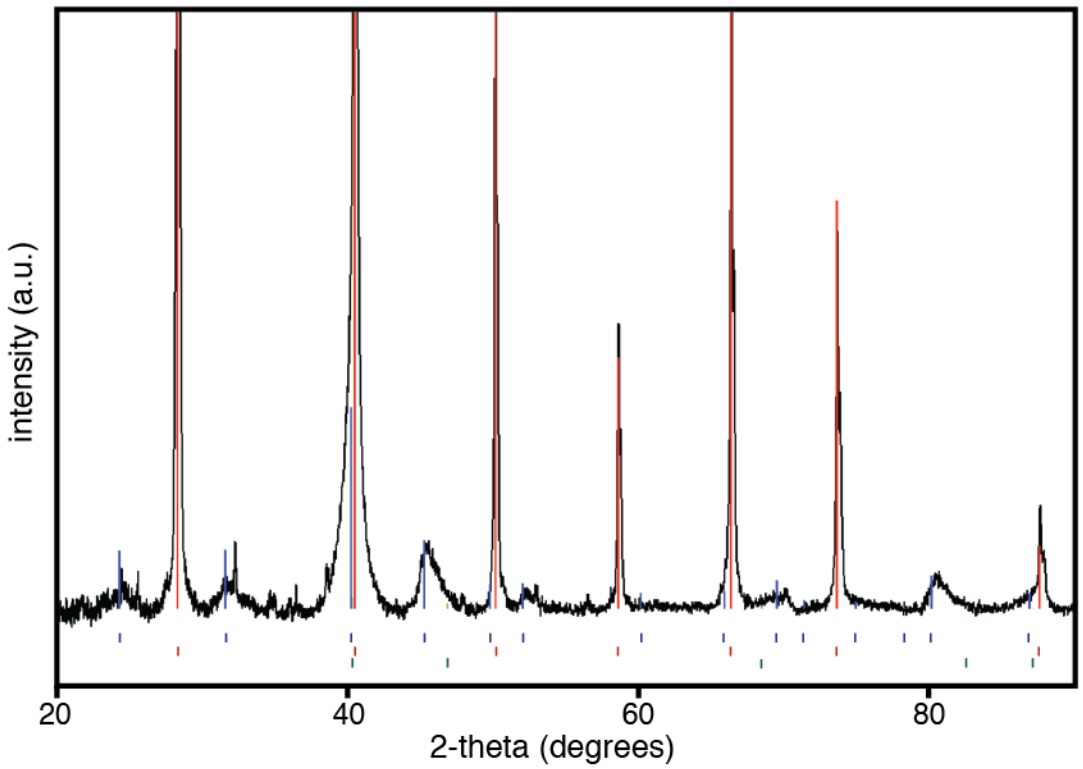

Figure 2.22 XRD pattern of PtMn from the synthesis and annealing conditions described in table 2.6 and 2.7. The blue tick marks at the bottom denote the peak position of ordered PtMn (database card # 01-077-2941), with the blue lines showing the relative peak intensities. The red tick marks are the peak positions of KCl (database card # 00-004-0587) with the red lines showing the relative intensities. The green tick marks denote $Pt_{0.5}Mn_{0.5}$ alloy (database card # 04-001-0116)

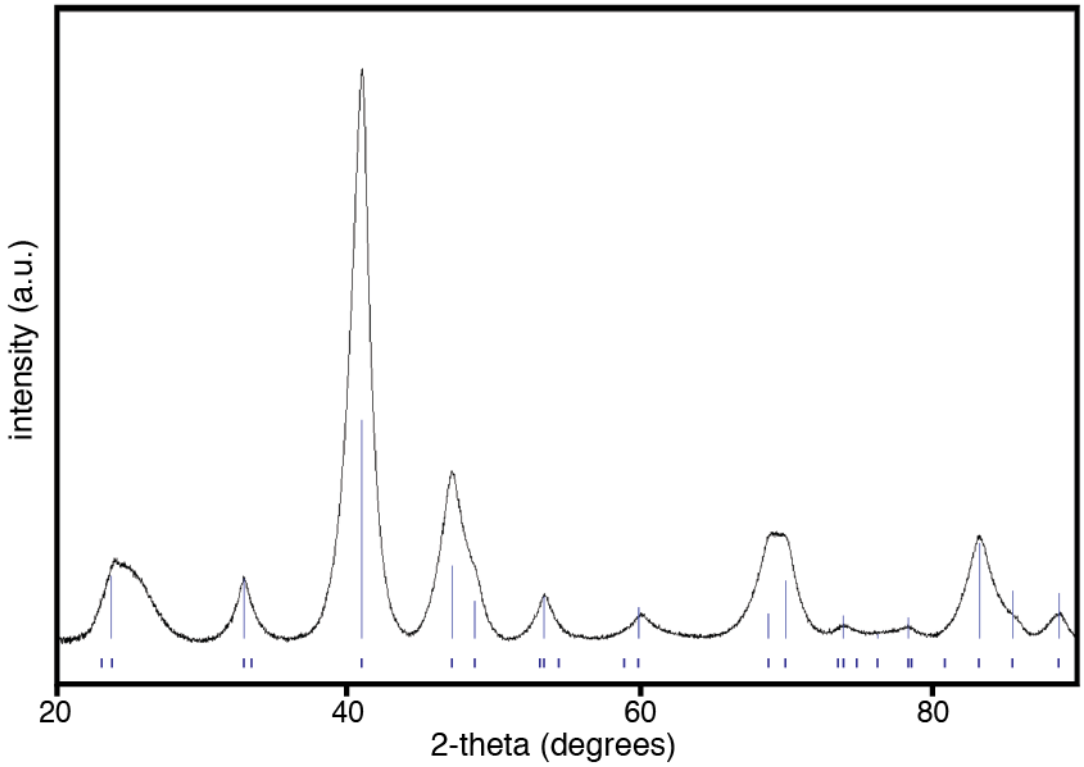

Figure 2.23 XRD pattern of PtFe from the synthesis and annealing conditions described in table 2.6 and 2.7. The blue tick marks at the bottom denote the peak position of ordered PtFe (database card # 00-043-1359), with the blue lines showing the relative peak intensities. This sample was transferred to C-Blk support, washed with Millipore water and dried at 125^{o}C for 1 hour prior to obtaining the XRD pattern to remove any residual KCl. The broad peak around 25^{o} is from the carbon support material.

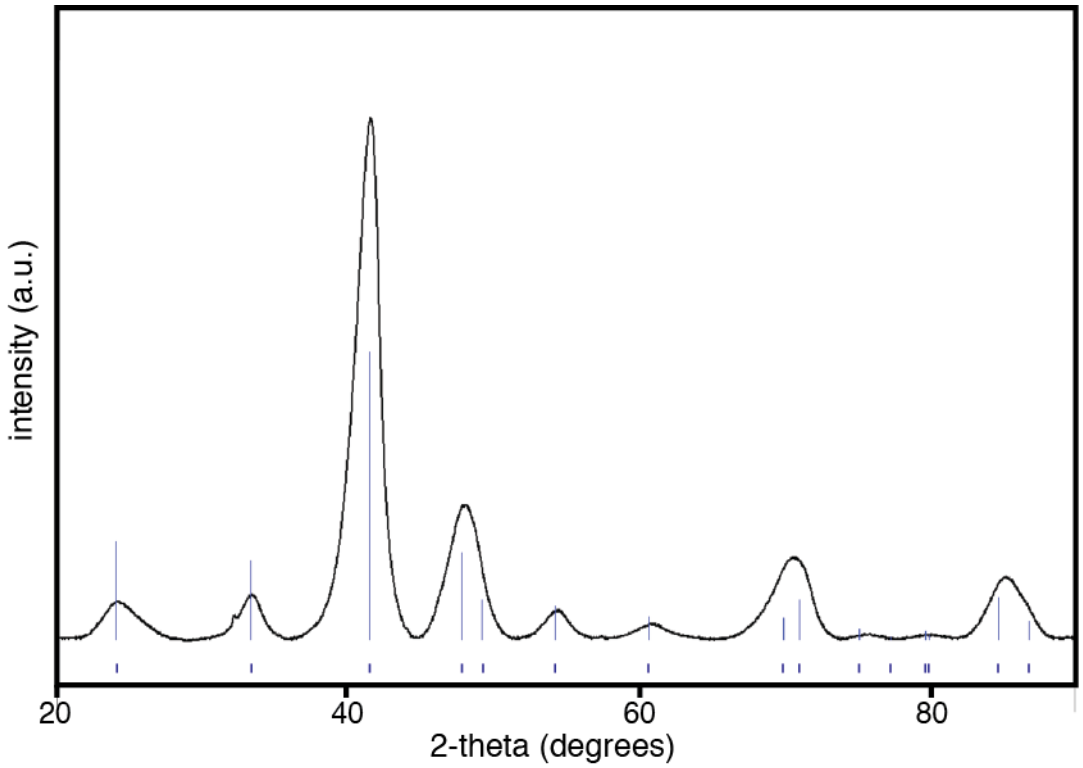

Figure 2.24 XRD pattern of PtCo from the synthesis and annealing conditions described in table 2.6 and 2.7. The blue tick marks at the bottom denote the peak position of ordered PtCo (database card # 03-065-8969), with the blue lines showing the relative peak intensities. This sample was transferred to C-Blk support, washed with Millipore water and dried at 125^{o}C for 1 hour prior to obtaining the XRD pattern to remove any residual KCl. The broad peak around 25^{o} is from the carbon support material.

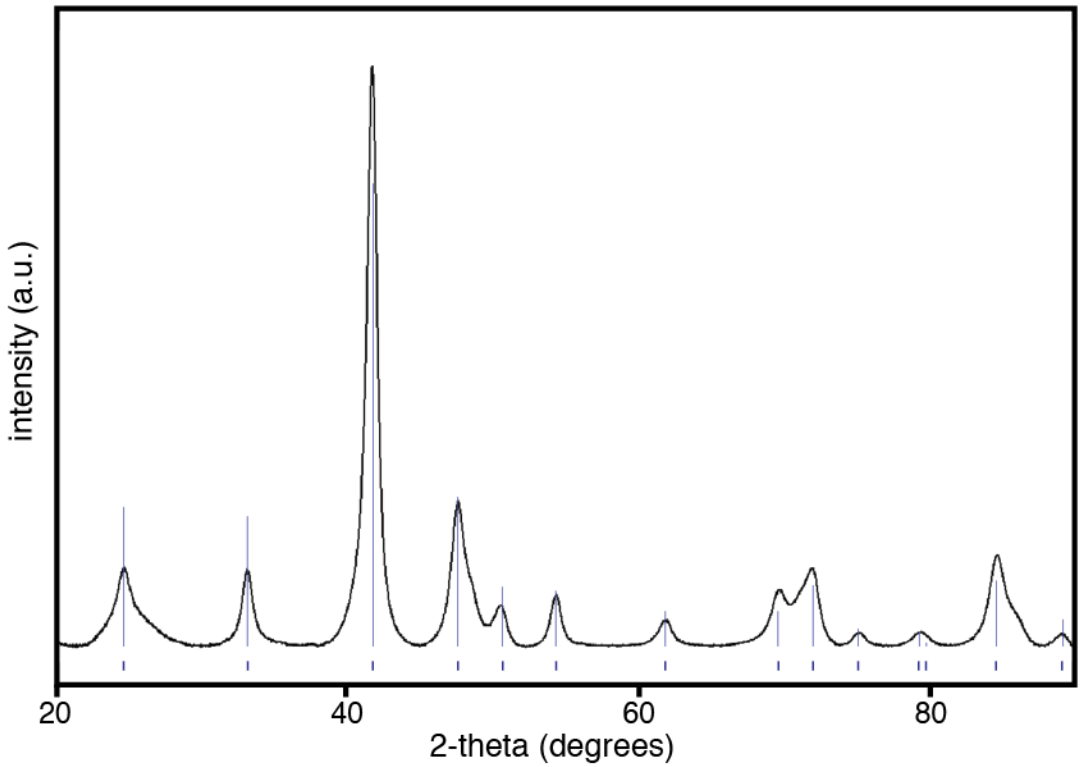

Figure 2.25 XRD pattern of PtNi from the synthesis and annealing conditions described in table 2.6 and 2.7. The blue tick marks at the bottom denote the peak position of ordered PtNi (database card # 01-072-2524), with the blue lines showing the relative peak intensities. This sample was transferred to C-Blk support, washed with Millipore water and dried at 125^{o}C for 1 hour prior to obtaining the XRD pattern to remove any residual KCl. The broad peak around 25^{o} is from the carbon support material.

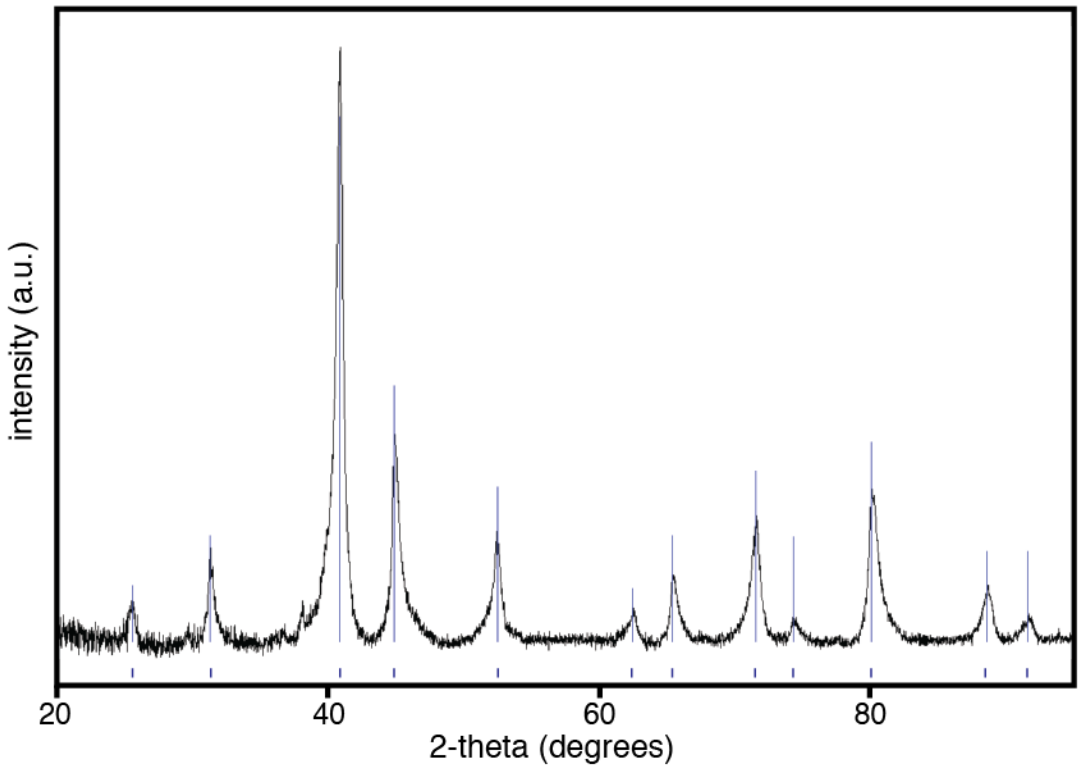

Figure 2.26 XRD pattern of PtZn from the synthesis and annealing conditions described in table 2.6 and 2.7. The blue tick marks at the bottom denote the peak position of ordered PtZn (database card # 00-006-0604), with the blue lines showing the relative peak intensities. This sample was washed with 0.1M HCl solution (10 mL) and Millipore water, then dried at 125^{o}C for 1 hour prior to obtaining the XRD pattern to remove any residual KCl and ZnO.

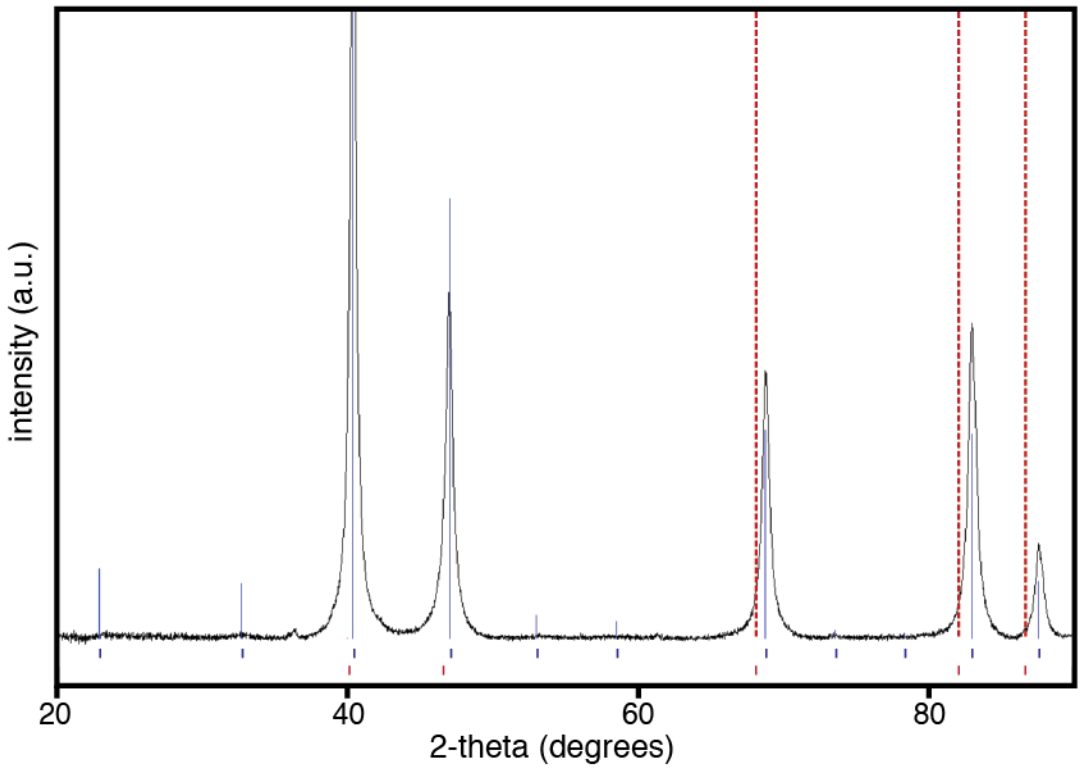

Figure 2.27 XRD pattern of Pd_3Fe from the synthesis and annealing conditions described in table 2.6 and 2.7. The blue and red tick marks at the bottom denote the peak position of ordered Pd_3Fe (database card # 01-071-8348) and Pd (database card # 00-046-1043), with the blue lines showing the relative peak intensities. The red dotted line shows the higher angle peak positions of Pd. This sample was washed with Millipore water and dried at 125^{o}C for 1 hour prior to obtaining the XRD pattern to remove any residual KCl.

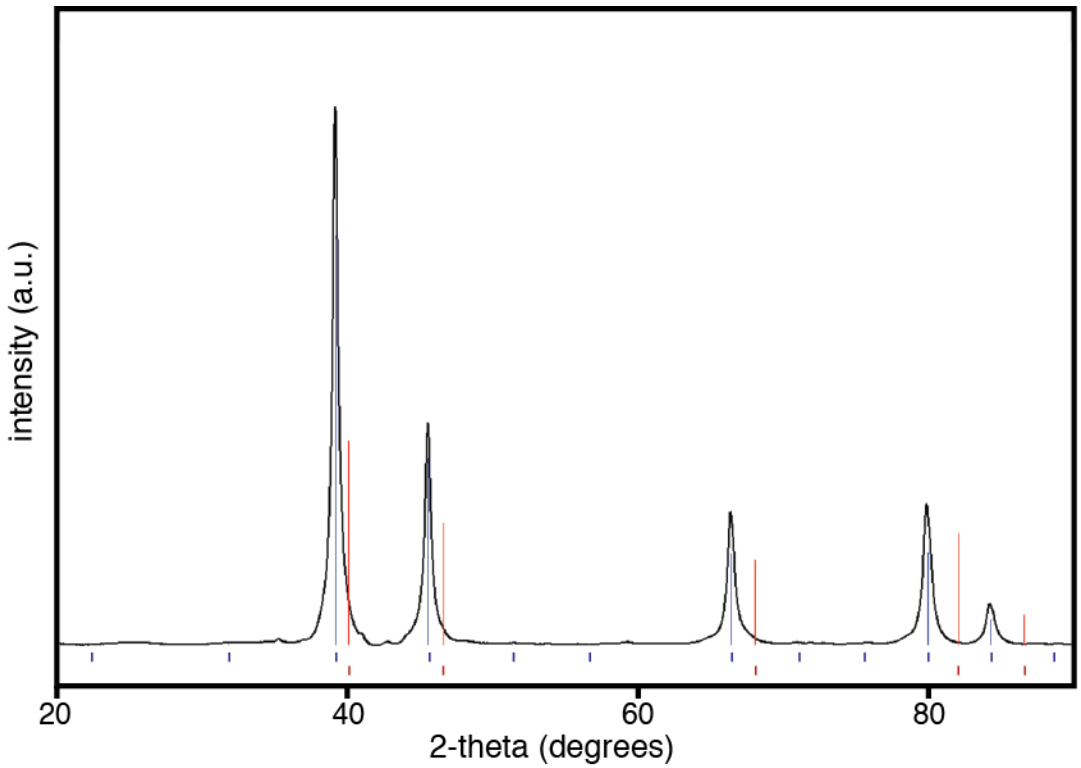

Figure 2.28 XRD pattern of Pd_3Sn from the synthesis and annealing conditions described in table 2.6 and 2.7. The blue and red tick marks at the bottom denote the peak position of ordered Pd_3Sn (database card # 04-001-0351) and Pd (database card # 00-046-1043), with the blue lines showing the relative peak intensities. The red dotted line shows the higher angle peak positions of Pd. This sample was washed with Millipore water and dried at 125^{o}C for 1 hour prior to obtaining the XRD pattern to remove any residual KCl.

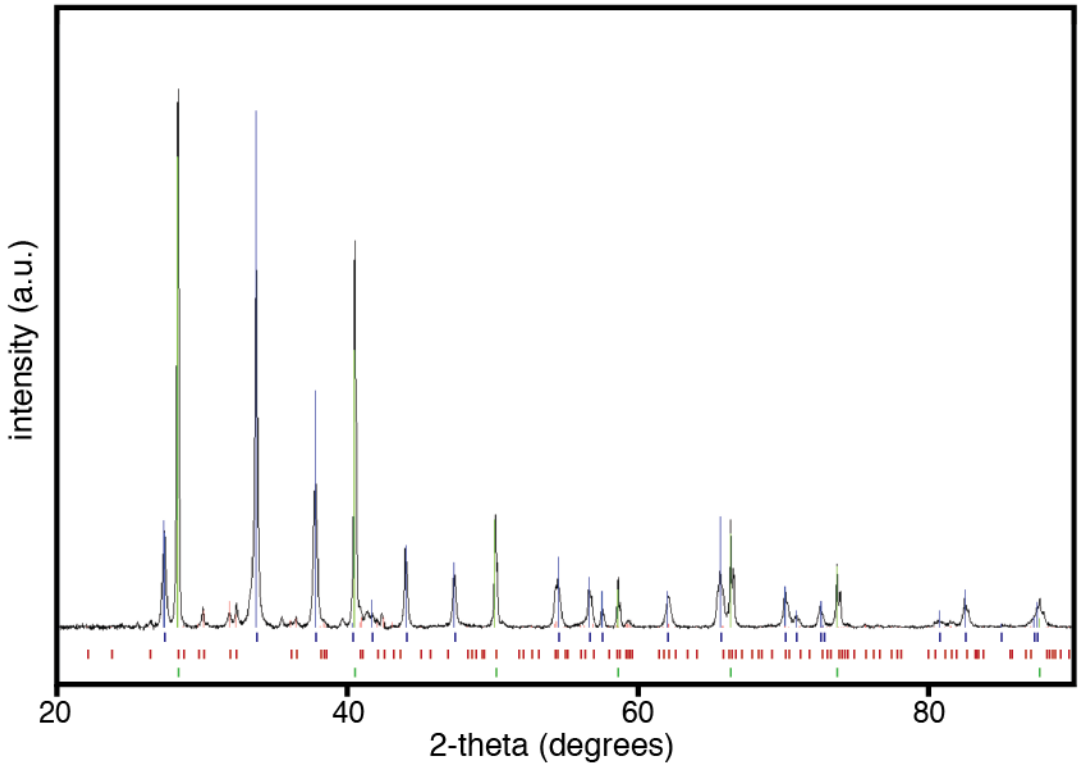

Figure 2.29 XRD pattern of $PdBi_2$ from the synthesis and annealing conditions described in table 2.6 and 2.7. The blue, red, and green tick marks at the bottom denote the peak position of ordered tetragonal $PdBi_2$ (database card # 04-003-6165), ordered monoclinic $PdBi_2$ (database card # 04-007-1933), and KCl (database card # 00-004-0587) respectively. The blue, red, and green lines show the relative peak intensities of each of the three phases.

Figure 2.30 Bi-Pd phase diagram

To explore the applicability of this method to synthesizing ordered intermetallic nanoparticles to systems beyond binary, the pseudo binary Pt_2FeNi, Pt_2CoNi, Pt_2CoFe, and PtFeSn phases were explored. Table 2.8 summarizes the synthetic and ordering (annealing) conditions of the pseudo ternary phases. The XRD patterns of ordered intermetallic Pt_2FeNi, Pt_2CoNi, and Pt_2CoFe nanoparticles are depicted in Fig. 2.31 and the XRD pattern of PtFeSn is given in Fig. 2.32. Since these phases (excluding PtFeSn) share the same structure type (tetragonal), similar peaks are observed; the lattice parameters of Pt_2FeNi, Pt_2CoNi, and Pt_2CoFe (from the database card # 00-035-0702, 01-077-7530, and 01-077-7477 respectively) are given in table 2.9. The location of the peaks shift according to the size of the unit cell, however the peak shifts are subtle due to the close atomic sizes of the non-Pt metals. Nonetheless, it is clear (since the ordered ternary XRD pattern is much more complex than the disordered cubic XRD pattern of the as-synthesized materials) that this method is capable of synthesizing pseudo ternary materials using this modified solution phase coreduction method.

Table 2.8 Summary of annealing conditions to form the ordered intermetallic phase of various pseudo-ternary systems. The reducing agent used, the ordered structure type, atomic ratios (from EDX) and domain size (from XRD) are also provided.

Target Phase	Reducing Agent Used	Anneal Temp. (^{o}C)	Anneal Time (hr)	Ordered Structure	EDX ratio	Domain Size (nm)
Pt_2FeNi	$KB(Et)_3H$	550	12	Tetragonal	46:28:27	7
Pt_2CoNi	$KB(Et)_3H$	550	12	Tetragonal	55:26:19	6
Pt_2CoFe	$KB(Et)_3H$	550	12	Tetragonal	46:25:28	6
PtFeSn	$KB(Et)_3H$	350	24	Hexagonal	31:35:34	8

Table 2.9 Lattice parameters of Pt_2CoNi (database card # 01-077-7530), Pt_2CoFe (database card # 01-077-7477), and Pt_2FeNi (database card # 00-035-0702).

Ordered Phase:	Lattice Parameters		
	a	b	c
Pt_2CoNi	3.815	3.815	3.651
Pt_2CoFe	3.833	3.833	3.718
Pt_2FeNi	3.837	3.837	3.656

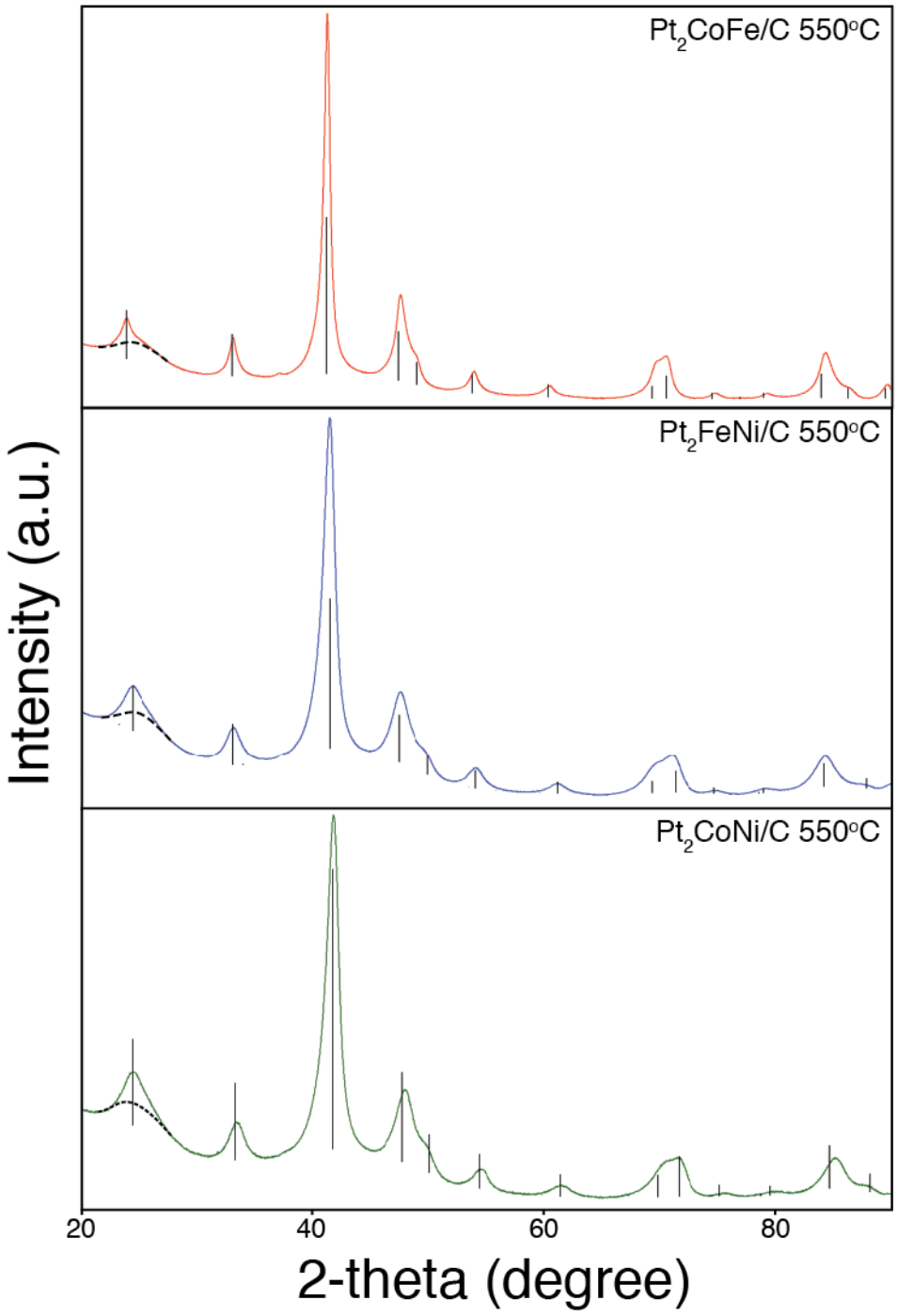

Figure 2.31 XRD pattern of Pt_2FeNi, Pt_2CoNi, and Pt_2CoFe (preparation details described in Table 2.8). The green lines mark the peak position of Pt_2FeNi (database card # 00-035-0702), the red lines mark the peak position of Pt_2CoNi (database card # 01-077-7530), and the blue lines mark the peak position of Pt_2CoFe (database card # 01-077-7477).

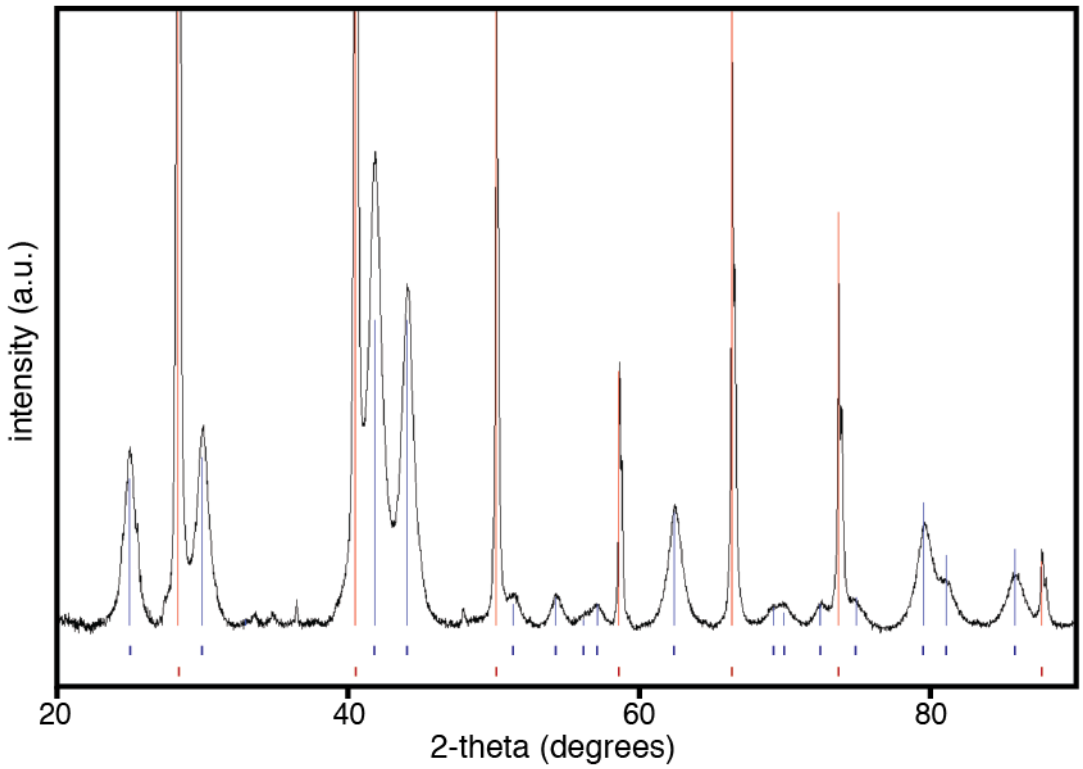

Figure 2.32 XRD pattern of PtFeSn from the synthesis and annealing conditions described in Table 2.8. The blue and red tick marks at the bottom denote the peak position of ordered PtFeSn (database card # 00-038-0922) and KCl (database card # 00-004-0587), with the blue and red lines showing the relative peak intensities.

2.5 Conclusion

The solution phase coreduction method offers a direct route to nanoparticle synthesis. The versatility and simplicity of this method makes it unique to the other variations of solution phase reduction methods; by selecting from a class of THF soluble precursors (metal chlorides, metal chloride THF adducts, or lithium metal chlorides), and using the right reducing agent (A[naphthalide] or A[$B(Et)_3H$] where A = Li of K), multimetallic alloy nanoparticles can be easily synthesized. Selecting potassium-based reducing agents traps the particles in a KCl matrix, kinetically stabilizing the particles and preventing agglomeration upon synthesis. The KCl also slows particle agglomeration when annealing to high temperatures (< 770^oC), giving the option to heat treat nanoparticle while maintaining relatively small particle sizes. The particles can be dispersed onto a support material after heat treatment using a weakly coordinating surfactant (ethylene glycol). Thus, this method is a versatile approach to synthesizing ordered nanoparticles for catalytic applications, which require high surface area materials.

The next chapter will focus on the catalytic activity (towards the oxygen reduction reaction or methanol oxidation reaction) of nanoparticles prepared in this manner.

REFERENCES

1 D. Wang, Q. Peng and Y. Li, *Nano Research* 2010, *3*, 574-580.

2 C. Raab, M. Simko, U. Fiedeler, M. Nentwich and A. Gazso, *Nano Trust Dossiers* 2011, *6*, 1-4.

3 Cahn, R. W. *Contemp. Phys.* 2001, *42*, 365-375.

4 J. Rodriguez-Carvajal, G. Rousse, C. Masquelier and M. Hervieu, *Physical review letters,* 1998, *81*, 4660-4663.

5 Liu, C. T. *Mater. Chem. Phys.* 1995, *42*, 77-86.

6 Sun, S.; Murray, C. B.; Weller, D.; Folks, L.; Moser, A. *Science* 2000, *287*, 1989-1992.

7 Goll, D.; Kronmuller, H. *Naturewissenschaften* 2000, *87*, 423-438.

8 Paduani, C. *J. Appl. Phys.* 2001, *90*, 6251.

9 Gavaler, J. R.; Janocko, M. A.; Bradinski, A. I.; Rowland, G. W. *IEEE Trans. Magn.* 1975, *2*, 192-196.

10 Cava, R. J.; Takagi, H.; Zandbergen, H. W.; Krajewski, J. J.; Peck, W. F.; Siegrist, T.; Batlogg, B.; Vandover, R. B.; Felder, R. J.; Mizuhashi, K.; Lee, J. O.; Eisaki, H.; Uchida, S. *Nature* 1994, *367*, 252.

11 He, T.; Huang, Q.; Ramirez, A. P.; Wang, Y.; Regan, K. A.; Rogado, N.; Hayward, M. A.; Haas, M. K.; Slusky, J. S.; Inumara, K.; Zandbergen, H. W.; Ong, N. P.; Cava, R. J. *Nature* 2001, *411*, 54-56.

12 Lopez, M. F.; Escudero, M. L. *Electrochim. Acta* 1998, *43*, 671-678.

13 Casado-Rivera, E.; Gal, Z.; Angelo, A. C. D.; Lind, C.; DiSalvo, F. J.; Abruna, H. D. *Chem. Phys. Chem.* 2003, *4*, 193-199.

14 Casado-Rivera, E.; Volpe, D. J.; Alden, L.; Lind, C.; Downie, C.; Vazquez-Alvarez, T.; Angelo, A. C. D.; DiSalvo, F. J.; Abruna, H. D. *J. Am. Chem. Soc.* 2004, *126*, 4043-4049.

15 Oana, M.; Hoffmann, R.; Abruna, H. D.; DiSalvo, F. J. *Surf. Sci.* 2005, *574*, 1-16.

16 Roucoux, A.; Schulz, J.; Patin, H. *Chem. Rev.* 2002, *102*, 3757-3778.

17 Zhang, C. J.; Baxter, R. J.; Hu, P.; Alavi, A.; Lee, M.-H. *J. Chem. Phys.* 2001, *115*, 5272-5277.

18 Mathauser, A. T.; Teplyakov, A. V. *Catal. Lett.* 2001, *73*, 207-210.

19 J. M. Gregoire, M. Kostylev, M. E. Tague, P. F. Mutolo, R. B. v. Dover, F. J. DiSalvo and H. D. Abruna, *Journal of the Electrochemical Society* 2009, *156*, B160-B166.

20 M. Prochaska, J. Jin, D. Rochefort, L. Zhuang, F. J. DiSalvo, H. D. Abruna and R. B. v. Dover, *Review of scientific instruments* 2006, *77*, 054104-054104.

21 P. Strasser, Q. Fan, M. Devenney, W. H. Weinberg, P. Liu and J. K. Norskov, *The Journal of Physical Chemistry B* 2003, *107*, 11013-11021.

22 Y. Kang, J. B. Pyo, X. Ye, T. R. Gordon and C. B. Murray, *ACS nano* 2012, *6*, 5642-5647.

23 J. Greeley, T. F. Jaramillo, J. Bonde, I. B. Chorkendorff and J. K. Norskov, *Nature materials* 2006, *5*, 909-913.

24 Shelton, Robin; Cliffe, J. Allie. “Spherical Cows” nasa.gov.

25 P. Claus, H. Hofmeister, *Journal of Physical Chemistry B* 1999, *103*, 2766.

26 A. Kraynov and T. E. Muller, *Applications of Ionic Liquids in Science and Technology* InTech 2011, p. 516.

27 J. D. Aiken III, R. G. Finke, *Journal of Molecular Catalysis A – Chemical* 1999, *145*, 1.

28 J. T. G. Overbeek, *Pure and Applied Chemistry* 1980, *52*, 1151.

29 L. S. Ott, R. G. Finke, *Coordination Chemistry Reviews* 2007, *251*, 1075.

30 S. K. M. Henze, O. Bauer, T. L. Lee, M. Sokolowski, F. S. Tautz, *Surface Science* 2007, *601*, 1566.

31 T. Hyeon, *Chemical Communications* 2003, *8*, 927-934.

32 B. Derjaguin, L. D. Landau, *Zhurnal Eksperimentalnoi I Teoreticheskoi Fiziki* 1945, *15*, 663.

33 E. J. Verwey, J. T. G. Overbeek, *Theory of the Stability of Lyophobic Colloids*, Elsevier, Amsterdam 1948.

34 B. Chaudret, K. Philippot, *Oil & Gas Science and Technology - Revue de l'IFP* 2007, *62*, 799.

35 E. V. Shevchenko, D. V. Talapin, H. Schnablegger, A. Kornowski, O. Festin, P. Svedlindh, M. Hasse and H. Weller, *Journal of American Chemical Society* 2003, 9090-9101.

36 J. Dupont, G. S. Fonseca, A. P. Umpierre, P. F. P. Fichtner, S. R. Teixeira, *Journal of the American Chemical Society* 2002, *124*, 4228.

37 B. M. Leonard, Q. Zhou, D. Wu and F. J. DiSalvo, *Chemistry of Materials* 2011, *23*, 1136-1146.

38 **a)** A. J. Bard and L. R. Faulkner, *Electrochemical Methods Fundamentals and Applications*, John Wiley & Sons, Inc., Canada, **1980**. **b)** "Chemical Reactivity." Cem.msu.edu. Retrieved 2013-04-06. **c)** U. Olsher, R. M. Izatt, J. S. Bradshaw and N. K. Dalley, *Chemical Reviews* **1991**, *91*, 137-164.

39 N. G. Connelly, W. E. Geiger, *Chemical Redox Agents for Organometallic Chemistry*, Chem. Rev. 1996, 96, 877-910.

40 *Standard Reduction Potentials, Vol.* Internet Archive: Way Back Machine, http://web.archive.org/web/20070518092613/http://www.northland.cc.mn.us/Chemistry/standard_reduction_potentials.htm.

41 M. Winter in *WebElements: the periodic table, Vol.* WebElements, http://www.webelements.com, 1993-2012.

42 G. N. Glavee, K. J. Klabunde, C. M. Sorensen and G. C. Hadjipanayis, *Langmuir* 1994, *10*, 4726-4730.

43 Krishnamurthy, S. *Aldrichim. Acta.* 1974, *7*, 55.

44 C. Morin, D. Simon and P. Sautet, *The Journal of Physical Chemistry B* 2004, *108*, 12084-12091.

45 T. Ghosh, F. Matsumoto, J. Mclnnis, M. Weiss, H. D. Abruna and F. J. DiSalvo, *Journal of Nanoparticle Research* 2009, *11*, 965-980.

46 N. Gjostein. In Diffusion, ASM, Metals Park, OH 1973, 241-74.

47 H. Chen, D. Wang, Y. Yu, K. A. Newton, D. A. Muller, H. Abruna and F. J. DiSalvo, *Journal of the American Chemical Society* 2012, *134*, 18453-18459.

48 R. Jenkins & R.L. Snyder, *Introduction to X-ray Powder Diffractometry*, John Wiley & Sons Inc. 1996, 89-91.

49 D. Mott, J. Galkowski, L. Wang, J. Luo and C.-J. Zhong, *Langmuir* **2007**, *23*, 5740-5745.

50 D. DeSario in *Statistical analysis of compositional variation vs. particle size*, *Vol.* **2012**.

51 O. Koper and S. Winecki, *Nanoscale Materials in Chemistry*, John Wiley & Sons, Inc., Canada, **2001**, p. 292.

52 F. G. Shi, J. Mater. Res., 1994, 9(5), 1307-1313

CHAPTER 3

ORDERED TETRAGONAL PSEUDO-TERNARY Pt_2CoFe/C, Pt_2FeNi/C, and Pt_2CoNi/C NANOPARTICLES AS ACTIVE AND STABLE ORR ELECTROCATALYSTS

Introduction

Of the different classes of fuel cells, PEMFCs using hydrogen fuel are presently considered the best candidate for automotive applications due to their low operating temperatures, short warm-up time, and acceptable power density. In order for commercial implementation of PEMFCs for mobile and transportation applications, the technology needs to be more durable and affordable. There are several factors that influence the cost: one, the initial cost of the fuel cell; two, fuel cell lifetime; three, efficiency of the fuel cell; and four, fuel distribution station issues.

A major contributor to the high cost is the sluggish kinetics of the oxygen reduction reaction (ORR), which leads to high Pt loadings to reach reasonable power densities. Even with high Pt loading, the activation overpotential for ORR is about 0.4 V at operating current densities (about 1 A/cm^2 of electrode surface). The DOE targets for automotive applications is 0.2 gPt/kW, implying that the required amount of Pt in the cathode compartment should be reduced to less than 0.1 $mgPt/cm^2$.[1] To achieve this benchmark, more active and stable catalysts with lower Pt content will need to be developed and utilized.

Alloying has been a promising approach to producing advanced catalytic materials.[2-7] It has been shown that alloying Pt with one or more 3d transition metals

can effectively enhance ORR activity by factor of about 2 to 4, which shifts the half-wave potential to more positive potentials by about 30 mV. During ORR, oxygen molecules split into adsorbed oxygen atoms and subsequently form water by combining with H^+ transported from the anode by the polymer electrolyte and with electrons from the external circuit. One hypothesis for this activity enhancement is that it is due to changes in the physical structure of surface Pt atoms (the Pt-Pt bond distance). An O=O bond length (1.3A) that allows for bridge bonding between two Pt atoms (Pt-Pt distance ~2.7A depending on composition and structure) may play an important role in oxygen dissociation at Pt surface, with reduced Pt-Pt distance leading to an enhancement in ORR activity.[2] Another hypothesis for the observed ORR activity enhancement is that it is due to a change in the electronic structure of surface Pt atoms (via the ligand effect with the alloyed 3d transition metal) to favor oxygen dissociation.[4] Alloy nanoparticles, in which the atoms randomly occupy the appropriate Wyckoff positions in the space group of the appropriate crystal structure, may have differing catalytic activities of the Pt atoms even on the same crystallographic surfaces (say (111) or (110)). Since the number of Pt or 3d metal near neighbors on the surface will be only probabilistically determined, it is difficult to pinpoint the exact mechanism of activity enhancement among alloys.

Ordered intermetallic materials (bulk or nano), as defined in chapter 2, are different from their alloy counterparts in that there is no disorder (uniform Pt-Pt distances, all with the same environment on a given surface) and more uniform electronic environment as well as higher structural stability (from the higher heat of formation of ordered intermetallics compared to their alloy counterparts). Ordered

intermetallic bulk materials also show enhanced ORR activity and better durability.[8,9] However, synthesizing intermetallic nanoparticles in the sub 10 nm ranges can be challenging.

This chapter focuses on the ORR catalytic activities of ordered tetragonal Pt_2CoFe, Pt_2FeNi, and Pt_2CoNi nanoparticles, with an average particle size of 4-7 nm, synthesized and deposited onto carbon supports using the method described in chapter 2. The ORR activities were compared with a Pt/C 50 wt% ETEK standard.

3.1 Electrochemical Techniques

The general procedure for evaluating a catalyst's electrocatalytic activity involves the casting of a catalyst thin-film of known concentration on the surface of a glassy carbon electrode. Once this thin-film has dried, the catalyst electrochemical activity is evaluated in a standard three-electrode electrochemical cell with working, counter, and reference electrodes to obtain CVs in a de-aerated electrolyte and ORR polarization curves in an O_2-saturated electrolyte.

3.1.1 Electrolyte Selection

The electrochemical measurements were done in 0.1 M H_2SO_4. Pt and Pt-based electrode catalysts exhibit significantly lower ORR activity in 0.05 M H_2SO_4 compared to using $HClO_4$ as the electrolyte.[10,11] This is due to Pt surfaces being highly susceptible to the adsorption of the HSO_4^- and SO_4^{2-} ions. For 20% Pt/C standards, mass and specific activities in 0.1 M $HClO_4$ (at 0.9 V scanned at 20 mV/s with a Pt loading of $20\mu g_{Pt}/cm^2$) are 0.21 A/mg_{Pt} and 347 $\mu A/cm^2_{Pt}$ respectively, whereas the

same electrode under the same conditions in 0.05 M H_2SO_4 electrolyte showed mass and specific activities of 0.07 A/mg_{Pt} and 105 $\mu A/cm^2_{Pt}$ respectively.[12] Despite the lower activities in sulfuric acid electrolytes, we have chosen to carry out the experiments in 0.1 M H_2SO_4. To compare "apples to apples," the results of our catalysts are compared against a Pt/C Etek standard under the same conditions.

3.1.2 Catalyst Film

The catalyst ink should be well dispersed and not settle or clump. A small amount of Nafion ionomer is added to improve adhesion of the film to the electrode surface. The alcohol type is optimized for each catalyst; catalysts that are inherently hydrophobic, such as alloys or heat-treated samples, require inks with high alcohol to water ratios to obtain optimal dispersion.[13] For the Pt_2CoFe/C, Pt_2FeNi/C, and Pt_2CoNi/C catalyst (which are highly hydrophobic), a stock solution of 0.02% Nafion in Ethanol was prepared by mixing 0.4 mL of 5 wt% Nafion ionomer solution (Sigma-Aldrich) and 99.6 mL of Ethanol in a 100 mL volumetric flask. 2 mL of the stock solution was added to the appropriate amount of NPs/C sample to yield ~14.5 $\mu g/cm^2$ Pt loading on the electrode. A 5 μL solution of the ink is drop-cast onto a 5 mm diameter electrode.

3.1.3 Catalytic Activity

In an electrochemical reaction, the exchange current density and Tafel slope together define the activity of the catalyst. Due to difficulties and uncertainties of these parameters, alternative ways of defining catalyst activity of fuel cells have been

adopted in this thesis: mass activity and specific activity.

Mass Activity is defined as follows:

$$\mathbf{A_m = i_{0.9}/M}$$

Where A_m is the mass activity of the catalyst, $i_{0.9}$ is the current density in mA/cm^2 at 0.9V, and M is the mass loading of Pt in mg/cm^2. The electrocatalytic activity towards ORR is quantified at E = 0.90 V due to possible interferences from mass-transport losses that may appear below E = 0.90 V.[14] The mass activity is measured under saturated oxygen in the electrolyte as the reactant. In order to calculate the mass activity, the polarization curve for a given electrode is established in which the current density at 0.9V is obtained from current-potential data (with the current normalized to the geometric surface area per gram of the catalyst).

Specific Activity is defined by:

$$\mathbf{A_s = i_{0.9}/S_r}$$

Where A_s is the specific activity of the catalyst and S_r is the electrochemical surface area (ECSA) or "real" surface area of the catalyst in the electrode in m^2/g_{Pt}. The ECSA of the Pt working electrode is calculated from equation 3.1, using the hydrogen adsorption charge ($Q_{H\text{-}ads}$) in the negative-going potential scan (0.40-0.075 V) on CVs under inert atmosphere conditions and after correction for double-layer charging (by subtracting the current at 0.40V from the total current).

$$ECSA_{Pt,\,cat}\ (m^2 g_{Pt}^{-1}) = \left[\frac{Q_{H\text{-}ads}\ (\mu C)}{210\ (\mu C/cm^2_{Pt}) \times L_{Pt}\ (g_{Pt}/cm^2) \times A_{geo}\ (cm^2)}\right] 10^4 \qquad \text{(Eq. 3.1)}$$

The charge of full coverage for clean polycrystalline Pt is $Q_{H\text{-}ads}$ = 210 μC cm^{-2}, and is used as the conversion factor.[15-17] L_{Pt} is the Pt loading on the working electrode and A_g is the geometric surface area of the glassy carbon electrode. The assumption in this method is that the surface of the nanoparticle is pure Pt; that is, the second metal of the alloy or intermetallic phase is leached from the topmost monolayer near the surface, and that surface has the same properties for hydrogen adsorption as pure Pt. While this assumption is reasonable, it has not been experimentally proven.

3.2 Experimental

3.2.1 Synthesis of ordered fct Pt-Fe-Co-Ni pseudo ternary NPs

Synthesis of Pt_2CoFe-25KCl Nanoparticles: A similar method to that reported in Chapter 2, as well as in a paper from Chen *et al.*[18] is used. Briefly, 100mg of $PtCl_4$ (0.3 mmol), 32mg of Li_2CoCl_4 (0.15 mmol), 24mg $FeCl_3$ (0.15 mmol), and 63mg LiCl (1.5 mmol) were added to 100mL three necked round bottom flask and dissolved in 25mL of dry THF. The solution is then rapidly reduced, via syringe, with 8.5 mL 1.0 M KEt_3BH to reduce all the metals and scavenge all the chloride ions to make KCl, leaving a 15% excess reducing agent to be sure that any reducible impurities in the THF (like trace amounts of water) are also accounted for. The black suspension is then transferred to a 50 mL centrifuge tube, capped with a septum and fastened with copper wire. The solution is spun at 7000 rpm for 5 minutes and the clear supernatant is removed under a positive pressure of argon through a cannula needle. The black precipitate is then washed three times with 30mL aliquots of dry THF with a final wash with 30 mLs of dry hexanes using the above procedure. The black precipitate is

then dried under vacuum via schlenk-line. The dried black powder (nanoparticles encased in KCl, NP/KCl) is exposed to air slowly by backfilling the centrifuge tube with Ar, puncturing the septum with a needle and allowing the sample to sit overnight. This process appears to minimize oxidation of the particle surface upon air exposure.

Synthesis of Pt_2FeNi-25KCl Nanoparticles: Similar to the synthesis of Pt_2CoFe-25KCl Nanoparticles, using 100mg of $PtCl_4$ (0.3 mmol), 24mg $FeCl_3$ (0.15 mmol), 57mg Li_6NiCl_8 (0.15 mmol), and 38mg LiCl (0.9 mmol).

Synthesis of Pt_2CoNi-25KCl Nanoparticles: Similar to the synthesis of Pt_2CoFe-25KCl Nanoparticles, using 100mg of $PtCl_4$ (0.3 mmol), 32mg of Li_2CoCl_4 (0.15 mmol), 57mg Li_6NiCl_8 (0.15 mmol), and 32mg LiCl (0.75 mmol).

Formation of the ordered intermetallic fct phase: The NPs/KCl is transferred to a silica tube and sealed under vacuum. The samples were then annealed at 550^{o}C for 4 hrs, cooled to 450^{o}C over 3 hrs, then held at 450^{o}C for 15 hrs, finally cooled to room temperature over 5 hrs.

3.2.2 Transfer of NP catalyst to carbon black support

Transfer of NPs to carbon black (C-Blk) support: 15mg of C-Blk (Vulcan XC72R, untreated) and 5mL of ethylene glycol (EG) in a 20-mL scintillation vile, was sonicated (Branson 3510) for 1 hr. 26mg of NPs/KCl with 1.5mL of EG were ultrasonicated (Microson Ultrasonic Cell Disruptor XL) for 30 seconds in a 5mL vial submerged in an ice bath. The NP/KCl/EG soln. is then added to C-Blk/EG soln. and ultrasonicated for an additional 10 minutes while submerged in an ice bath. The final solution was centrifuged at 3500 rpm for 20 minutes, the supernatant was removed

and the black precipitated was washed 5 times with 10mL aliquots of Millipore water. After the final wash, the black precipitate was dried at 125^{o}C in air for 90 minutes.

3.2.3 Structural Characterization

The crystalline structure of the NP catalysts was examined with a Rigaku Ultima VI powder X-ray diffractometer (PXRD) with Copper K-α radiation (λ = 1.5406 Å and $K_{\alpha 2}$, λ = 1.5444 Å). Lattice parameters and Pt-Pt bond distances of the NP catalysts were analyzed from the PXRD patterns via Rietveld refinements using GSAS software package.

3.2.4 TGA: Determination of NPs/C wt%

The mass percent of NPs on carbon black support was determined using Thermogravimetric analysis (TGA). The samples were heated to 550^{o}C at a rate of 10^{o}C/minute, and then held at that temperature until the mass stabilizes for at least 10 minutes. The measurements were performed under a flow of air to completely oxidize the carbon support material. Complete oxidation of the non-Pt transition metals is also assumed (formation of Fe_2O_3, Co_3O_4, and NiO) and the percent mass difference is subtracted from the experimental value. The final mass of Pt and metal oxide allows a direct calculation of the mass fraction of the nanoparticles in the Vulcan nanoparticle composite.

3.2.5 Particle Size Analysis

Average particle size of the NPs/C were determined from TEM images (FEI

T12 Spirit TEM, Tecnai 200 kV), by averaging the diameter of at least 100 individual particles. At the same time, a rough estimate of the particle size distribution is obtained.

3.2.6 Electrochemical Characterization

Cyclic voltammograms (CV) of the catalyst materials were recorded at room temperature between 0.05 and 1.10 V vs. RHE at a scan rate of 20 mVs^{-1} after flushing the electrolyte with N_2 for 30 minutes prior to the experiment. The ORR activity of the deposited nanomaterials was studied at room temperature using rotating disk electrode (RDE) techniques in the potential range of 0.40 and 1.1 V vs. RHE in the negative direction with a scan rate of 20 mVs^{-1}. The electrochemical cell was flushed with O_2 for 30 minutes before the experiment and the flow was maintained during the course of experiments to assure an O_2 saturated solution. The rotation speed of the disk electrode for each ORR experiment was 1600 rpm. Both CV and RDE experiments were conducted in 0.1 M H_2SO_4, where a RHE was used as the reference electrode and a Pt wire as a counter electrode.

3.2.7 Stability Studies

The catalysts were subjected to 2000 electrochemical potential cycles to examine the stability in terms of real platinum surface area, ORR activity, and the change in composition of Pt and non-Pt metal in the electrode. The potential cycling was interrupted several times to record the CV and RDE voltammograms. CV and RDE voltammograms of all the catalysts were recorded after 25 and 2000 potential

cycles. The elemental composition of all the electrodes after the final CV and RDE experiments were measured with EDS. All the potential cycling experiments were carried out at room temperature and ambient pressure.

3.2.8 Elemental Analysis

Pt, Fe, Co, and Ni atomic percentages of all the catalysts (no carbon) were determined via EDS. The bulk compositions of all the materials were determined with a SEM Philips XL-30-FEG (field emission gun) equipped with EDS. At least five different individual spots were chosen and measured to determine composition on each sample. The electron beam is roughly 1 μm in diameter and collects data from roughly 10^5 - 10^6 nanoparticles (assuming a excitation and detection sphere of 1 μm^3). One generally expects that this will closely reflect the metal ratio of the precursors, unless specific metals are lost during the workup.

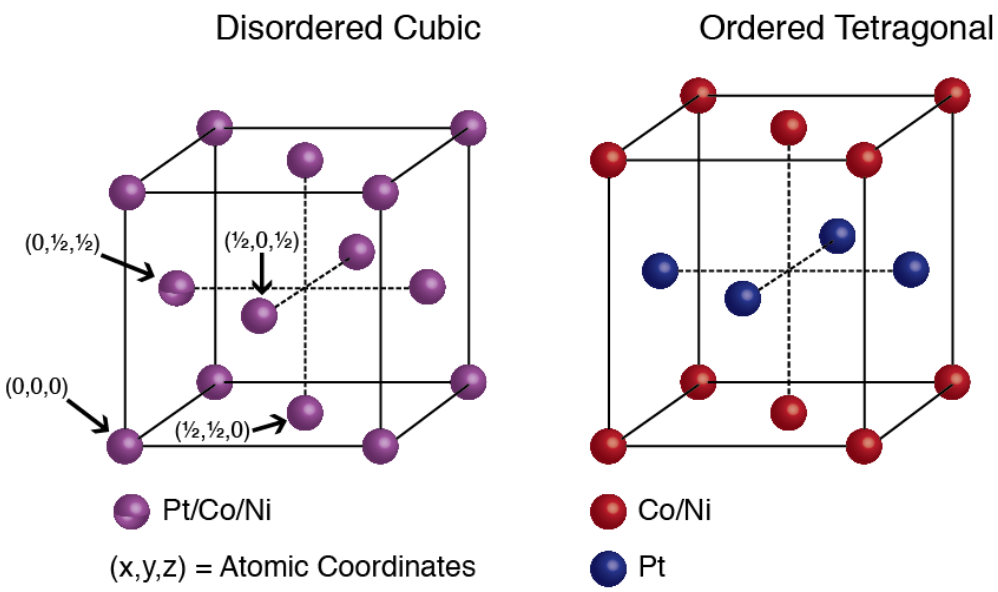

Atomic Coordinates	Disordered Cubic Site Occupancy (%)			Ordered Tetragonal Site Occupancy (%)		
	Pt	Co	Ni	Pt	Co	Ni
(0,0,0)	50	25	25	0	50	50
(½,½,0)	50	25	25	0	50	50
(½,0,½)	50	25	25	100	0	0
(0,½,½)	50	25	25	100	0	0

Figure 3.1 Unit cell of disordered cubic and ordered tetragonal Pt_2CoNi. The 4 Wyckoff positions are given in the form of (x,y,z) coordinates along with the site occupancy of Pt, Co, and Ni atoms in both unit cells.

3.3 Results and Discussion

3.3.1 Structure Analysis

As discussed in Chapter 2, the nanoparticles prepared at room temperature exhibit a disordered face-centered-cubic structure. Upon annealing at 550^{o}C, the NPs transition from an alloy to an ordered tetragonal structure. The difference in the unit cell and site occupancy of Pt, Co, and Ni atoms are given in Figure 3.1. The XRD spectra of tetragonal Pt_2CoFe/C, Pt_2FeNi/C, and Pt_2CoNi/C are depicted in Figure 3.2 and 3.3. Figure 3.2 shows the individual XRD plots with the corresponding database peak locations and intensities (indicated by the black lines) indicating the ordered structure as expected. The broad hump around 23^{o}, indicated by the dashed line, is the XRD peak of the carbon black support material.

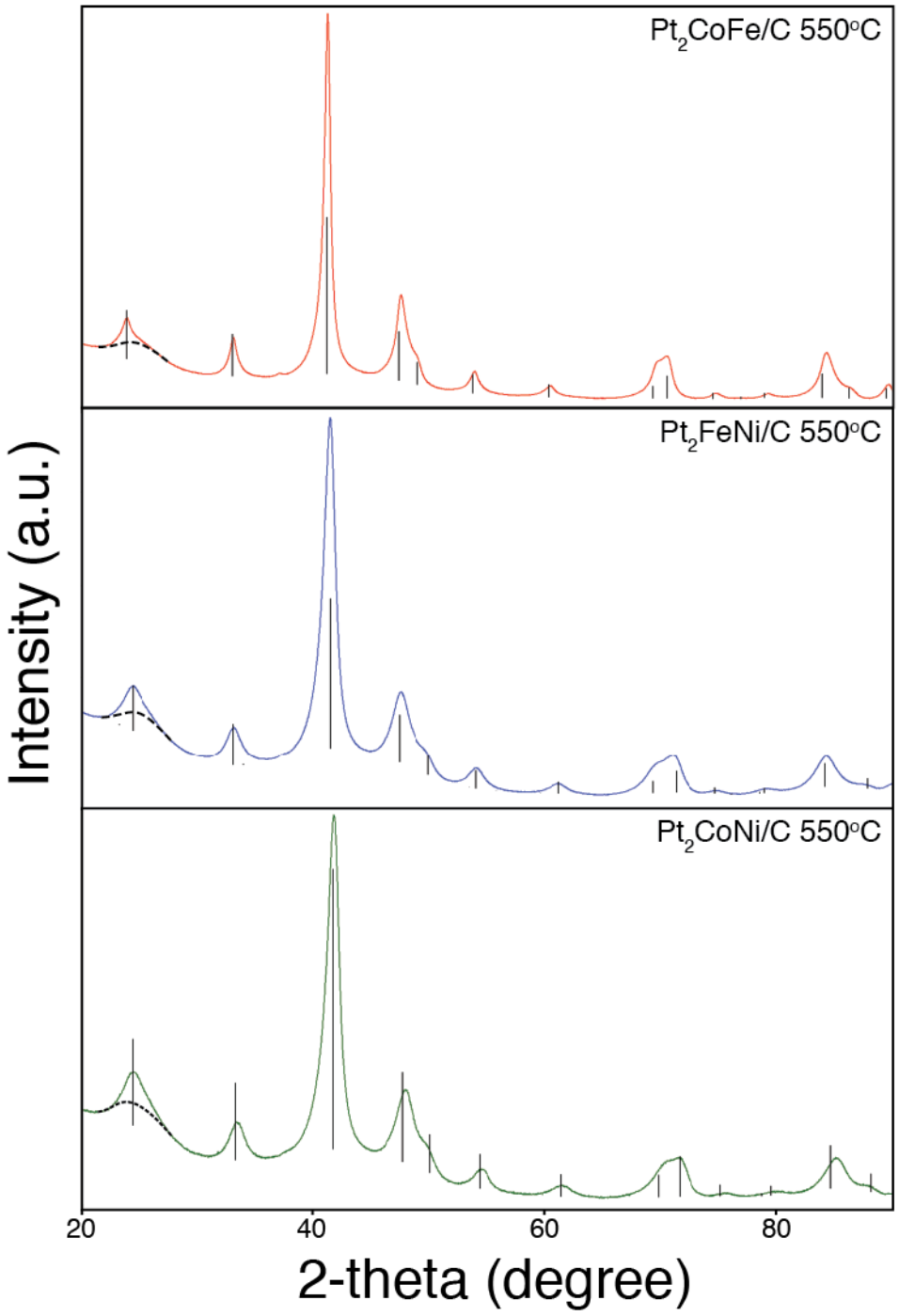

Figure 3.2 PXRD pattern of Pt_2CoFe/C (top), Pt_2FeNi/C (middle), and Pt_2CoNi/C (bottom) made at 550°C. The black lines denote the peak locations of fct Pt_2CoFe (database card # 01-077-7477), Pt_2FeNi (database card # 01-089-2026), and Pt_2CoNi (database card # 01-077-7530) for the top, middle, and bottom PXRD patterns respectively. The dashed line around 23° is the broad peak from the carbon black support material.

Figure 3.3 is an overlay of the same three XRD patterns to emphasize the subtle peak shifts that arise from different lattice parameters. The atomic size of Fe, Co, and Ni is 156, 152, and 149 pm respectively.[19] Thus, the lattice parameters are expected to increase in the order of $Pt_2CoNi < Pt_2FeNi < Pt_2CoFe$. The (111) peak (the peak at roughly 41^o two-theta), shifts to higher angles in the order of $Pt_2CoFe < Pt_2FeNi < Pt_2CoNi$ (XRD peak shift to higher angles is indicative of smaller lattice parameters).

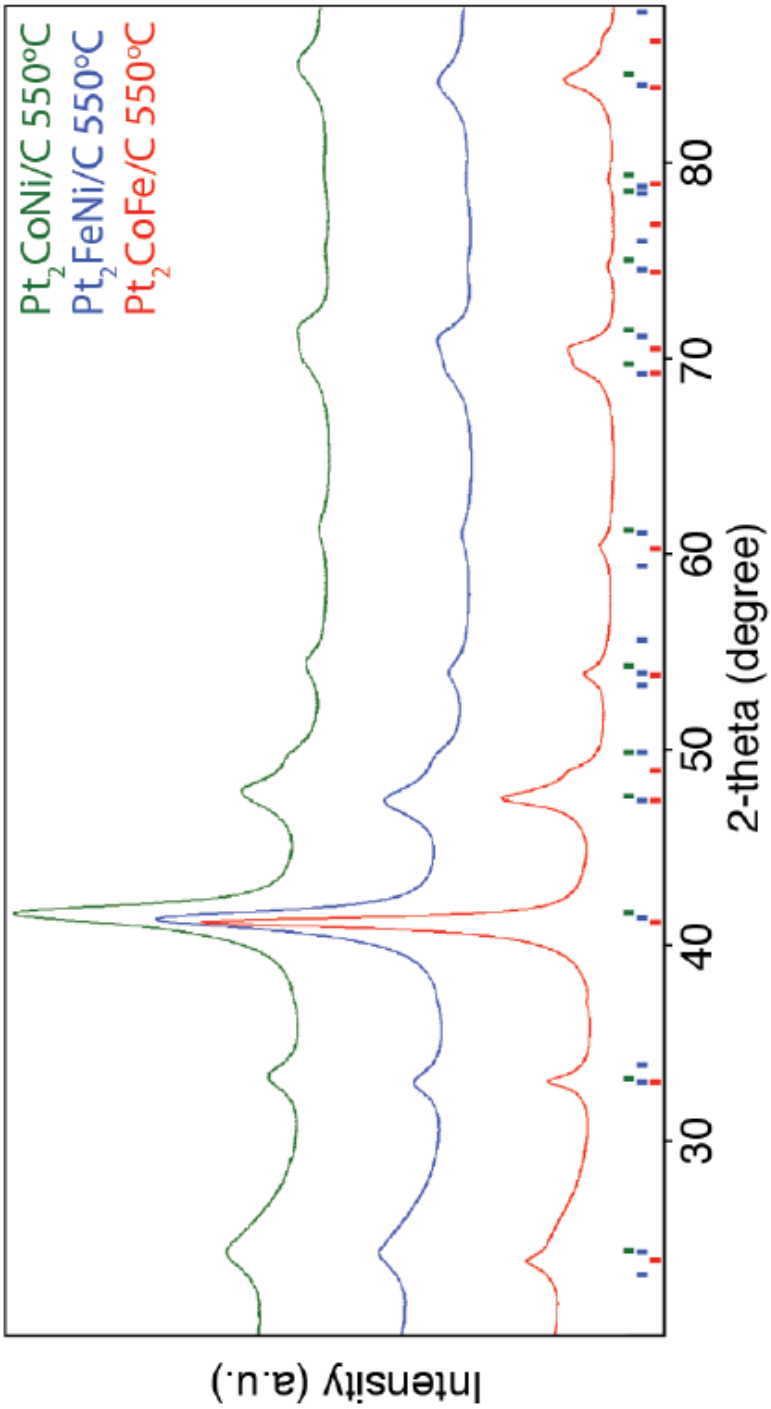

Figure 3.3 PXRD pattern of Pt_2CoFe/C (red), Pt_2FeNi/C (blue), and Pt_2CoNi/C (green) made at 550°C. The tick marks indicate the peak locations of Pt_2CoFe (red; database card # 01-077-7477), Pt_2FeNi (blue; database card # 01-089-2026), and Pt_2CoNi (green; database card # 01-077-7530).

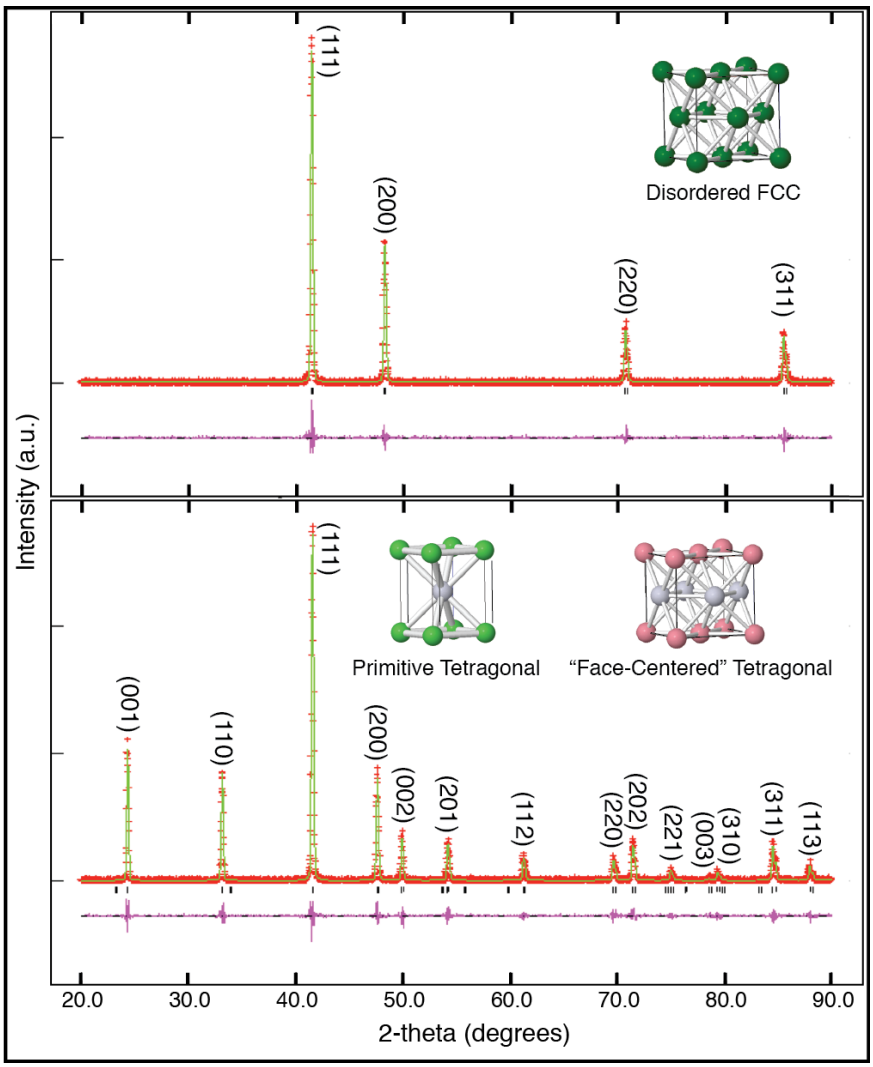

Figure 3.4 Simulated PXRD patters of disordered cubic (top) and ordered tetragonal (bottom) of Pt_2CoNi. Since the X-ray scattering factors for Co and Ni are very similar (in the ratio of 27:28 respectively), it is not possible to determine if Co and Ni are ordered or disordered on the 2(b) site. We assume here that these two 3d elements are disordered on that site. Pt_2CoNi unit cell is primitive tetragonal, but to better visualize the similarities between the ordered tetragonal and the disordered cubic, the "face-centered" tetragonal cell is shown and has the volume of two primitive tetragonal cells. The dark green spheres in the disordered FCC unit cell represent Pt/Co/Ni atoms in a 50/25/25 percent occupancy respectively. The silver sphere in the primitive tetragonal cell represents Co/Ni atoms in a 50/50 percent occupancy and the green spheres represents Pt atoms. The Pink spheres in the "face-centered" tetragonal cell represent Co/Ni atoms and the silver spheres represent Pt atoms.

Rietveld refinement is a technique used to characterize crystalline materials.

The XRD pattern of powdered samples results in a pattern characterized by reflections (peaks in intensity) at certain positions. The height, width, and position of these reflections can be used to determine many aspects of the materials structure, such as lattice parameters and site occupancies, rather accurately.[20] In collaboration with Minghui Yang, refinement of Pt_2CoFe, Pt_2FeNi, and Pt_2CoNi was done and the key information is summarized in Table 3.1. A simulated Rietveld refinement plot of disordered and ordered Pt_2CoFe is depicted in Figure 3.4, which shows the "ordering peaks" (the extra XRD peaks that arise when transitioning from a disordered fcc structure to an ordered tetragonal structure on annealing) that are seen in the three catalyst materials. Figure 3.5 is a representative Rietveld refinement done on a Pt_2CoNi/C sample annealed at 550^oC.

Table 3.1 Refinement results of the lattice parameters for the primitive tetragonal unit

cell for Pt_2CoFe/C, Pt_2FeNi/C, Pt_2CoNi/C nanoparticles annealed at 550°C. The "a-axis" for the "face-centered" unit cells is 3.810, 3.828, and 3.800 Å respectively. As a reference, the unit cell data of Pt is given. Pt_2CoNi/C sample annealed at 550°C ([1]) had a large fitting error (χ^2), so the refinement was repeated with another sample annealed to higher temperatures (625°C for 24hrs) and is labeled accordingly ([2]).

Formula	Pt_2CoFe	Pt_2FeNi	Pt_2CoNi	Pt
System	Tetragonal	Tetragonal	Tetragonal	Cubic
Space Group	*P4/mmm*	*P4/mmm*	*P4/mmm*	*Fm-3m*
a, b (Å)	2.701(2)	2.707(2)	2.656(2)[1] 2.694(1)[2]	3.9242
c (Å)	3.737(2)	3.681(2)	3.621(4)[1] 3.708(1)[2]	3.9242
α, β, γ (degree)	90	90	90	90
Volume ($Å^3$)	27.28(1)	26.97(4)	25.54(8)[1] 26.91(4)[2]	60.430
Z	0.5	0.5	0.5	1
wR_p	0.0314	0.0567	0.0209[1] 0.0464[2]	
R_p	0.0232	0.0425	0.0165[1] 0.0327	
χ^2	19.54	14.3	40.39[1] 6.877[2]	
Pt-Pt distance (Å)	2.701	2.707	2.656[1] 2.694[2]	2.775

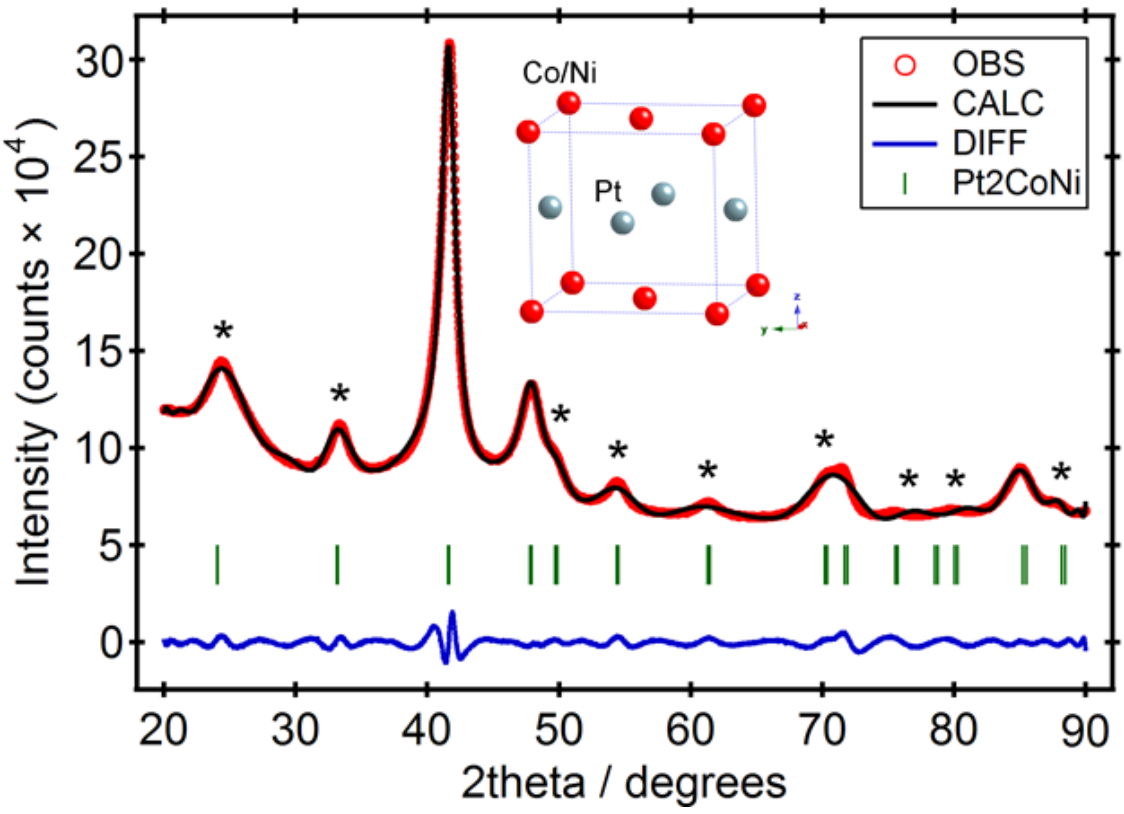

Figure 3.5 Sample Rietveld refinement plot of Pt_2CoNi/C. The red pattern made from many red circles is the experimental data. The black line is the calculated pattern. The blue line represents the difference between the calculated and observed patterns. The green tic marks represent the peak locations of tetragonal Pt_2CoNi bulk material from the database card # 01-077-7530. The (*) indicates the peaks that appear due to the effects of the ordering of Pt and Fe/Co.

The XRD patterns of Pt_2CoFe/C, Pt_2FeNi/C, and Pt_2CoNi/C samples agree reasonably well with the reported peak positions and relative intensities of their bulk counterparts, with the exception of nano-Pt_2CoNi (*vide intra*). The expected trend in volume and lattice parameters follows the decreasing metallic radii of the 3d elements from Fe, to Co, to Ni, respectively. Figure 3.6 shows the cell volume of bulk and nano PtFe, PtCo, PtNi, Pt_2FeNi, Pt_2FeCo, and Pt_2CoNi materials.[21,22,27-30] As expected, there is a linear decrease in lattice parameters and volume as the 3d element changes from Fe > FeCo > FeNi > Co > CoNi > Ni between the respective binaries, except for nano-Pt_2CoNi. Note that the goodness of fit ($\chi 2$) for the Pt_2CoNi pattern (Table 3.1) is more than twice as large as for the other two ternaries. A large $\chi 2$ indicates a poor fit and likely larger errors in fitting lattice parameters as well as intensities.

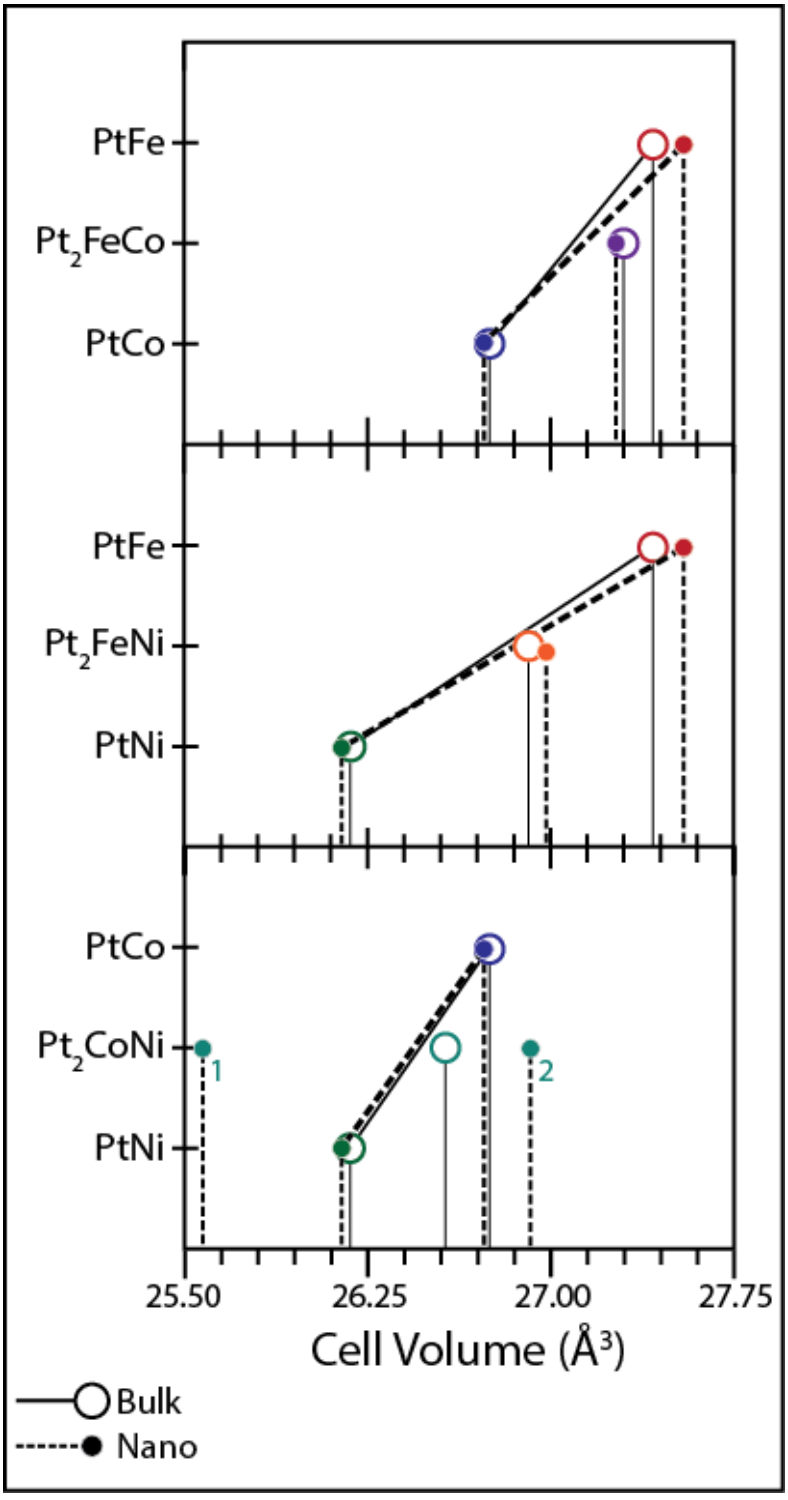

Figure 3.6 Plot of bulk and nano cell volumes of PtFe, PtCo, PtNi, Pt_2FeCo, Pt_2FeNi, and Pt_2CoNi. The Pt_2CoNi nano phase labeled "1" and "2" represent the cell volumes (from Table 3.1) of sample 1 and 2 respectively.

Figure 3.7 shows the lattice parameters (a and c) of bulk and nano Pt_2FeCo, Pt_2FeNi, and Pt_2CoNi along side their corresponding binary phases. Looking at just the lattice parameter "a," the trend follows: PtFe > Pt_2FeNi > Pt_2FeCo > PtNi > Pt_2CoNi > PtCo. Again, the "a" lattice parameter is too small for nano-Pt_2CoNi^1, but when the analysis was repeated, nano-Pt_2CoNi^2 had an "a" lattice parameter near expected value (though the "c" parameter of the second sample is too large). The decrease of the "a" parameter going from PtNi to PtCo is surprising and opposite the trend from PtCo to PtFe or from PtNi to PtFe (as indicated by the negative slope in Figure 3.7). The anomalous trend is balanced with an expansion in the "c" parameter so that the unit cell volume follows the expected trend in atomic size. Thus, the trend in Pt-Pt bond distances (lattice parameter "a") of the pseudo-ternary nanoparticle samples obtained in Table 3.1 agrees well with the trend observed in the bulk phase (Pt_2FeNi > Pt_2FeCo > Pt_2CoNi).

Again, there is anomalous behavior in the c-axis, now in the series from PtNi to PtFe (non-linear but small changes) and small deviations from linear behavior on going from nano-PtNi to nano-PtCo. The latter is likely an experimental artifact due to the poor Rietveld fit, as mentioned previously for the a-axis.

The lattice parameters of each pseudo-ternary material should be near the line connecting the two binary phases (solid line for bulk phases and dashed lines for nano_. The only significant deviation from Vegard's law (predicts linear variation in lattice parameter on alloying as long as the structure remains the same) is seen in the nano-Pt_2CoNi sample, but this deviation is likely due to large statistical errors in the fitting of the X-ray patter to the structural model.

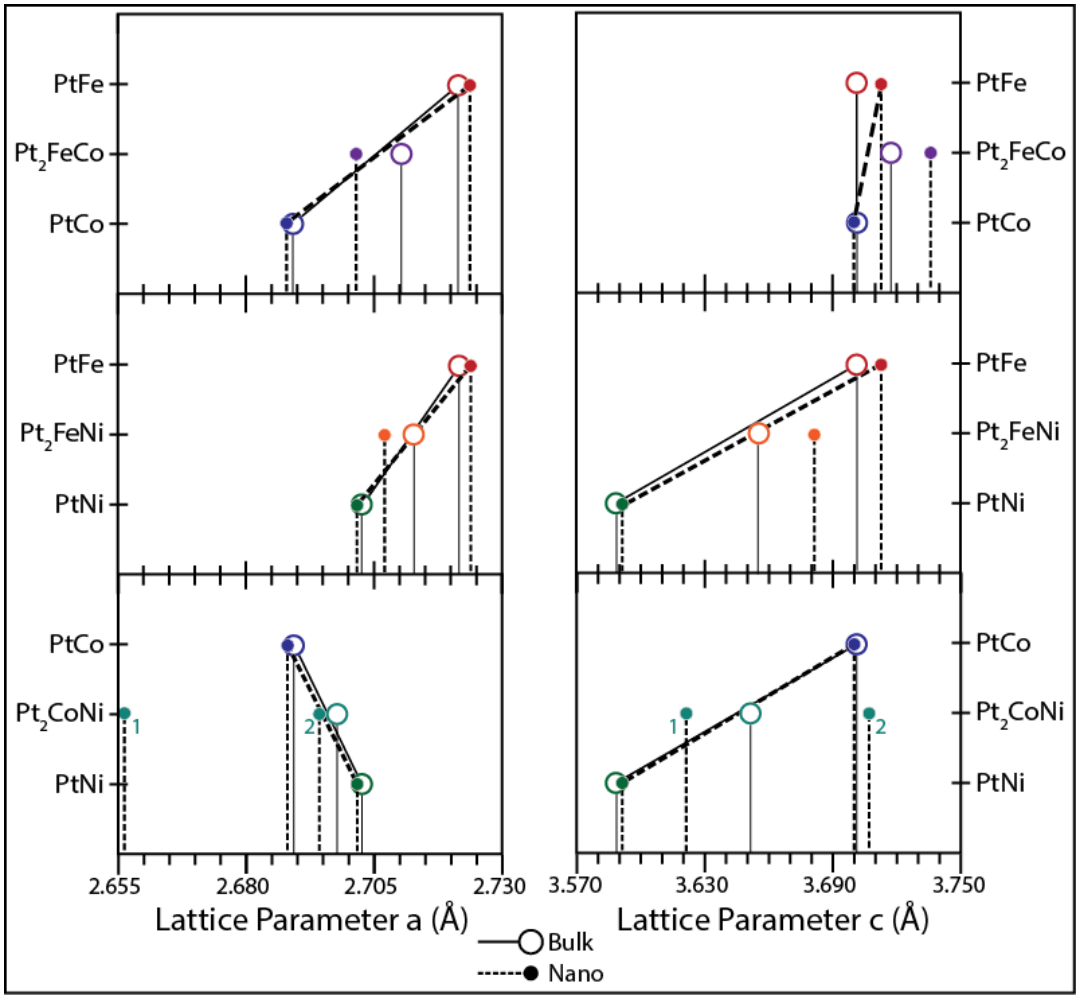

Figure 3.7 Lattice parameters (a and c) of bulk and nano PtFe, PtCo, PtNi, Pt_2FeCo, Pt_2FeNi, and Pt_2CoNi materials. The vertical dashed lines and solid circles mark the lattice parameters of nanoparticle samples, with the solid vertical lines and open circles marking the lattice parameters of the bulk samples. The lines connecting the binary phases (dashed for nano and solid for bulk) mark the expected progression in lattice parameter of the ternary ordered alloy according to Vegard's Law.

This may come from poor modeling of the peak profiles, since there is a distribution of particle sizes leading to complex peak shapes (since the broad diffraction peaks decreases the reliability of Rietveld refinement).

3.3.2 Elemental Analysis

Figure 3.8 shows the EDS spectra of Pt_2CoFe/C, Pt_2FeNi/C, and Pt_2CoNi/C catalysts before ORR testing. It is clear that samples are "pure" in that no other elements were detected. The atomic compositions of the samples before and after stability tests are given in Table 3.2. Roughly 10% of the 3d metal atoms are lost due to leaching after 2000 CV measurements (cycled between 0.05 – 1.10 V at a scan rate of 50 mV/s in 0.1 M H_2SO_4). Any exposed 3d metal atoms on the surface of the particles are expected to dissolve within the first 2 sweeps; however, typical alloy nanoparticles with initial PtM (M = 3d transition metal) ratios of 50:50 see a reduction of roughly 30 at% of the non-Pt element, stabilizing at the Pt at% of 75-80%.[23] Thus, it is possible to conclude that ordered nanomaterials are structurally more stable (less prone to leaching) than their alloy counterparts under cathodic operating conditions.

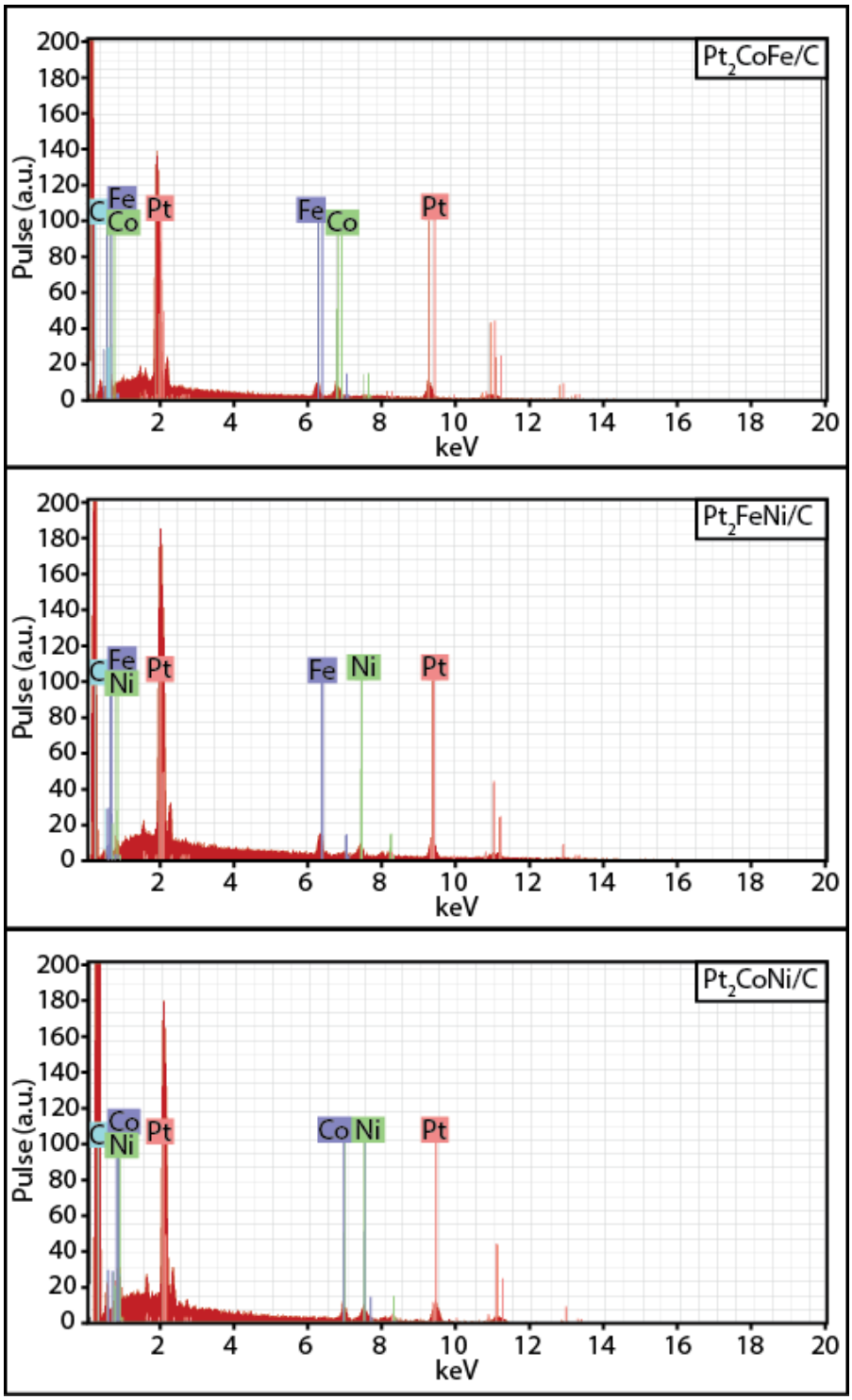

Figure 3.8 EDS spectra of Pt_2CoFe/C (top), Pt_2FeNi/C (middle), and Pt_2CoNi/C (bottom). The x-ray energies detected are indicative of $K_{a1,2}$ and $L_{a1,2}$ for Fe, Co, and Ni as well as the M_{a1} and L_{a2} of Pt as indicated by the labeled colored lines.

Table 3.2 EDS results of the catalyst materials before and after electrochemical measurements (2000 CVs from 0.05 – 1.10 V at a scan rate of 20 mV/s in 0.1 M H_2SO_4)

Electrode	**Pt_2CoFe/C**			**Pt_2FeNi/C**			**Pt_2CoNi/C**		
Atom	**Pt**	**Co**	**Fe**	**Pt**	**Fe**	**Ni**	**Pt**	**Co**	**Ni**
As Made Samples	50.9	25.7	23.4	50.5	26.6	22.9	49.3	25.0	25.7
After 2000 CVs	61.1	18.9	20.0	63.9	16.9	19.2	61.6	18.5	19.9

It is also possible to estimate the thickness of the Pt "skin" or "shell" knowing the atomic composition and particle size. The underlying assumptions are: 1, the particles are spherical and all have the same uniform composition (see insert in Figure 3.9); 2, the interface between the Pt skin and the underlying PtM material is sharp; 3, the distribution of particle sizes can be represented by the average diameter of the particles; and 4, the volume of a Pt atom is roughly the same as the volume of the M atom.

Estimation of Pt-Shell thickness from atomic composition and particle size:

$$\#\text{ of Pt atoms} = \underbrace{\frac{(D - 2t)^3}{V_{Pt}+V_M}}_{\text{core}} + \underbrace{\frac{(D^3 - (D-2t)^3)}{V_{Pt}}}_{\text{shell}}$$

$\boxed{V = \text{Vol. of Atom}}$

$$\#\text{ of M atoms} = \underbrace{\frac{(D - 2t)^3}{V_{Pt}+V_M}}_{\text{core}} \qquad \boxed{V_{Pt} \approx V_M}$$

$$\frac{\#\text{ of M atoms}}{\#\text{ of Pt atoms}} = \frac{\frac{(D - 2t)^3}{2V_{Pt}}}{\frac{(D - 2t)^3}{2V_{Pt}} + \frac{2(D^3 - (D-2t)^3)}{2V_{Pt}}}$$

$$\frac{\#\text{ of M atoms}}{\#\text{ of Pt atoms}} = \frac{1}{1 + \frac{2(D^3 - (D-2t)^3)}{(D - 2t)^3}} \qquad \boxed{x = \frac{t}{D}}$$

$$\frac{\#\text{ of M atoms}}{\#\text{ of Pt atoms}} = \frac{1}{1 + \frac{2(1 - (1-2x)^3)}{(1 - 2x)^3}}$$

A plot of atomic composition (M/Pt) vs. x (t/D, where $0 \leq t/D \leq 0.5$) is shown in Figure 3.9. From the (M/Pt) values from Table 3.2 (0.64, 0.57, and 0.62 for Pt_2CoFe, Pt_2FeNi, and Pt_2CoNi respectively), and the average particle sizes after 2000 cycles in Table 3.3 (5.1, 6.3, and 8.0 nm diameters for Pt_2CoFe, Pt_2FeNi, and Pt_2CoNi respectively), the average Pt-shell thickness for Pt_2CoFe, Pt_2FeNi, and Pt_2CoNi are 0.20, 0.32, and 0.34 nm respectively, which is roughly 1 monolayer of Pt. In this range of composition, the M to Pt ratio decreases rapidly with small increases in "t." Consequently, the EDS signal will be very sensitive to small changes in the thickness of the leached layer.

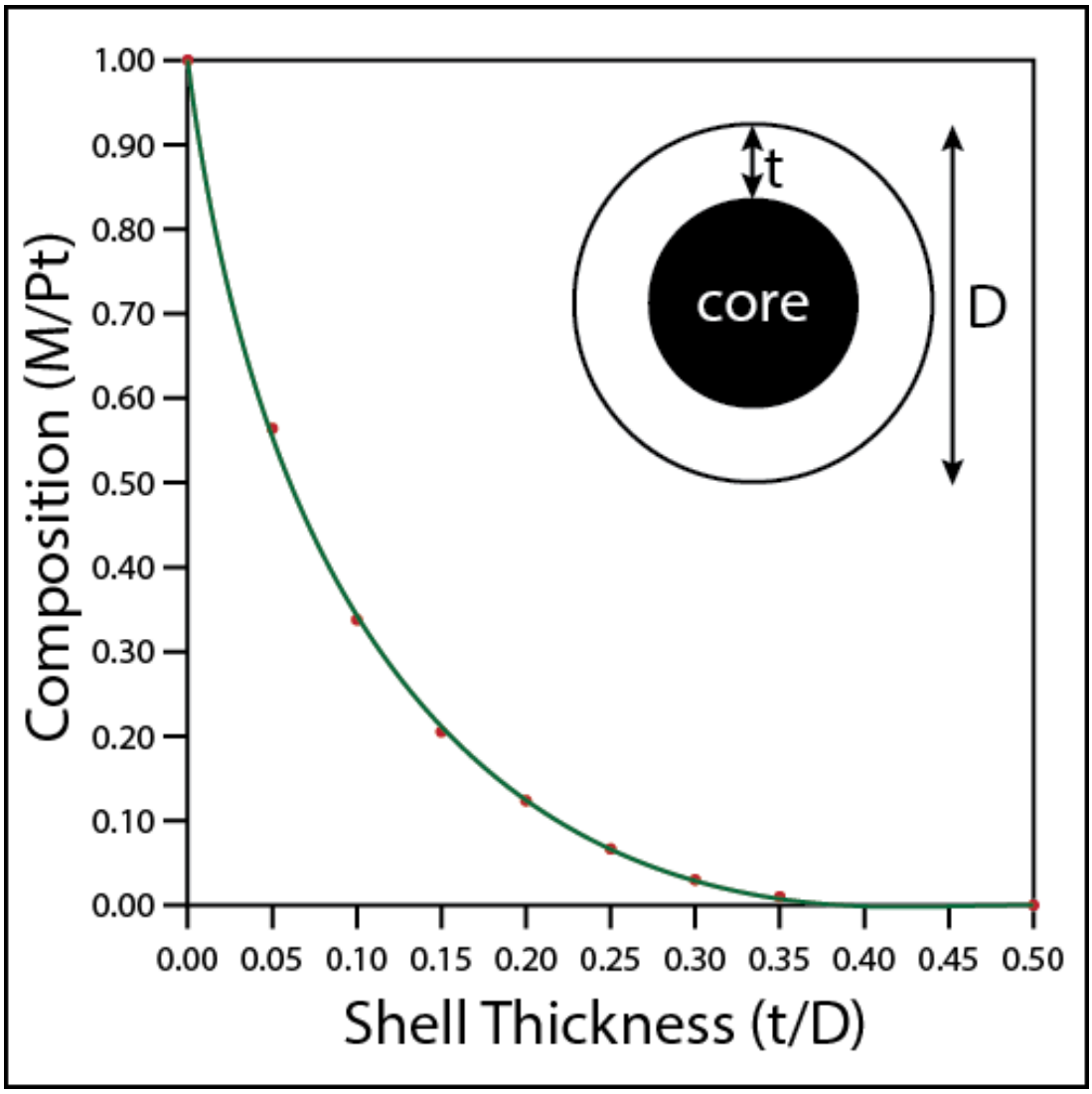

Figure 3.9 Plot of composition (M/Pt) vs. shell thickness (t/D) using the approximations discussed in section 3.3.2.

3.3.3 TGA Analysis: NPs/C

The TGA of ordered Pt_2CoFe/C, Pt_2FeNi/C, and Pt_2CoNi/C material is shown in Figure 3.10. After oxidizing the carbon support material to CO_2, the percent mass of nanoparticles on carbon was determined to be 26.20%, 25.68%, and 24.04% for Pt_2CoFe/C, Pt_2FeNi/C, and Pt_2CoNi/C respectively. Correcting for the oxidation of the non-Pt metal (the formation of Fe_2O_3, Co_3O_4, and NiO), the catalyst loading was determined to be 17.24 wt%, 17.76 wt%, and 16.69 wt% for Pt_2CoFe/C, Pt_2FeNi/C, and Pt_2CoNi/C respectively. These values compare well with the theoretical loading of 20 wt% as determined by the masses of reactants and carbon black used in the synthesis. This means that 100 +/- 5 wt% of the catalyst is bound to the support and not lost to the supernatant or container walls.

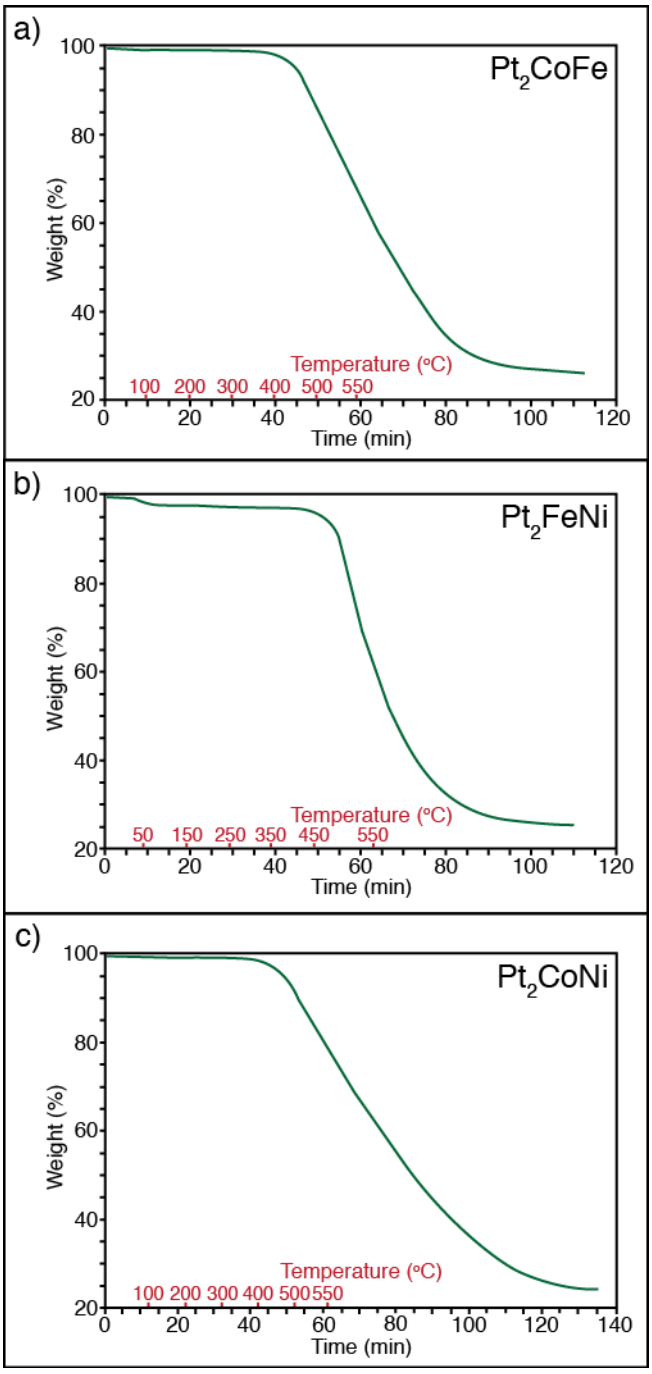

Figure 3.10 TGA results for heating Pt_2CoFe/C, Pt_2FeNi/C, and Pt_2CoNi/C catalyst materials. Samples were heated to 550°C at a rate of 10°/min, and then held at that temperature for at least 50 minutes until the weight stabilized.

3.3.4 Average Particle Size

TEM images of Pt_2CoFe/C, Pt_2FeNi/C, and Pt_2CoNi/C annealed at 550^oC are shown in Figure 3.11 next to the corresponding histogram. TEM images and histograms of the same electrode materials after electrochemical stability tests (cycling 2000 times from 0.05 – 1.10 V at 50 mV/s) are shown in Figure 3.12. The average particle sizes of Pt_2CoFe/C, Pt_2FeNi/C, and Pt_2CoNi/C before and after electrochemical tests are summarized in Table 3.2. After cycling, the average particle size increases, either through Oswald ripening and/or coalescence.

Table 3.3 Particle Size Analysis of electrode materials before and after 2000 CVs. CVs were done in 0.1 M H_2SO_4 from 0.05 – 1.10 V at a scan rate of 50 mV/s.

Electrode Material	**Particle Size (nm)**	
	As Made Samples	**After 2000 CVs**
Pt_2CoFe/C	3.9	5.1
Pt_2FeNi/C	4.0	6.3
Pt_2CoNi/C	3.9	8.0

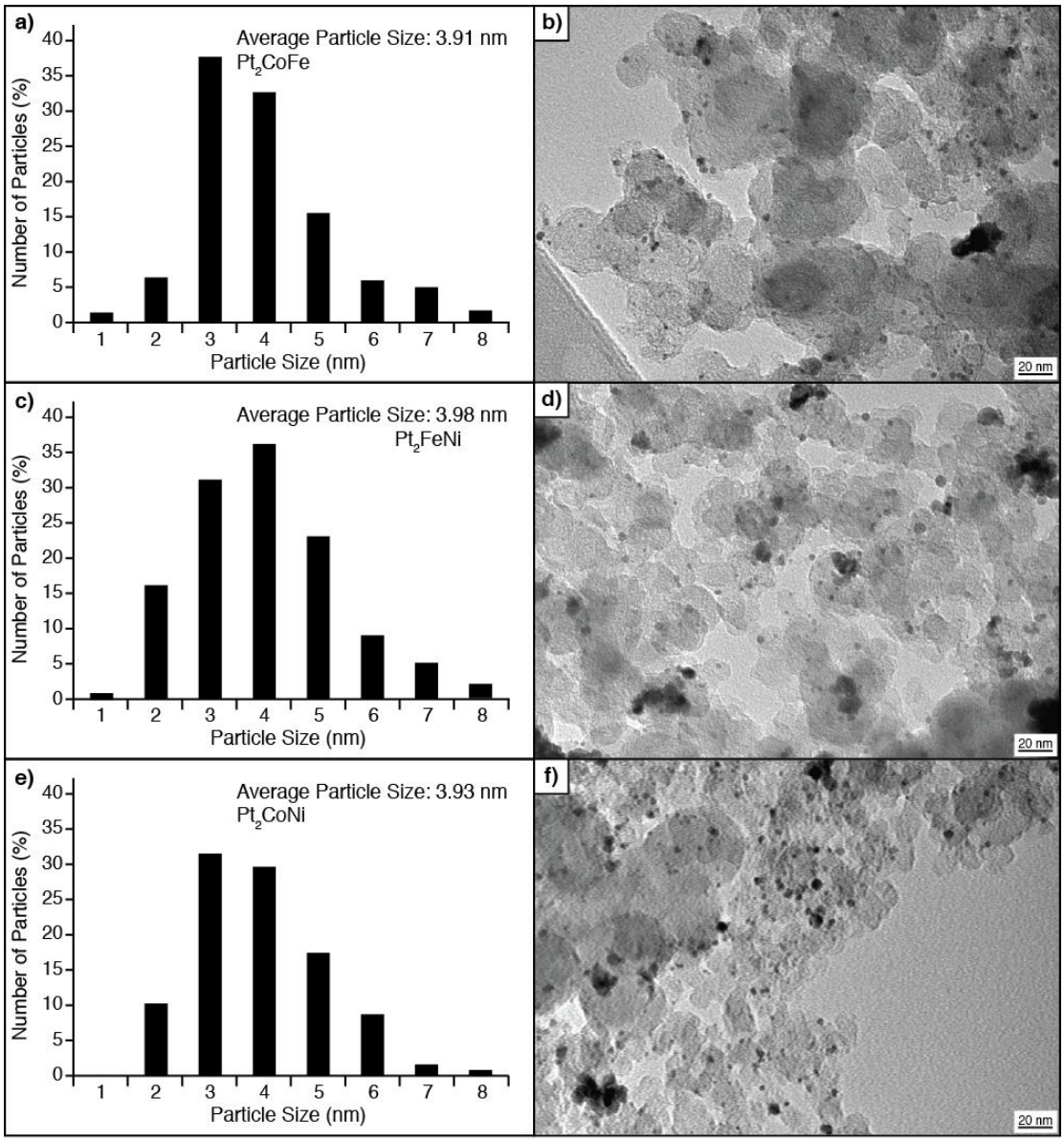

Figure 3.11 Particle size histograms and corresponding TEM image of Pt_2CoFe/C (a & b), Pt_2FeNi/C (c & d), and Pt_2CoNi/C (e & f). The histograms were made by analyzing at least 100 particles and normalized to the total percent of the analyzed particles, ignoring obvious aggregated masses.

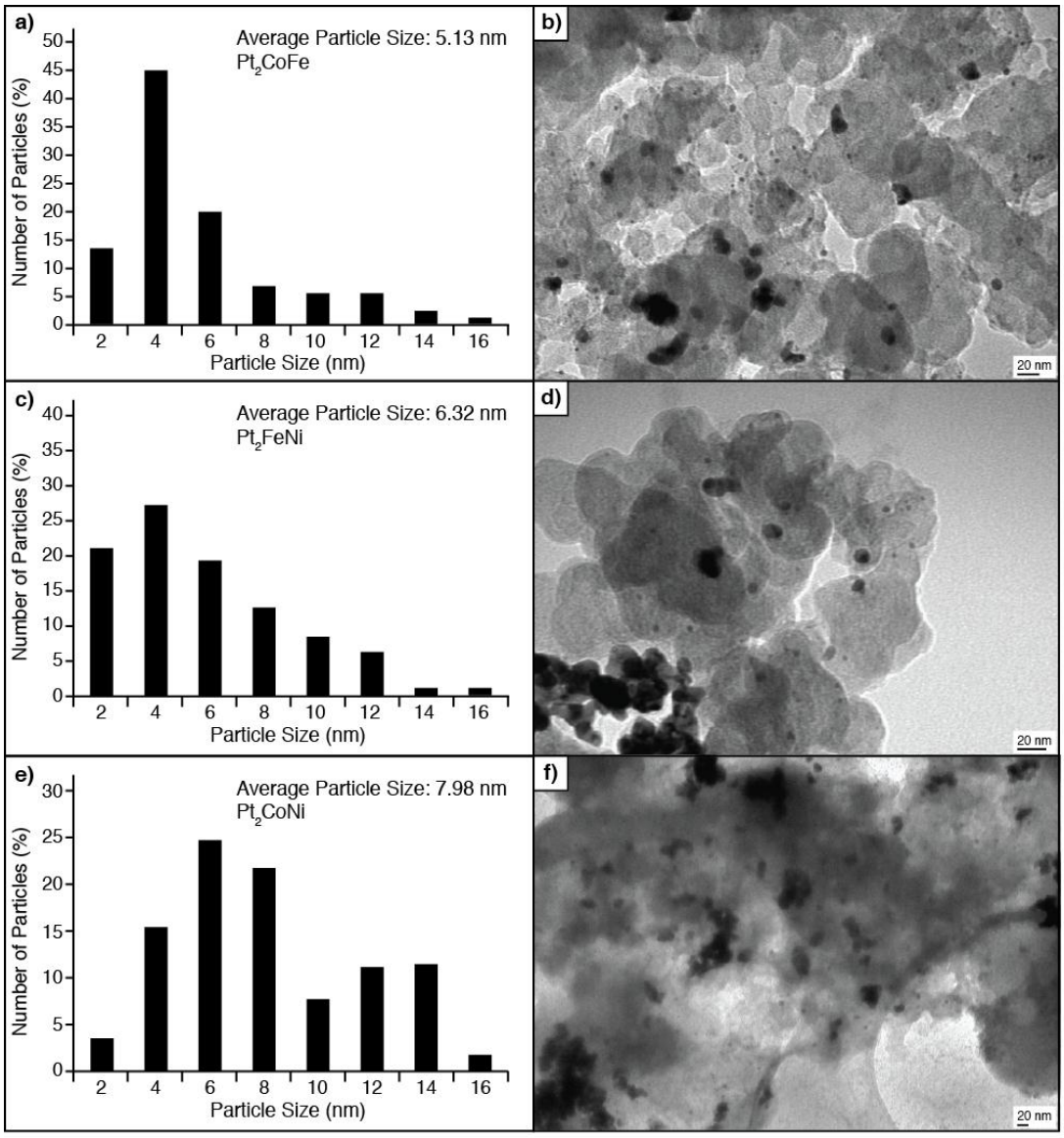

Figure 3.12 Particle size histograms and corresponding TEM image of Pt_2CoFe/C (a & b), Pt_2FeNi/C (c & d), and Pt_2CoNi/C (e & f) after stability test (1000 cycles from 0.05 – 1.10 V at 50 mV/s).

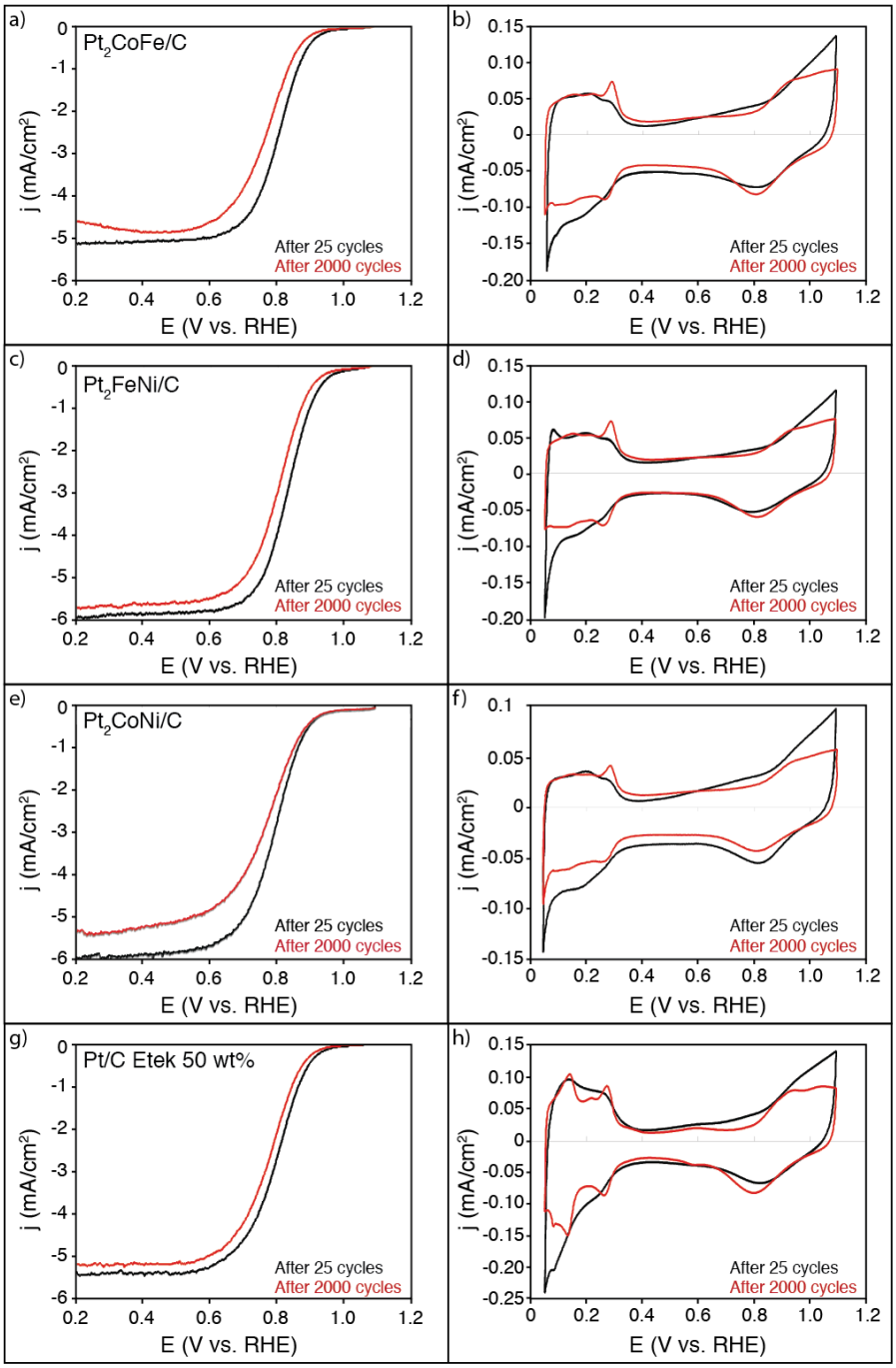

Figure 3.13 ORR polarization curve (left) and CV measurements (right) of Pt_2CoFe/C, Pt_2FeNi/C, and Pt_2CoNi/C. Electrochemical measurements were done in 0.1M H_2SO_4 at a scan rate of 20mV/s. ORR polarization analysis was taken after the electrolyte was purged with O_2 gas for at least 20 minutes. CV measurements were done in electrolyte purged with N_2 gas. Stability tests consisted of 2000 cycles from 0.05 – 1.10 V at 50 mV/s).

3.3.5 ORR Activity

Figure 3.13 shows the ORR polarization curves and CVs of Pt_2CoFe/C, Pt_2FeNi/C, Pt_2CoNi/C, and Pt/C 50 wt% ETEK standard after 25 and 2000 CV cycles. In the CVs of the pseudo-ternary materials after 2000 cycles, a peak at about 0.29 V appears; from hydrogen evolution studies on Pt single crystal surfaces, this peak correlates to the Pt (111) hydrogen desorption peak.[25] The shape of these CV scans after 2000 cycles indicate that the pseudo-ternary catalysts are growing and becoming more faceted, possibly becoming more octahedral in shape.

Figure 3.14 shows the ORR polarization curves of all the electrode materials and Pt/C standard at 25 and 2000 CV cycles on one plot. Table 3.3 summarizes the change in ECSA, mass activity, specific activity, and half-wave potential for ORR of each electrode material after 25 and 2000 CV cycles. Figure 3.15 shows the mass and specific activity of the ordered pseudo-ternary electrode materials after 25 and 2000 CVs vs. Pt/C 50 wt% Etek standard.

The trend in mass and specific activity (taken from ORR polarization curves at 0.9 V vs. RHE) after 25 CV cycles is $Pt_2FeNi/C > Pt_2CoNi/C > Pt/C > Pt_2CoFe/C$. After 2000 CV cycles, Pt_2CoNi/C showed the highest activity as seen in Figure 3.15. The high specific activity is most likely due to greater particle size after cycling as seen from Table 3.3 and the reduced ECSA from Table 3.4.

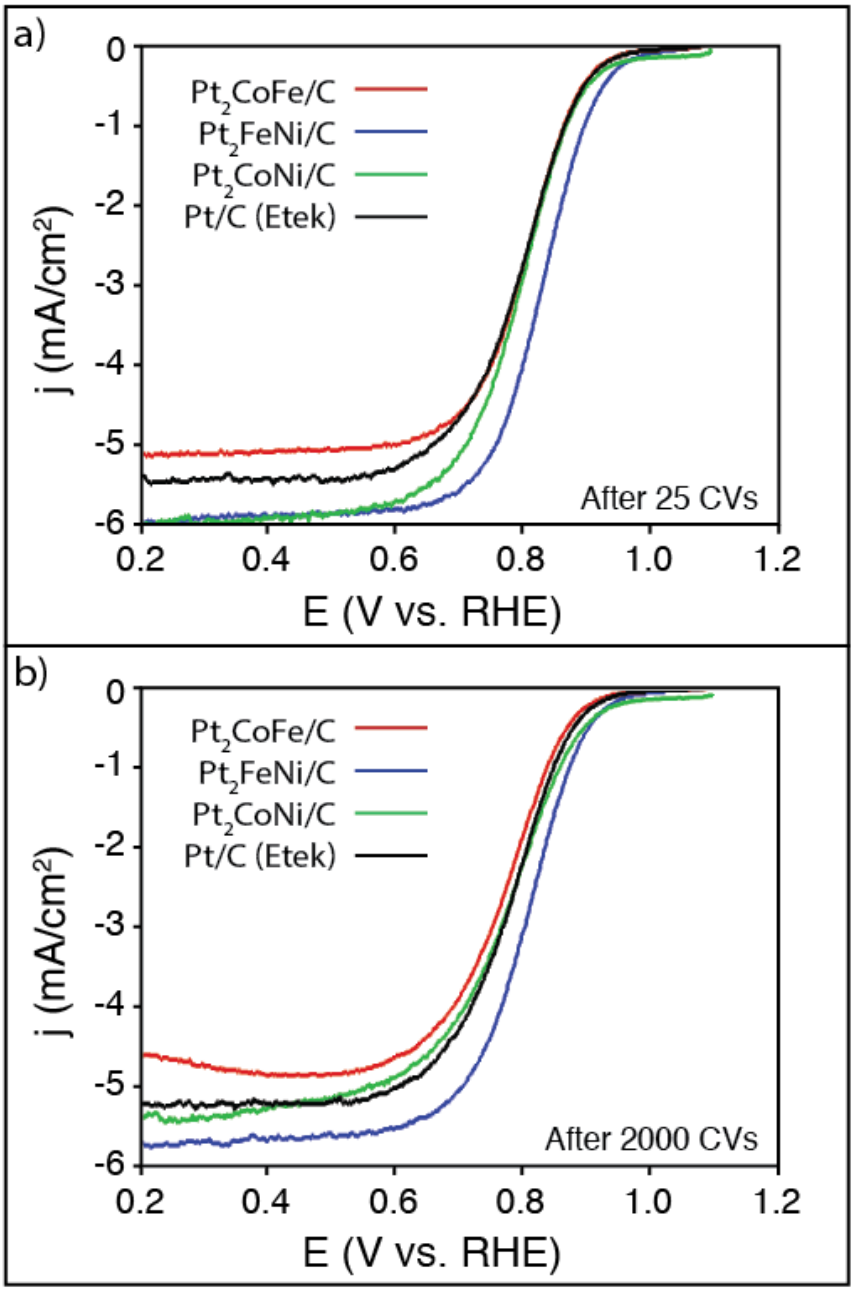

Figure 3.14 ORR cathodic polarization curves of Pt_2CoFe/C, Pt_2FeNi/C. Pt_2CoNi/C, and Pt/C (Etek) 50 wt% after 25 CVs (a) and after 2000 CVs (b). ORR polarization curves were done in O_2 saturated 0.1 M H_2SO_4 at a rate of 20 mV/s from 1.10 – 0.20 V. CVs were done from 0.05 – 1.10 V at 50 mV/s in N_2 saturated 0.1 M H_2SO_4.

Table 3.4 Summary of ORR activity of ordered Pt_2CoFe/C, Pt_2FeNi/C, Pt_2CoNi/C,

and Pt/C_{Etek} 50 wt% standard. Electrochemical measurements were done in 0.1M H_2SO_4. The CV measurements were done at a rate of 50mV/s from 0.05 to 1.10V.

Electrode Material	Pt Loading ($\mu g/cm^2$)	ECSA (m^2/g_{Pt})		Mass Activity @0.9V 20mV/s (mA/mg_{Pt})		Specific Activity @0.9V 20mV/s ($\mu A/cm^2_{Pt}$)		Half-Wave Potential $E_{1/2}$ (mV)	
		25 CV	2000 CV	25 CV	2000 CV	25 CV	2000 CV	25 CV	2000 CV
Pt_2CoFe/C	14.5	27.2	22.5	28.4	14.2	101	61	806	775
Pt_2FeNi/C	14.5	29.6	23.1	60.0	32.6	203	141	829	803
Pt_2CoNi/C	14.5	19.7	15.2	33.5	29.2	170	192	794	779
Pt/C 50% (ETEK)	14.5	40.5	32.3	29.2	17.2	72	53	796	781

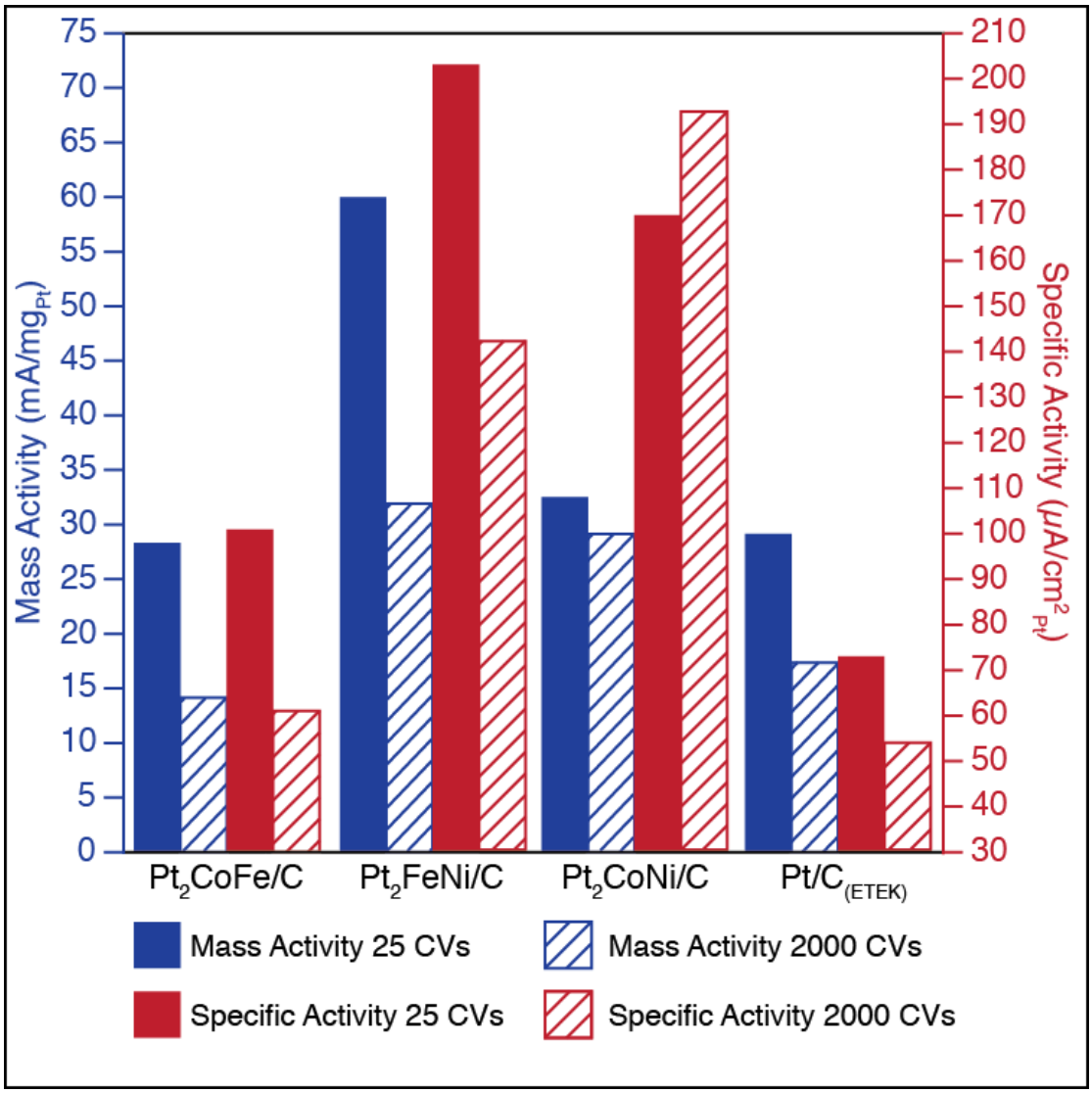

Figure 3.15 ORR activity summary of the ordered pseudo-ternary electrode materials after 25 CVs (solid) and 2000 CVs (dashed) vs. Pt/C 50 wt% Etek standard. For each electrode material, the blue bars indicate the mass activity and the red bars indicate the specific activity. The activity was taken from ORR polarization curves at 0.9V at a sweep rate of 20 mV/s during the cathodic sweep. The CVs were done from 0.05 – 1.10 V at a sweep rate of 50 mV/s. All measurements were done in 0.1 M H_2SO_4.

The mass and specific activity are not necessarily the best indicators of ORR

activity (as they depend on particle size, active surface area, mass loading on the electrode itself), so instead, the half-wave potential should receive the greatest attention. Looking at the shift in $E_{1/2}$, the trend in enhanced ORR activity is as follows: $Pt_2FeNi/C > Pt_2CoFe/C > Pt_2CoNi/C > Pt/C$, with Pt_2FeNi/C showing a $E_{1/2}$ roughly 33 mV more positive than Pt/C.

The activity, among the ternary electrode materials, seems to increase with greater Pt-Pt bond lengths (according to the Rietveld refinement data in Table 3.1). This trend would suggest that perhaps the activity enhancement vs. Pt-Pt bond distance is a "volcano-type" plot, with the peak centered near 2.707 Å. A plot of $E_{1/2}$ vs. Pt-Pt bond distance is depicted in Figure 3.16. The lattice parameters of Pt_2CoFe/C, Pt_2FeNi/C, and Pt_2CoNi/C match the lattice parameters of their bulk counterparts.[21,22,24] The dashed lines in Figure 3.13 outlines the "volcano" shape, suggesting that shortening the Pt-Pt bond beyond 2.736 Å (the half way point of the volcano shape) would yield lower ORR catalytic activity. Initial decrease of the Pt-Pt bond distance promotes higher ORR activity by strengthening the Pt-O bond, thus weakening the O-O bond.[26] However, if the Pt-O bond is too strong, the activity will begin to decrease since the reaction is now limited by the removal of Pt-OH from the Pt surface. Our data suggests that perhaps the optimum Pt-Pt bond distance is above 2.707 Å.

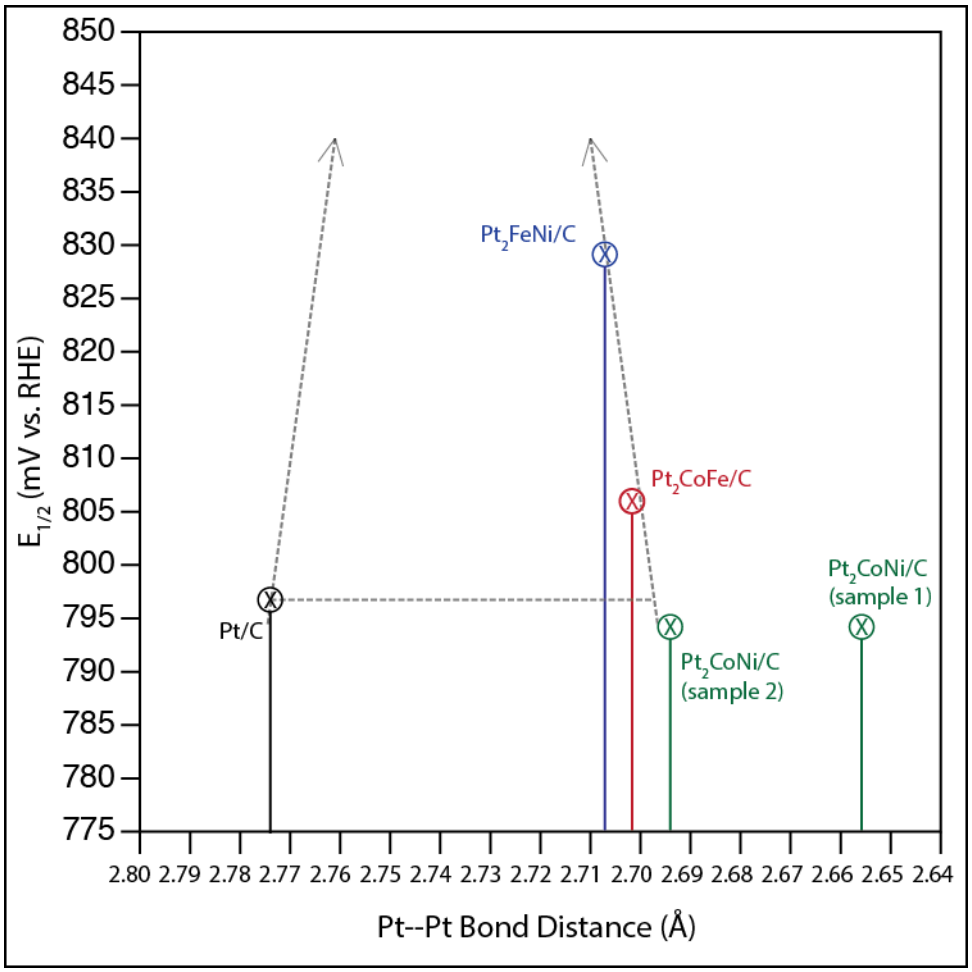

Figure 3.16 Plot of $E_{1/2}$ (mV vs. RHE) vs. decreasing Pt-Pt bond distance of the electrode material. The "X" indicates the cathodic half-wave potential of each electrode material (in 0.1 M H2SO4 at a sweep rate of 20 mV/s) taken after 25 CV sweeps. The lattice parameter was determined from Rietveld refinements from XRD patterns of the electrode material. The lattice parameter of Pt was taken from the bulk crystal structure. The grey dashed lines outline the "volcano" shape that extends beyond the range of the plot, indicating a Pt-Pt bond distance of ~ 2.736 may show the highest $E_{1/2}$ of roughly 1 V.

3.3.6 ORR Stability

As mentioned in section 3.3.2, the ordered pseudo-ternary materials are relatively more stable than their alloy counterparts with regards to non-Pt metal leaching. The change in ECSA after stability testing (2000 CV cycles from 0.05 – 1.10 V at 50 mV/s), suggests a reduction in active surface area, which is comparable to that of the Pt/C Etek standard. Looking at ECSA is not the best way to determine catalyst stability as the change in surface area may be due to increase in particle size and/or decomposition of the carbon support material (facilitating particle agglomeration). The change in the half-wave potential of the ordered pseudo-ternary electrode materials before and after stability tests were comparable to that of Pt/C. Pt_2CoNi/C showed decrease of roughly 15 mV (same as Pt/C), whereas the other two electrode materials showed a decrease of roughly 30 mVs. After 2000 CV scans, only Pt_2FeNi had a $E_{1/2}$ that was greater than Pt/C (803 vs. 781 mV), whereas the other two materials ended up behaving exactly like Pt/C. This suggests that the depth of leaching is least in Pt_2FeNi, so that the surface properties are still influenced by the ordered intermetallic material below the surface.

3.4 Conclusion

Ordered tetragonal Pt_2CoFe, Pt_2FeNi, and Pt_2CoNi in the 4-6 nm size range were synthesized using a modified solution-phase coreduction method, which utilizes the KCl byproduct to kinetically stabilize the NPs from agglomeration upon annealing at moderately high temperatures (550^oC). The ordered nanoparticles were transferred onto a carbon support using ethylene glycol and various sonication techniques. The

electrode materials were characterized using XRD, EDS, TGA, and TEM to determine the crystal structure, atomic composition, wt% on carbon-black, and particle size. The ORR activity and stability of these nanomaterials were tested in 0.1 M H_2SO_4 using CV and RDE electrochemical techniques. Pt_2FeCo and Pt_2FeNi, but not Pt_2CoNi, showed enhanced mass and specific activity for ORR compared to the Pt/C 50 wt% Etek standard, with Pt_2FeNi/C showing the greatest activity enhancement. The activity of the electrode materials decreased with decreasing Pt-Pt bond distances, suggesting the bond distances are too short and activity is hindered due to sluggish kinetics of oxygen removal from surface Pt atoms. Future work should focus on forming ordered Pt-M catalysts with Pt-Pt bond distances closer to 2.736 Å, or at least in the positive direction of 2.707 Å. EDS after electrochemical measurements showed that all of the ordered materials lost roughly 10% of the 3d metals through leaching, which is significantly (15 - 20 atomic %) less than Pt-M alloy materials of similar initial Pt-M atomic ratios. Thus, ordered Pt-based nanomaterials are both highly active and more stable ORR catalyst materials in PEMFCs.

REFERENCES

1 Cava, R. J.; Takagi, H.; Zandbergen, H. W.; Krajewski, J. J.; Peck, W. F.; Siegrist, T.; Batlogg, B.; Vandover, R. B.; Felder, R. J.; Mizuhashi, K.; Lee, J. O.; Eisaki, H.; Uchida, S. *Nature* 1994, *367*, 252.

2 Koh, S.; Toney, M. F.; Strasser, P. *Electrochimica Acta* 2007, *52*, 2765.

3 Jiang, J.; Kucernak, A. *Journal of Electroanalytical Chemistry* 2009, *630*, 10.

4 Hwang, S. J.; Yoo, S. J.; Jang, S.; Lim, T. H.; Hong, S. A.; Kim, S.-K. *The Journal of Physical Chemistry C* 2011, *115*, 2483.

5 Luo, J.; Wang, L.; Mott, D.; Njoki, P. N.; Kariuki, N.; Zhong, C.-J.; He, T. *Journal of Materials Chemistry* 2006, *16*, 1665.

6 Kang, Y.; Pyo, J. B.; Ye, X.; Gordon, T. R.; Murray, C. B. *ACS nano* 2012, *6*, 5642.

7 Thungprasert, S.; Sarakonsri, T.; Klysubun, W.; Vilaithong, T. *Journal of Alloys and Compounds* 2011, *509*, 6812.

8 J. Rodriguez-Carvajal, G. Rousse, C. Masquelier and M. Hervieu, *Physical review letters*, 1998, *81*, 4660-4663.

9 E. J. Verwey, J. T. G. Overbeek, *Theory of the Stability of Lyophobic Colloids*, Elsevier, Amsterdam 1948.

10 Markovic, N.; Gasteiger, H.; Ross, P. N. J. Electrochem. Soc. 1997, 144, 1591–1597.

11 Paulus, U. A.; Schmidt, T. J.; Gasteiger, H. A.; Behm, R. J. J. Electroanal. Chem. 2001, 495, 134–145.

12 Garsany, Y.; Baturina, O. A.; Swider-Lyons, K. E.; Kocha, S. S. *Analytical Chemistry* 2010, *82*, 6321.

13 Takahashi, I.; Kocha, S. S. J. Power Sources 2010, 95, 6312–6322.

14 Gasteiger, H. A.; Kocha, S. S.; Sompalli, B.; Wagner, F. T. Appl. Catal., B 2005, 56, 9–35.

15 Schmidt, T. J.; Gasteiger, H. A. In Handbook of Fuel Cells - Fundamentals, Technology and Applications; Vielstich, W., Gasteiger, H. A., Lamm, A., Eds.; Wiley, 2003; Vol. 2, p 316.

16 Biegler, T.; Rand, D. A. J.; Woods, R. J. Electroanal. Chem. 1971, 29, 269–277.

17 Ralph, T. R.; Hards, G. A.; Keating, J. E.; Campbell, S. A.; Wilkinson, D. P.; Davis, M.; St.-Pierre, J.; Johnson, M. C. J. Electrochem. Soc. 1997, 144, 3845–3857.

18 Chen, H.; Wang, D.; Yu, Y.; Newton, K. A.; Muller, D. A.; Abruna, H.; DiSalvo, F. J. *Journal of the American Chemical Society* 2012, *134*, 18453.

19 Winter, M.; WebElements: http://www.webelements.com, 1993-2012.

20 Rietveld, H. M. *Journal of Applied Crystallography* 1969, *2*, 65.

21 Woolley, J. C.; Bates, B. *Journal of the less-common metals* **1960**, *2*, 11.

22 Woolley, J. C.; Bates, B. *Journal of the less-common metals* **1959**, *1*, 382.

23 Cui, C.; Gan, L.; Heggen, M.; Rudi, S.; Strasser, P. *Nature materials* 2013.

24 Kanazawa, H.; Lauhoff, G.; Suzuki, T. *Journal of applied physics* **2000**, *87*, 6143.

25 Gomez, R.; Fernandez-Vega, A.; Feliu, J. M.; Aldaz, A. *Journal of Physical Chemistry* **1993**, *97*, 4769.

26 Takako, T.; Igarashi, H.; Uchida, H.; Watanabe, M. *Journal of the Electrochemical Society* **1999**, *146*, 3750.

27 Yuasa S., Miyajima H., Otani Y. *J. Phys. Soc. Jpn.* **63**, 3129 (1994).

28 Stevens, G.T., Hatherly, M., Bowles, J.S. *J. Mater. Sci.* **13**, 499 (1978).

29 Hinz, F., Inden, G., Pierron-Bohnes, V., Cadeville, M.C., Leroux, C. *J. Phys. F* **18**, 2033 (1988).

30 U.Esch & A.Schneider *Z. Elektrochem. Angew. Phys. Chem.* **50**, 268 (1944).

CHAPTER 4

ATTEMPT AT SYNTHESIZING TRUE-TERNARY NANOMATERIALS USING THE SOLUTION PHASE CO-REDUCTION METHOD

4.1 Introduction

True ternary intermetallic compounds possess a wide variety of physical properties, including super hard materials,[1] magnetoresistance,[2,5,6] superconductivity,[3] and ferromagnetic shape memory[4] to name a few. The diverse properties that ternary materials possess make them important for many scientific studies and technological applications. Traditionally, intermetallics are synthesized using high-temperature arc melting or by powder metallurgy techniques, which require high temperatures to homogenize the constituent elements followed by lengthy annealing times at reduced temperatures to form the ordered, more thermodynamically stable, crystal structure. The rate of these reactions is typically limited by solid-solid diffusion, which, due to the low diffusion rates, makes the high temperatures necessary.

Similar to the definition of an ordered binary material, the term "true ternary" material refers to a material consisting of three separate elements each occupying different crystallographic sites (Wyckoff position) in the unit cell. This is different than the pseudo-ternary materials discussed in chapter 3 (Pt_2CoFe, Pt_2FeNi, and Pt_2CoNi) where the three different elements share two different Wyckoff position in the binary prototype AuCu tetragonal unit cell. An example of a true ternary material is $AuCuSn_2$ with the unit cell depicted in Figure 4.1.[7]

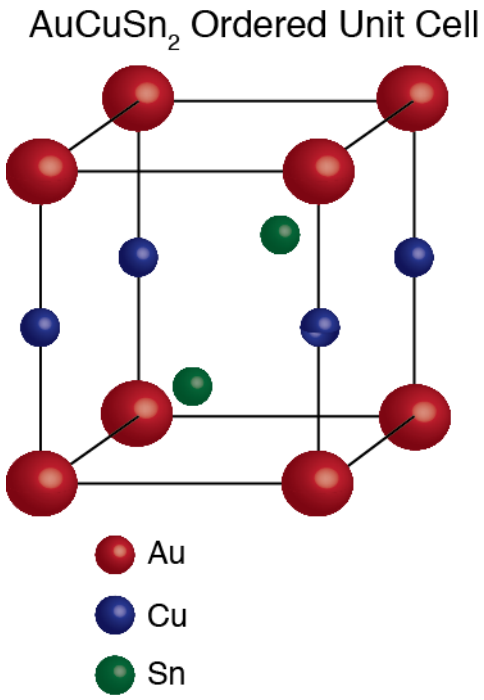

Figure 4.1 Unit cell of $AuCuSn_2$ (Au = red, Cu = blue, Sn = green).

To synthesize true ternary materials, it helps to understand the conditions at which thermodynamically distinct phases can occur at equilibrium. To visualize this, a ternary phase diagram is used. This type of diagram is three-dimensional but is illustrated in two-dimensions for ease of drawing and reading. Instead of being a rectangular plot, as it is for a binary phase diagram, it is a triangle with an element at each of the vertexes and the temperature/pressure stated. The phase diagram of $AuCuSn_2$[7] is depicted in Figure 4.2. Reading the composition of Au, Cu, and Sn at any point of the phase diagram in Figure 4.2 can be done by drawing three tie-lines, each parallel to a side of the triangle and going through the point in question. To find the Au composition, the line drawn parallel to the axis opposite of the Au vertex is the one needed, and the percent Au is then read off the axis. And example of the three lines are also shown in Figure 4.2 with the red dashed lines indicating the atomic percent of each element needed to form the $AuCuSn_2$ phase.

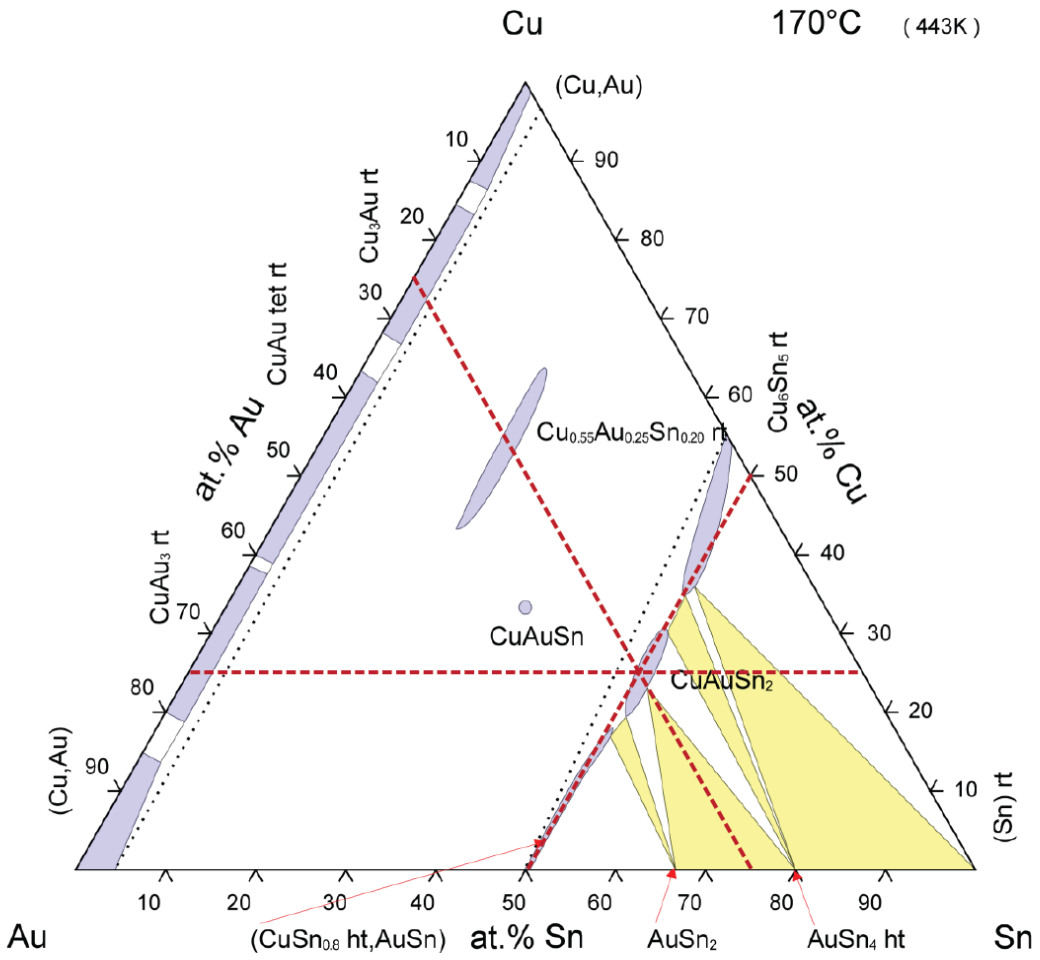

Figure 4.2 Ternary phase diagram of Au-Cu-Sn (yellow = three-phase fields, white = two-phase fields, blue = single phase fields) at 170^{o}C. The red dashed lines indicate the atomic percent of each element to form $AuCuSn_2$.

This chapter explores the application of the solution-phase coreduction method discussed in chapter two, in attempts to form ordered true-ternary nanomaterials. The phases explored in this chapter are $MnPd_2Sn$, $Bi_4Mn_5Pd_2$, $Bi_4Cu_4Mn_3$, and $AuCuSn_2$. The synthesis of bulk $MnPd_2Sn$,[4] $Bi_4Mn_5Pd_2$,[5] $Bi_4Cu_4Mn_3$,[6] and $AuCuSn_2$[7] have been reported, however, they often require high annealing temperatures (1100 – 1300 K) over long periods of time (1 – 2 weeks). The synthetic method described in chapter 2 was able to form ordered binary and pseudo-ternary materials at lower temperatures and shorter annealing times since the different elements are homogeneously mixed on the atomic scale. Also with the higher surface to volume ratio of atoms in nanoparticles, the average diffusion rates are much higher compared to bulk materials of similar composition. This chapter discusses the outcome of applying the synthetic method from chapter 2 towards the synthesis of ordered intermetallic true ternary nanomaterials.

4.2 Experimental

4.2.1 Synthesis of $MnPd_2Sn$/KCl Nanoparticles with KEt_3BH:

A similar method to that reported in Chapter 2 was used. Briefly, 55 mg of $PdCl_2$ (0.3 mmol), 32 mg of Li_2MnCl_4 (0.15 mmol), 29 mg $SnCl_2$ (0.15 mmol), and 32 mg LiCl (0.75 mmol) were added to 100mL three necked round bottom flask and dissolved in 25mL of dry THF. The solution is then rapidly reduced, via syringe, with 2.75 mL 1.0 M KEt_3BH to reduce all the metals and scavenge all the chloride ions to make KCl, leaving a 15% excess reducing agent to be sure that any reducible impurities in the THF (such as trace amounts of water) are also accounted for. The

black solution is then transferred to a 50 mL centrifuge tube, capped with a septum and fastened with copper wire. The solution is spun at 7000 rpm for 5 minutes and the clear supernatant is removed under a positive pressure of argon through a cannula needle. The black precipitate is then washed three times with 30mL aliquots of dry THF with a final wash with 30 mL of dry hexanes using the above procedure. The black precipitate is then dried under vacuum on the Schlenk-line. The dried black powder (nanoparticles encased in KCl, NP/KCl) is exposed to air slowly by backfilling the centrifuge tube with Ar, puncturing the septum with a needle and allowing the sample to sit overnight. This process appears to minimize oxidation of the particle surface upon air exposure.

4.2.2 Synthesis of $MnPd_2Sn$/KCl Nanoparticles with KNaph:

Same conditions as above, using KNaph/THF soln. (331 mg Naphthalene, 100 mg K metal, 15 mL dry THF) as the reducing agent. The dissolved metal precursor/THF soln. was added to the KNaph/THF solution.

4.2.3 Synthesis of $Bi_4Mn_5Pd_2$/KCl Nanoparticles with KEt_3BH:

Similar to the synthesis of $MnPd_2Sn$/KCl w/ KEt_3BH, 27 mg of $PdCl_2$ (0.15 mmol), 40 mg of Li_2MnCl_4 (0.375 mmol), 95 mg $BiCl_3$ (0.3 mmol), and 50 mg LiCl (1.2 mmol) were reduced with 3.25 mL of 1.0 M KEt_3BH/THF as a reducing agent.

4.2.4 Synthesis of $Bi_4Mn_5Pd_2$/KCl Nanoparticles with KNaph:

Similar to the synthesis of $MnPd_2Sn$/KCl w/ KNaph, 27 mg of $PdCl_2$ (0.15 mmol), 40 mg of Li_2MnCl_4 (0.375 mmol), 95 mg $BiCl_3$ (0.3 mmol), and 50 mg LiCl (1.2 mmol) using KNaph/THF soln. (400 mg Naphthalene, 127 mg K metal, 20 mL dry THF) as a reducing agent.

4.2.5 Synthesis of $Bi_4Cu_4Mn_3$/KCl Nanoparticles with KEt_3BH:

Similar to the synthesis of $MnPd_2Sn$/KCl w/ KEt_3BH, 3 mL of 0.1 M Li_2CuCl_4/THF soln. (0.3 mmol), 24 mg of Li_2MnCl_4 (0.225 mmol), 95 mg $BiCl_3$ (0.3 mmol), and 38 mg LiCl (0.9 mmol) using 4.5 mL of 1.0 M KEt_3BH/THF as a reducing agent.

4.2.6 Synthesis of $Bi_4Cu_4Mn_3$/KCl Nanoparticles with KNaph:

Similar to the synthesis of $MnPd_2Sn$/KCl w/ KNaph, 3 mL of 0.1 M Li_2CuCl_4/THF soln. (0.3 mmol), 24 mg of Li_2MnCl_4 (0.225 mmol), 95 mg $BiCl_3$ (0.3 mmol), and 38 mg LiCl (0.9 mmol) using KNaph/THF soln. (575 mg Naphthalene, 180 mg K metal, 20 mL dry THF) as a reducing agent.

4.2.7 Synthesis of $AuCuSn_2$/KCl Nanoparticles with KEt_3BH:

Similar to the synthesis of $MnPd_2Sn$/KCl w/ KEt_3BH, 91 mg $AuCl_3$ (0.3 mmol), 3 mL of 0.1 M Li_2CuCl_4/THF soln., 113 mg $SnCl_2$ (0.6 mmol), and 26 mg LiCl (0.6 mmol) using 4.5 mL of 1.0 M KEt_3BH/THF soln. as a reducing agent. Since Au^{+3} is slowly reduced to $Au_{(s)}$ by Sn^{+2} (apparent from a slow color change and precipitation of a brown solid), the $SnCl_2$ and LiCl was dissolved separately in 5 mL THF and $AuCl_3$ and Li_2CuCl_4/THF were dissolved in 20 mL THF. The $SnCl_2$/LiCl/THF soln. was injected to a rapidly stirring $AuCl_3$/Li_2CuCl_4/THF solution right before injection of the reducing agent.

4.2.8 Annealing Conditions

The annealing conditions to form the ordered intermetallic phases of each of the ternary nanoparticles are summarized in Table 4.1. Table 4.1 also gives the reducing agent used and the identified phases after annealing that were identified by XRD.

Table 4.1 Summary of annealing conditions in attempts to form the ordered intermetallic nanoparticles.

Target Phase	**Reducing Agent Used**	**Annealing Temp. (^{o}C)**	**Annealing Time (hr)**	**Identified Phases (from XRD)**
$MnPd_2Sn$	KEt_3BH	600	24	$Pd_{13}Sn_9$ + MnO
$MnPd_2Sn$	KNaph	600	24	Pd_2Sn + MnO
$Bi_4Mn_5Pd_2$	KEt_3BH	500	24	$PdBi_2$ + MnO
$Bi_4Mn_5Pd_2$	KNaph	400	24	$PdBi_2$ + MnO + $Mn_{0.35}Pd_{0.65}$
$Bi_4Cu_4Mn_3$	KEt_3BH	300	12	Bi + Cu + MnO
$Bi_4Cu_4Mn_3$	KNaph	250	12	Bi + Cu + MnO + $Bi_4Cu_{0.38}Mn_{3.41}$
$AuCuSn_2$	KEt_3BH	300	12	$AuCu_3$ + Cu_3Sn + AuCu + $AuSn_2$ + $Cu_{0.86}Sn_{0.14}$

4.3 Characterization

4.3.1 X-Ray Diffraction

The crystalline structure of the NP catalysts was examined with a Rigaku Ultima VI powder X-ray diffractometer (PXRD) with Copper K-α radiation (λ = 1.5406 Å and $K_{\alpha 2}$, λ = 1.5444 Å).

4.4 Results/Discussion

4.4.1 $MnPd_2Sn$ NPs made from KEt_3BH/KNaph reduction

Figure 4.3 and 4.4 are the powder XRD patterns of $Mn^{+2}/2Pd^{+2}/Sn^{+2}$ ions reduced with KEt_3BH and KNaph respectively and annealed to 600^{o}C for 24 hrs. The synthesis of bulk $MnPd_2Sn$ involves arc melting the stoichiometric amount of the pure metals, then annealing at 850^{o}. The identified phases for the sample reduced with KEt_3BH are $Pd_{13}Sn_9$, MnO, and KCl (which is left in to eliminate the washing and drying step as possible source of metal oxidation). No $MnPd_2Sn$ phase was detected via XRD. There are a few unidentified peaks in the diffraction pattern, which may be another Pd rich Sn alloy phase. It is possible that different reduction kinetics come into play since Mn^{+2} is more difficult to reduce than Pd^{+2} and Sn^{+2} (see Table 2.3 in chapter 2). Although KEt_3BH is a relatively strong reducing agent, it is possible that the difference in reduction potentials leads to differences in reduction rates of the metal cations. One might expect faster kinetics for the reduction of Pd and Sn, since their reduction potentials are more than 1 volt positive than that of Mn. This could lead to the formation of Pd-Sn nanoparticles, or to either nanoparticles that are Pd/Sn rich and Mn particles forming later. Another possibility would be the formation of particles in

which the cores are Pd/Sn rich with Mn rich shells. Upon eventual exposure to air, Mn rich particles or Mn rich shells would oxidize, preventing the formation of $MnPd_2Sn$ ordered intermetallic phase.

Perhaps using a stronger reducing agent, such as KNaph, would reduce all the metal cations at a high rate, forming nanoparticles stoichiometric $MnPd_2Sn$ particles. To test this hypothesis, reduction with a stronger reducing agent (KNaph) was done. The identified phases in Figure 4.4 are Pd_2Sn, MnO, and KCl. Using a different reducing agent does effect which phase forms after annealing, however, the $MnPd_2Sn$ was still not detected (by XRD). Another hypothesis as to why the ternary phase does not form may be due to the oxophilic nature of Mn, any exposed Mn on the surface of the nanoparticle is expected to oxidize and that could affect the ability to form the ordered ternary phase within the particle. However, in chapter 2, both single phase PtMn and Pt_3Mn were prepared via the same synthetic procedure; both phases containing similar, and higher, concentrations of Mn in the target phase. Perhaps surface segregation of Mn atoms in $MnPd_2Sn$ is higher than that of Pt-Mn phases, favoring the formation of MnO on the particle surface upon annealing.

Another hypothesis is that this method of synthesizing ternary metal NP compositions is not capable of forming true ternary phases. As discussed in chapter 2, the as-made nanoparticle composition varies depending on the as synthesized particle size, with small particles yielding statistically higher stoichiometric variation compared to larger particles (1 nm binary particles expecting to have compositional variation of +/- 10%).[8] With three possible elements, the statistical variation is expected to be greater, which may make forming compositionally “sensitive” ternary

phases difficult if the as synthesized particle size is small (1-2 nms). In such cases, one might expect the Mn to fully oxidize on air exposure.

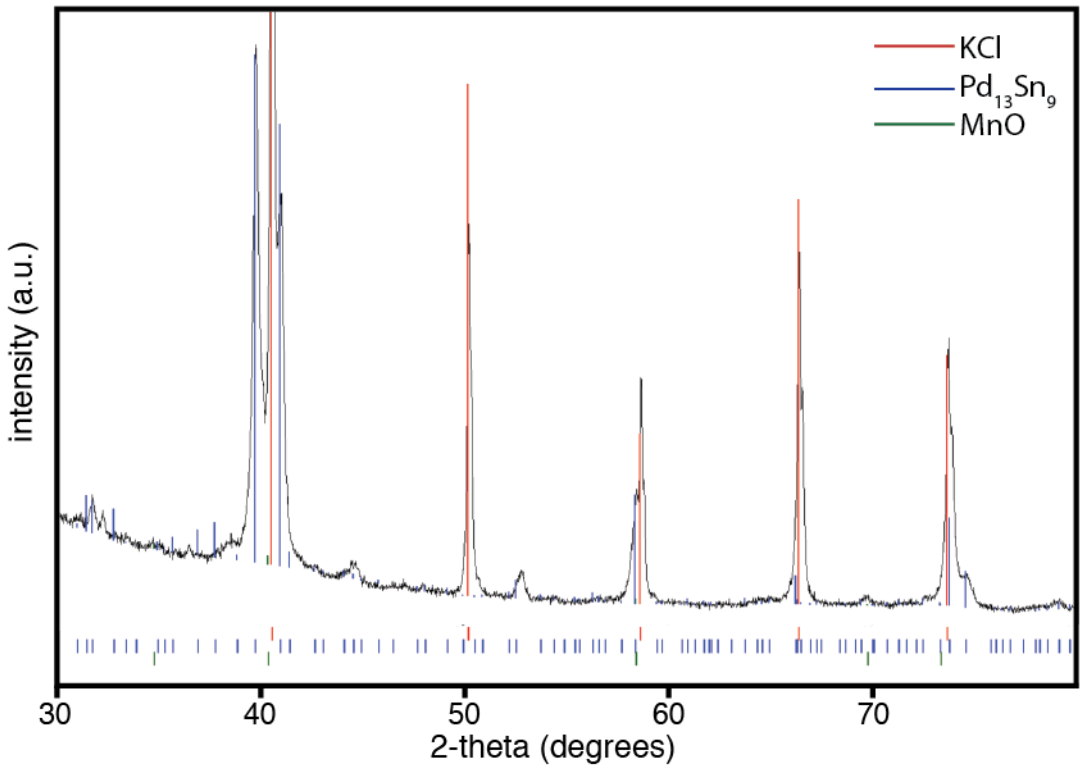

Figure 4.3 XRD pattern of $MnPd_2Sn$ reduced with KEt_3BH and annealed at 600°C for 24 hrs. The tick marks at the bottom represent the database peak locations for the identified phases (red = KCl #00-004-0587; blue = $Pd_{13}Sn_9$ #04-007-2411; green = MnO #01-071-4748). The colored lines overlaying the XRD pattern indicate the relative peak intensities of the corresponding phases.

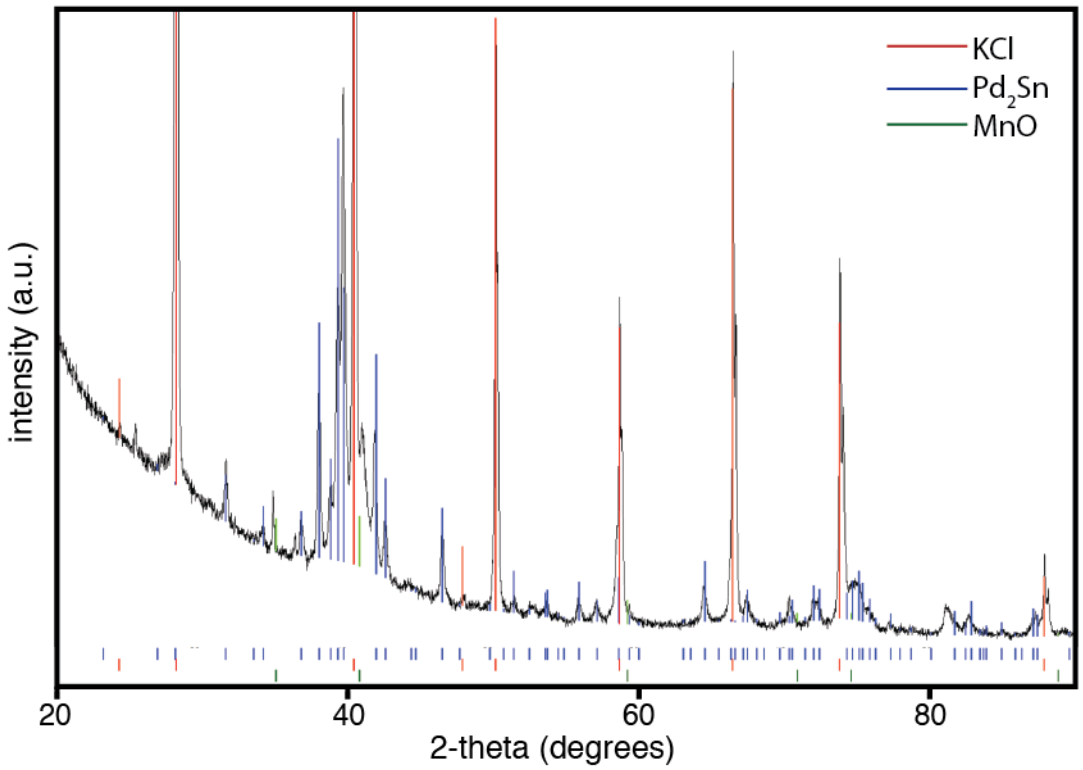

Figure 4.4 XRD pattern of $MnPd_2Sn$ reduced with KNaph and annealed at 600^{o}C for 24 hrs. The tick marks at the bottom represent the database peak locations for the identified phases (red = KCl #00-004-0587; blue = Pd_2Sn #00-052-1515; green = MnO #01-071-4748). The colored lines overlaying the XRD pattern indicate the relative peak intensities of the corresponding phases.

4.4.2 $Bi_4Mn_5Pd_2$ NPs made from KEt_3BH/KNaph reduction

Figure 4.5 and 4.6 are the powder XRD patterns of $4Bi^{+3}/5Mn^{+2}/2Pd^{+2}$ ions reduced with KEt_3BH and KNaph respectively and annealed at 500°C and 400°C respectively for 24 hrs. The synthesis of $Bi_4Mn_5Pd_2$ bulk material involves melting stoichiometric ratios of the pure metals at 1000-1100°C followed by a rapid quench to room temperature. The sample is then annealed at 400-550°C for at least 24 hrs.[2] The identified phases in Figure 4.5 are $PbBi_2$, MnO, and KCl (a byproduct of the reduction reaction and left in to exclude the washing/drying step as a possible source of Mn oxidation). No $Bi_4Mn_5Pd_2$ phase was detected via XRD. For similar reasons discussed in section 4.4.1, reduction with KNaph was done.

The identified phases in Figure 4.6 (sample reduced with KNaph) are $PdBi_2$, MnO, $Mn_{0.35}Pd_{0.65}$, and KCl. Reduction with a stronger reducing agent resulted in the formation of Mn-Pd alloy phase after annealing that was not apparent when KEt_3BH was used as a reducing agent. The formation of the Mn-Pd alloy indicates that using a stronger reducing agent does minimizes the problems caused by large differences in metal reduction potentials (phase segregation). The previous hypothesis that smaller as-synthesized nanoparticles, exhibiting larger statistical compositional variation, may be the reason why forming single true ternary phase sample is difficult using this method.

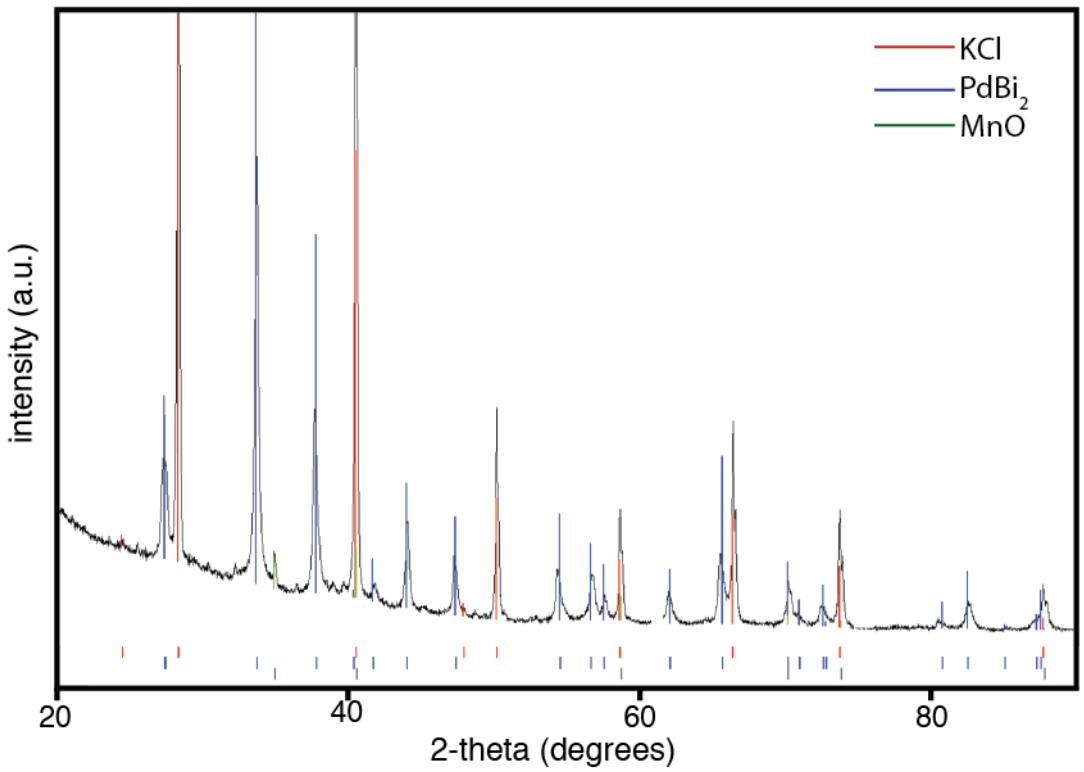

Figure 4.5 XRD pattern of $Bi_4Mn_5Pd_2$ reduced with KEt_3BH and annealed at 500°C for 24 hrs. The tick marks at the bottom represent the database peak locations for the identified phases (red = KCl #00-004-0587; blue = $PdBi_2$ #04-003-6165; green = MnO #01-071-4748). The colored lines overlaying the XRD pattern indicate the relative peak intensities of the corresponding phases.

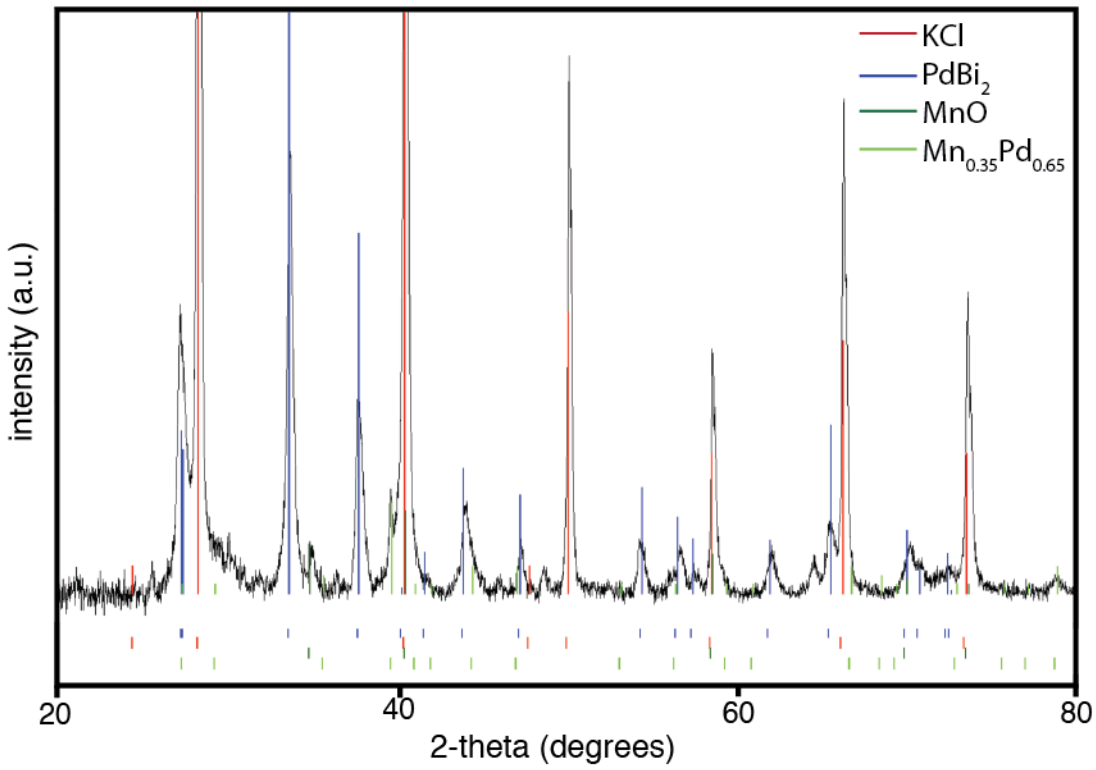

Figure 4.6 XRD pattern of $Bi_4Mn_5Pd_2$ reduced with KNaph and annealed at 400°C for 24 hrs. The tick marks at the bottom represent the database peak locations for the identified phases (red = KCl #00-004-0587; blue = $PdBi_2$ #04-003-6165; dark green = MnO #01-071-4748; light green = $Mn_{0.35}Pd_{0.65}$ #00-007-0122). The colored lines overlaying the XRD pattern indicate the relative peak intensities of the corresponding phases.

4.4.3 $Bi_4Cu_4Mn_3$ NPs made from KEt_3BH/KNaph reduction

Figure 4.7 and 4.8 are the powder XRD patterns of $4Bi^{+3}/4Cu^{+2}/3Mn^{+2}$ ions reduced with KEt_3BH and KNaph respectively and annealed at 300°C and 250°C respectively for 12 hrs. The synthesis of bulk $Bi_4Cu_4Mn_3$ involves melting stoichiometric ratios of the pure metals at 1000-1100°C followed by a rapid quench to room temperature. The sample is then annealed at 400-550°C for at least 24 hrs.[2] The identified phases in Figure 4.7 are Bi, Cu, MnO, and KCl (a byproduct of the reduction reaction and left in to exclude the washing/drying step as a possible source of Mn oxidation). No $Bi_4Cu_4Mn_3$ phase was detected via XRD. For similar reasons discussed in section 4.4.1, reduction with KNaph was done.

The phases identified in Figure 4.8 are Bi, Cu, $Bi_4Cu_{0.38}Mn_{3.41}$, and KCl. The dominant phases are Bi, Cu, and KCl, no $Bi_4Cu_4Mn_3$ phase was detected, although many of the unidentifiable peaks, with relatively small peak intensities, match the Bi-Cu-Mn alloy phase. For similar reasons discussed in section 4.4.1 and 4.4.2, this method may not be able to synthesize phase pure $Bi_4Cu_4Mn_3$ nanoparticles.

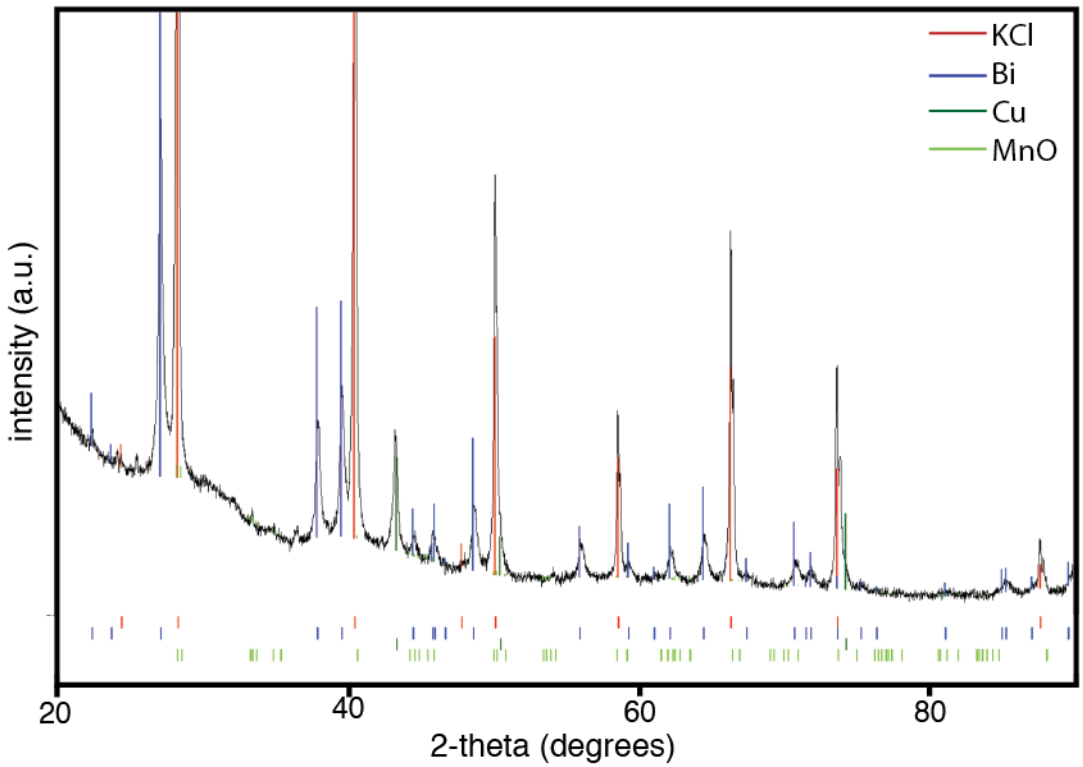

Figure 4.7 XRD pattern of $Bi_4Cu_4Mn_3$ reduced with KEt_3BH and annealed at 300°C for 12 hrs. The tick marks at the bottom represent the database peak locations for the identified phases (red = KCl #00-004-0587; blue = Bi #04-006-7762; dark green = Cu #01-070-3039; light green = MnO #04-002-2936). The colored lines overlaying the XRD pattern indicate the relative peak intensities of the corresponding phases.

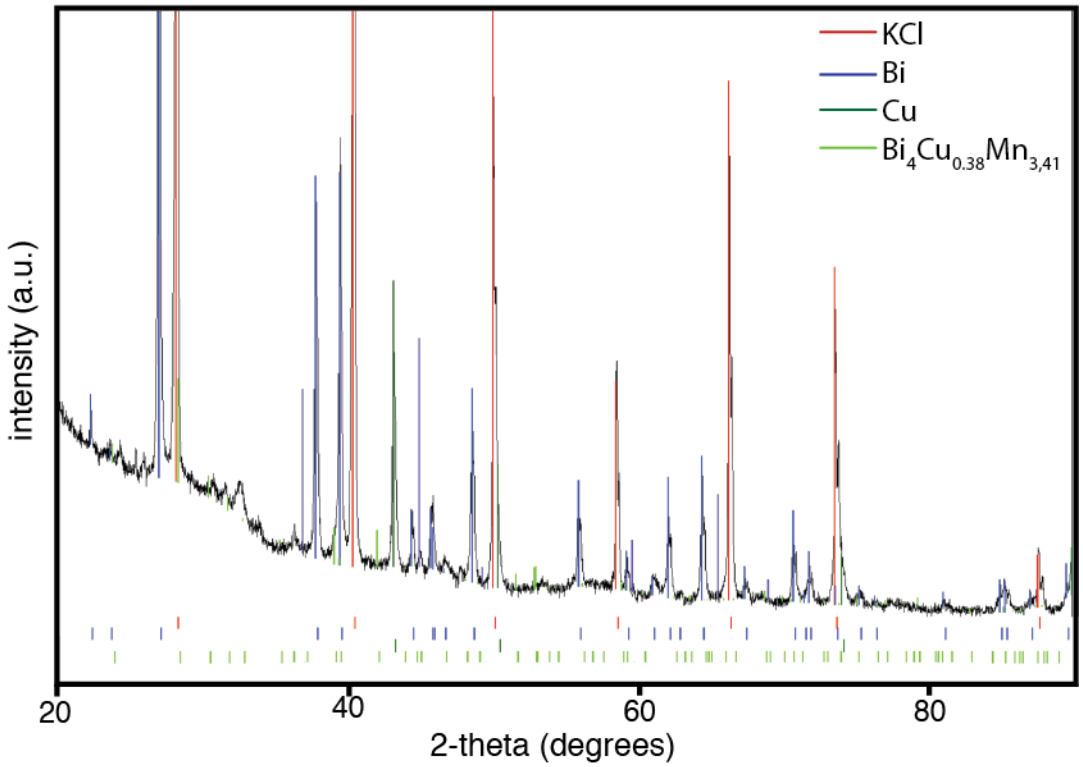

Figure 4.8 XRD pattern of $Bi_4Cu_4Mn_3$ reduced with KNaph and annealed at 250^{o}C for 12 hrs. The tick marks at the bottom represent the database peak locations for the identified phases (red = KCl #00-004-0587; blue = Bi #04-006-7762; dark green = Cu #01-070-3039; light green = $Bi_4Cu_{0.38}Mn_{3.41}$ #03-065-2578). The colored lines overlaying the XRD pattern indicate the relative peak intensities of the corresponding phases.

4.4.4 $AuCuSn_2$ made from KEt_3BH reduction

Figure 4.9 is the powder diffraction pattern of $Au^{+3}/Cu^{+2}/Sn^{+2}$ ions reduced with KEt_3BH and annealed at 300^{o}C for 12 hrs. The synthesis of bulk $AuCuSn_2$ involves melting stoichiometric amounts of the pure metals at 1025^{o}C for one minute, followed by a rapid quench to room temperature. The sample is then reground and annealed to 750^{o}C for 10 hours and cooled to room temperature at a rate of 1^{o}C/min. The identified phases in Figure 4.9 are $AuCu_3$, Cu_3Sn, AuCu, $AuSn_2$, $Cu_{0.86}Sn_{0.14}$, and KCl. The multitude of identified phases may have been due to possible interaction of Au^{+3} and Sn^{+2} cations (Sn^{+2} reducing Au^{+3}). However, carrying out the same reaction using 1.0 M $SnCl_4$/Heptane as the Sn precursor yielded a similar PXRD pattern. KEt_3BH is more than capable of rapidly reducing the different metal cations, thus, the inability to form phase pure $AuCuSn_2$ may be due to the limitations of this synthetic method described in the previous sections.

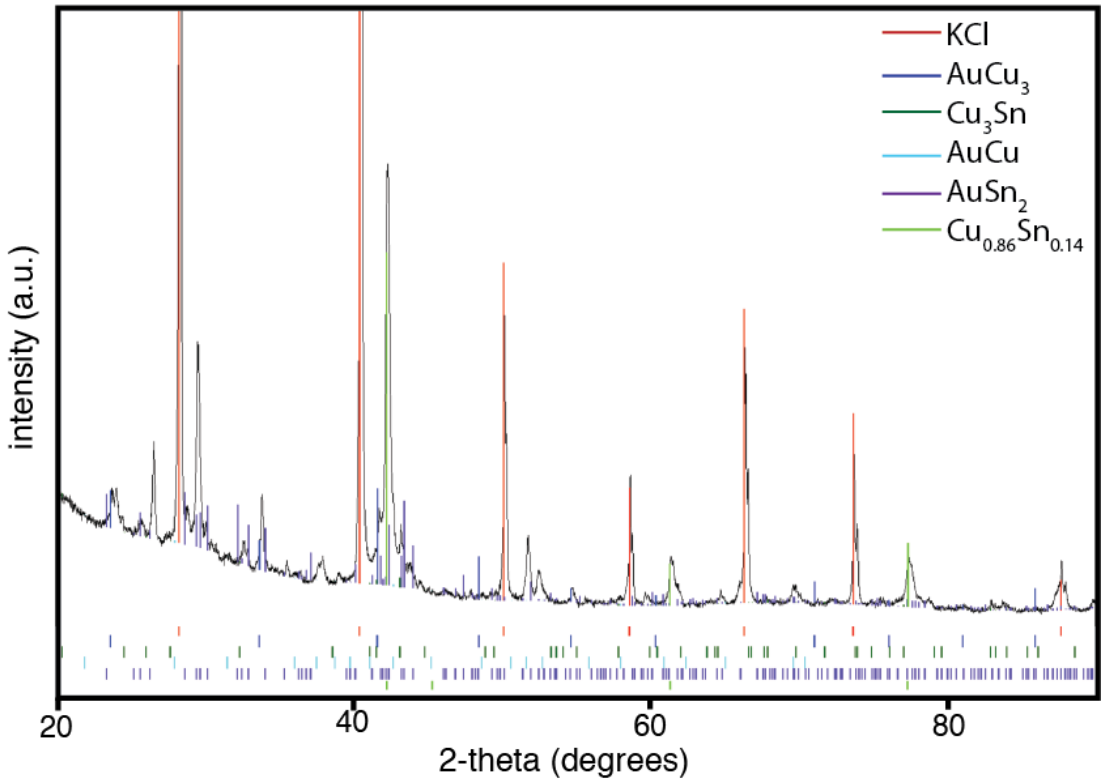

Figure 4.9 XRD pattern of $AuCuSn_2$ reduced with KEt_3BH and annealed at 300°C for 12 hrs. The tick marks at the bottom represent the database peak locations for the identified phases (red = KCl #00-004-0587; dark blue = $AuCu_3$ #03-065-3249; dark green = Cu_3Sn #01-074-6752; light blue = AuCu #00-038-0741; purple = $AuSn_2$ #04-007-1630; light green = $Cu_{0.86}Sn_{0.14}$ #04-007-3939). The colored lines overlaying the XRD pattern indicate the relative peak intensities of the corresponding phases.

4.5 Conclusion

The solution phase coreduction method, described in chapter 2 and capable of forming binary and pseudo ternary nanomaterials, was used to try and form ordered true ternary nanomaterials. $MnPd_2Sn$, $Bi_4Mn_5Pd_2$, $Bi_4Cu_4Mn_3$, and $AuCuSn_2$ were targeted to test the limitations of this method. The synthesis of compounds that contained manganese were done twice, once using KEt_3BH and then using KNaph, keeping all other reaction conditions the same. There was a difference in the XRD identifiable phases after heat treatment using the two reducing agents, which is likely due to the large difference in reducing power of KNaph and KEt_3BH. KNaph is the stronger reducing agent and should be able to reduce all the metal cations to the zero-valent state indiscriminately. No ternary phase diagram exist for the targeted ternary materials (except for Au-Cu-Sn), but from the lack of a single-phase samples, the targeted ternary phases may be too "compositionally sensitive" to form using this method. A hypothesis for this phenomenon aligns well with the theory that small as-synthesized nanoparticles exhibit greater compositional variation (especially for ternary metal systems), thus making it difficult to form true ternary phases that form within a small compositional window. Future work may change the temperature and concentration of the metal precursor solution prior to reduction to favor larger as-synthesized particles and higher statistical uniformity among the nanoparticle. This may yield enough nanoparticles with the appropriate atomic composition to form the targeted ternary phase upon annealing.

REFERENCES

1. Racault, C.; Langlais, F.; Naslain, R. *Journal of materials science* **1994**, *29*, 3384.
2. Street, B.; Suits, J. C.; Lee, K. *Solid State communications* **1974**, *14*, 33.
3. Meisner, G. P. *Physica B+ C* **1981**, *108*, 763.
4. Rocha, F. S. d.; Kakuno, E. M.; Kinast, E. J.; Mazzaro, I.; Fraga, G. L. F. *The European Physical Journal B* **2011**, *83*, 167.
5. Suits, J. C.; Street, G. B.; Lee, K. *Physical Review B* **1974**, *10*, 120.
6. Szytula, A.; Binczycka, H. *Solid State Communications* **1981**, *38*, 41.
7. Lange, S.; Nilges, T.; Hoffmann, R.-D.; Pottgen, R. *Z. Anorg. Allg. Chem.* **2006**, *633*, 1163.
8. D. DeSario in *Statistical analysis of compositional variation vs. particle size, Vol.* **2012**.

CHAPTER 5

CONCLUDING REMARKS

This dissertation has presented the development of a modified solution phase coreduction method for the synthesis of ordered intermetallic binary and pseudo-ternary compounds as nanoparticles/nanocrystals. Many of these materials have functional properties important for scientific study, with potential for possible incorporation into future energy devices.

The synthetic method, described in chapter two, was able to produce ordered binary nanomaterials with control over size and composition in a variety of metallic systems. The method uses metal chloride, and lithium metal chloride, precursors dissolved in THF, followed by rapid reduction with a potassium-based reducing agent (either KEt_3BH or KNaph depending on the reduction potential of the metal precursors). By using strong potassium reducing agents (enough to account for the number of chloride ions), alloy nanoparticles with near stoichiometric compositions are encased within a KCl matrix, which precipitate out of solution. After removal of the soluble byproducts, the NPs/KCl can undergo heat treatment to transform into the thermodynamically stable ordered phase without significant particle agglomeration and growth (the KCl acts as an encapsulating agent, significantly slowing interparticle mass transport). After formation of the desired phase, the KCl can be washed away with several water washes if particle agglomeration is not a concern. It is also possible to transfer the ordered nanoparticle onto a support material via sonication in ethylene

glycol (which is both a weakly coordinating surfactant that can be easily removed under mild heating conditions and a solvent for KCl). This method is important for catalytic applications (and other applications in which high surface areas and clean surfaces are important). This work demonstrates a new general approach to synthesizing intermetallic nanocrystalline solids, while previous synthetic methods were confined to a handful of metallic systems. Also, this method avoids the use of strongly coordinating ligands, which poisons the surface directly or with decomposition products that are formed on annealing.

In chapter 3, this method was used to form ordered tetragonal pseudo-ternary nanoparticles of the composition Pt_2MM' (M and M' from one each of Fe, Co, or Ni). The electrode materials were characterized using XRD, EDS, TEM, TGA, and their catalytic activity towards ORR was determined using RDE and CV techniques. Pt_2FeNi/C showed the highest activity towards ORR, with a half-wave potential 33 mV more positive than Pt/C standard. After a stability test of 2000 cycles (from 0.05 – 1.10 V at a sweep rate of 50 mV/s), Pt_2FeNi still showed the best activity with a half-wave potential 22 mV more positive then Pt/C (after the same stability test).

In chapter 4, the synthesis of ordered true-ternary nanomaterials was explored, uncovering some limitations of this synthetic method. Several ternary metal systems were evaluated, but were unable to synthesize single-phase true ternary nanomaterials. One hypothesis for this shortcoming may have been due to the large difference in reduction potentials of the metal precursors (the E^o for the reduction of Mn^{+2} and Pd^{+2} in aqueous systems are, for example, -1.18 V and +0.95 V respectively). To test this hypothesis, similar reaction conditions were employed to make nanoparticles using

either KEt_3BH or KNaph as reducing agents. The likelihood of forming nanoparticles near the desired stoichiometric ratios would be higher using a stronger reducing agent, with the hopes that the highly negative reduction potential of these reducing agents will reduce the metal cations rapidly upon contact. There was a difference in products obtained with the two reducing agents as inferred from the identified phases using XRD after annealing. However, no true-ternary phases were produced in observable amounts. Another hypothesis as to why forming ordered true-ternary nanomaterials is difficult (using this method) is possibly due to the large statistical variation in composition and or size from particle to particle, which increases upon decreased particle size and number of elements in the target composition. No ternary phase diagram exists for the ternary metal systems explored (except for Au-Cu-Sn), but judging from the many phases identified from XRD, the compositional window of these ternary phases may be too narrow compared to the spread in composition, among the synthesized particles, to produce single phase samples. Perhaps future work can focus on increasing the as-synthesized particle size (by changing reduction temperature and concentration) to minimize the compositional difference among the as-synthesized nanoparticles.

Nonetheless, the techniques in this dissertation can be used to access a wide variety of binary and pseudo-ternary ordered intermetallic phases as either alloy or ordered nanocrystals, and they have the potential to greatly expand the availability of complex multimetallic nanomaterials for future studies and integration future technological devices.